Short-Wave Infrared Photodetectors Based on Colloidal Quantum Dots

Kortegolfinfrarood-fotodetectoren gebaseerd op colloïdale nanokristallen

Chen Hu

Promotoren: prof. dr. ir. G. Roelkens, prof. dr. ir. Z. Hens
Proefschrift ingediend tot het behalen van de graad van
Doctor in de ingenieurswetenschappen: fotonica

Vakgroep Informatietechnologie
Voorzitter: prof. dr. ir. B. Dhoedt
Faculteit Ingenieurswetenschappen en Architectuur

Vakgroep Anorganische en Fysische Chemie
Voorzitter: prof. dr. I. Van Driessche
Faculteit Wetenschappen

UNIVERSITEIT
GENT

Academiejaar 2016 - 2017

ISBN 978-94-6355-014-7
NUR 965, 971
Wettelijk depot: D/2017/10.500/49

Universiteit Gent
Faculteit Ingenieurswetenschappen en Architectuur
Vakgroep Informatietechnologie

Promotor:

Prof. dr. ir. Günther Roelkens
Prof. dr. ir. Zeger Hens

Examencommissie:

Prof. dr. ir. Hendrik Van Landeghem (voorzitter)	Universiteit Gent
Prof. dr. ir. Günther Roelkens (Promotor)	Universiteit Gent
Prof. dr. ir. Zeger Hens (Promotor)	Universiteit Gent
Prof. dr. ir. Dries Van Thourhout (Secretary)	Universiteit Gent
Prof. dr. ir. Christophe Detavernier	Universiteit Gent
Prof. dr. ir. Arjan Jeroen Houtepen	Delft University of Technology
Prof. dr. ir. Wolfgang Heiss	Friedrich-Alexander-Universität Erlangen-Nürnberg

Universiteit Gent
Faculteit Ingenieurswetenschappen en Architectuur

Vakgroep Informatietechnologie
Technologiepark-Zwijnaarde 15, B-9052 Gent, België

Tel.: +32-9-264.33.41
Fax.: +32-9-331.35.93

Proefschrift tot het bekomen van de graad van
Doctor in de ingenieurswetenschappen: fotonica
Academiejaar 2016-2017

Dankwoord

When I started to write my thesis, I thought I could finish the "Dankwoord" first since this seems an easy part. However, when the thesis came to an end, this section was the last unfinished part and the most difficult part of them all. When writing this acknowledgement, various unforgettable moments during my PhD period flashed through my mind like movies… My PhD would not have been possible without the support from my promoters, my dear friends and colleagues and my family. I am extremely grateful to all for your help and encouragement…

First of all, I would like to express my gratitude to my promoter Günther. I am sincerely honored for having had the chance to work on this topic under your supervision in the Photonics Research Group. Thank you very much for all your support through the whole period of my PhD. When I faced difficulties or problems, you were always there when I needed you, your office door is always open for discussion and you always come with brilliant ideas. Someone said the experience of a PhD life is quite related to your supervisor, I fully agree with this. You gave me the freedom to do research during my entire PhD study, I had a lot of fun in the past few years and I really enjoyed it. Thank you.

Secondly, I would also like to thank my promoter Zeger, from the Physics and Chemistry of Nanostructures group at Ghent University. Thank you for giving me the opportunity to work in the PCN group, the experience to work in two completely different groups is very special. Your rich knowledge in nanomaterials and chemistry has enlightened me in many experimental problems, which was very valuable for my work. Thank you for all your great ideas and helpful discussions during my PhD, and also thank you for providing me the opportunity to collaborate with different groups and test new ideas in the first year of my PhD. This period was really a cornerstone of my PhD.

Thanks to all the professors in the Photonics Research Group. Thanks to Roel for making PRG so charming and attractive. Thanks to Dries for all the QD discussions. Thanks to Bart for the help during my measurements. Thanks to Wim for the great IPKISS, fantastic Photoshop skills and being a great actor for the movie of Hui. Thanks to Nicolas for the scientific discussions. Thanks to Geert and Peter for the nice chats.

I would also like to thank all the members of my PhD Jury: Prof. Wolfgang Heiss, Prof. Arjan Houtepen, Prof. Christophe Detavernier, and Prof. Dries Van Thourhout for the time spent on reading my thesis and for helping me to improve it.

I very much appreciate the opportunity to collaborate with different groups, I have got a lot of help and learned a lot from them. In order to obtain air-stable QD devices, I got a lot of help from Prof. Christophe Detavernier, Jakob Kuhs and Dr. Kilian Devloo-Casier for the nice ALD deposition in the CoCooN Group in S1, thank you very much. I would also like to thanks Prof. Wolfgang Heiss, Dr. Sergii Yakunin and Dr. Mykhailo Sytnyk in Johannes Kepler University Linz for the collaboration on photodetector characterization, Hall measurement and fancy HgTe quantum dots. Also, thanks to Prof. Daniel Vanmaekelbergh and Dr. Wiel Evers for teaching me to prepare the beautiful PbSe superlattices and nice TEM pictures. Thanks to Prof. Arjan Houtepen and Dr. Ryan Crisp from Delft University of Technology for their patience and help to implement TRMC measurements. Thanks to Prof. Filip Beunis and Dr. Oksana Drobchak for the luminescence microscopy measurements in the Liquid Crystals and Photonics Group.

Many thanks to Alban for all your kind help during the first year of my PhD. Thank you for your step-by-step teaching since the second day I started working in the Photonics Research Group. From device fabrication to characterization, you taught me a lot. I could not have done this without you, merci beaucoup.

I would also like to thank Yolanda for teaching me how to synthesize nice PbS QDs, and for all your help in the PCN group to help me when I started various chemical manipulations from the second month of my PhD. I really enjoyed the time in the chemistry lab of PCN with you, it was a lot of fun. Muchas gracias!

For device fabrication, I spent a lot of time in the Ghent University cleanroom, and I also got a lot of help from the lovely people in the lab. Steven, thank you so much for all the help during my processing. No matter what happened, you always remained calm and patient, as a guardian angel in the cleanroom. Moreover, you make a beautiful balance between engineering and art, thank you for the fantastic painting, it is one of the best gifts I have ever got. Many thanks to Liesbet for all the safety training and nice SEM and FIB pictures, I really enjoyed the time spent with you for all the chatting, laughing and nice music sharing moments. Thanks to Kasia for a lot of help in the cleanroom, you made the cleanroom life more fun than I expected. Thanks to Muhammad for all the metal deposition processes. Thanks to John George from the Liquid Crystals and Photonics group for the ALD experiments.

My PhD could also never have been realized without the help of all the administrative staff members in the Photonics Research Group and PCN Group. Thanks to Ilse Van Royen for all the things no matter big or small during my

PhD. Thanks to sweet Kristien for being a great doctor for my computer. When I rushed into your office with a “sick” computer and you always made magic happen. Thanks to Mike from the beginning of my PhD for my contracts. Thanks to Ilse Meersman for all the PO numbers. Thanks to Michael for all the python cods in the lab, you made my measurement life much easier, and furthermore, thank you for the Dutch summary translation of my thesis, it is a lot of work and you did a fantastic job (I think), thanks. Thanks to Jeroen and Jelle for the great help and practice during my measurements. Thanks to Bert for his organization skills. Thanks to Peter and Bart for all the nice crafts in the workshop. Thanks to Pierre and Claudine for all the administrative issues in PCN. Thanks to Danny and Tom for all the help during FTIR measurements. Thanks to Els for the nice XPS measurements. Thanks to Pat for solving all the IT problems in PCN group.

Thanks to the QD photodetector team: Willem, Nayyera, Kasper and Jorick for the nice discussion and inspiration. Thanks to the QD team: Weiqiang, Yunpeng, Pieter, Bram, Abdoulghafar, Suzanne, Lukas, Renu, Edouard. I learned a lot from you. Thanks to the MIR team: Alban, Nannicha, Aditya, Bart, Ruijun, Muhammad, Utsav, François, Sanja, Anton, Dorian, for the expansion of my view during my research.

During my PhD, I got a lot of help from my colleagues in the Photonics Research Group. Many thanks to Weiqiang and Yunpeng for discussions on QDs and simulations, I learned a lot from you. Thanks to Eva, Hui and Jing for the help during my measurement and mask design. Thanks to Ruijun and Bin for the help on simulation. Thanks to Haolan for a lot of discussion and help on lock-in measurements. Thanks to Hongtao for all the measurements done in IMEC.

I would also like to thank my colleagues in the PCN group who helped a lot during my PhD. Thanks to Stijn and Willem for the nice TEM and SEM measurements. Also thanks to Sofie for TEM pictures. Thanks to Tangi and Marco for the nice CdSe/CdS QDs. Thanks for Jonathan for the nice HfO_2 QDs. Thanks to Kim for the ZnSe QDs and all the help in the lab. Thanks to Pieter for the help discussion on QDs. Thanks to all the friends and colleagues in S3, Antti, Ruben, Antoine, Elena, Jorick, Suzanne, Renu, Kishu, Katerien, Emile, Valeriia, Shalini, Mickael, Arnau, Dorian, Igor… Thank you all for the feeling you gave me when I started my PhD.

Many thanks to the senior PhDs in my early PhD period in the Photonics Research Group, particularly, sweet and glamorous Pauline, cheerful Cristina, considerate Eva, beautiful Marie, Elewout, Sam, Kristof, Wout, Karel, Stevan, Bram, Yannick, Thomas, Tom, Thijs, Peter De Heyn, Diedrik. Thank you all for the unforgettable chats, drinks and parties, I enjoyed all the moments spent with you.

Thanks to all my office mates and dear friends during the time in Technicum and iGent. Jan-Willem, Stefania, Jesper, Alfonso, Dorian, Sulakshna, Pieter Dumon, Antonio, Alex, Paul, Fabio, Grigorij, Nayyra for the enjoyable working, partying and great foosball time. Thank you for making my everyday life in Gent so colorful and joyful. Daan, thank you for your friendship, for all the memorable moments we spent together, and for being a great guide in Brugge.

I would also like to thank all the friends and colleagues in the Photonics group, Amin, Leili, Utsav, Ashwyn, Sarah, Andereas, Pieter Wuytens, Herbert, Sanja, Sören, Alejandro, Lukas, Artur, Rodica, Stephane, Sarvagya, Frederik, Koen, Ashim, Samir, Ananth, Kumar, Bendix, Mahmoud, Nina, Kasper, Anton,…, for all the nice chats and discussion, for the great time spent in the cleanroom together, for all the friendship and help from your guys.

Special thanks to all my Chinese friends and colleagues in Gent, Yunpeng, Weiqiang, Yufei, Haolan, Lei Guo, Bin Tian, Huihui, Ruijun, Ang, Jing, Jianping, Zhechao, Ying Zheng, Yanlu, Hui Yu, Xiaoning, Xiaomin, Yuxin, Ye, Lianyan, Xin, Keqi, Yingchen, Qiangsheng, Yuting, Min, Yingtao, Xu Liu, Jinghao, Haifeng, Linghua, Shih-Che, for sharing so many great moments together, for so many nice trips in Europe and for all the enjoyable time during my life in Gent.

I would like to thank all my dear friends I met in Sweden during my master study. Thanks to Xiaodan, Bin, Qijun, Yajun, Qiang Tai, Tao Liu, Meixian, Ye Tian, Wenqing, Said, Aimi, for your friendship and the great moments we shared together. Thanks to Sha Tao, Jia mao, Yeyu, for your nice company and all the joyful moments in Sweden. Thanks to my dear friend Yuan Tian and Deng Jing, for all your support, cheerful time and friendship over past 15 years.

My deepest and heartfelt gratitude goes to my parents who raised me, support and love me unconditionally. This thesis is especially dedicated to them. 最深的感谢给我的父母，谢谢你们一直以来对我无条件的支持和爱，我爱你们，直到永远。

Ghent, May 2017
Chen Hu

Table of Contents

List of Figures

List of Tables

List of Acronyms

A

AFM	Atomic Force Microscopy
ALD	Atomic Layer Deposition

C

C_2Cl_4	Tetrachloroethylene
CMOS	Complementary Metal-Oxide-Semiconductor

E

EBL	Electron-Beam Lithography
EDT	1,2-ethanedithiol
ETL	Electron Transport Layer

F

FTIR	Fourier-Transform Infrared Spectroscopy

G

G-R noise	Generation-Recombination noise

H

HTL	Hole Transport Layer

L

LB	Langmuir–Blodgett

LBL	Layer-by-layer
LEDs	Light Emitting Diodes

M

MBE	Molecular Beam Epitaxy
MeOH	Methanol
MIR	Mid-Infrared
MOVPE	Metalorganic Vapour Phase Epitaxy

N

NEP	Noise Equivalent Power
NIR	Near-Infrared

O

ODE	Octadecene
OlAc	Oleic Acid

P

PECVD	Plasma-Enhanced Chemical Vapor Deposition
PL	Photoluminescence

Q

QDs	Quantum Dots
QDSSCs	Quantum Dot-Sensitized Solar Cells
QY	Quantum Yield

R

RIE	Reactive-Ion Etching

S

SEM	Scanning Electron Microscope
SNR	Signal-to-Noise Ratio
SWIR	Short-Wave Infrared

T

TE	Transverse-Electric
TMA	Trimethylaluminum
TEM	Transmission Electron Microscopy
TM	Transverse-Magnetic

U

UV	Ultraviolet

X

XPS	X-ray Photoelectron Spectroscopy

Nederlandse samenvatting –Summary in Dutch–

In de afgelopen decennia is er een enorme ontwikkeling in fotonische geïntegreerde circuits voor optische interconnecties in het 1.3-1.55 μm golflengtebereik, als gevolg van de snelle groei van persoonlijke communicatie. De laatste jaren heeft de toepasbaarbaarheid van fotonische geïntegreerde circuits uitbreiding genomen door de groei van hoogvolume markten zoals gasdetectie en biomedische instrumenten. Infraroodspectroscopie is een belangrijke methode in een deel van deze nieuwe toepassingen. De meeste infrarood spectroscopische detectiesystemen bestaan uit dure afzonderlijke componenten zoals lasers en fotodetectoren. In dit proefschrift tonen we een nieuwe benadering voor infraroodfotodetectoren op basis van halfgeleider colloïdale nanokristallen (of 'quantum dots', QDs) in oplossing, die het mogelijk maken om een veelzijdige, lage kost fotodetectortechnologie compatibel met geïntegreerde circuits te realizeren.

De toegenomen belangstelling in colloïdale QDs voor geïntegreerde fotodetectortoepassingen kan worden toegeschreven aan drie factoren. Ten eerste is er de lage kost van materiaal en fabricage. Ten tweede kan het golflengtegebied gemakkelijk worden aangepast door het kiezen van het juiste QD materiaal en de bijbehorende QD grootte, tot in het mid-infrarood. Deze unieke eigenschap maakt colloïdale QDs tot een aantrekkelijk materiaal, met name in het golflengtegebied boven 0.9 um dat niet wordt waargenomen door kristallijn silicium, een courrant gebruikt fotodetectormateriaal. De derde reden is de flexibiliteit in heterogene integratie door het gebruik van QDs in oplossing, hetgeen potentieel biedt voor grootschalige integratie op CMOS uitleesschakelingen of fotonische geïntegreerde circuits.

Colloïdale quantum dot films

Om colloïdale quantum dot films te implementeren die geschikt zijn voor fotodetectortoepassingen, streven we naar de ontwikkeling van een efficiënte vaste stof ligand-uitwisseling om het transport van ladingdragers in quantum dot films te verbeteren waardoor opto-elektronische toepassingen mogelijk worden. Verschillende benaderingen voor de depositie van quantum dots in oplossing, zoals 'drop casting' en 'dip coating', werden verkend om homogene quantum dot films te verkrijgen. Diverse benaderingen voor vaste stof ligand-uitwisseling, ter verbetering van de fotoconductiviteit, worden besproken. Om scheuren in de film tijdens vaste stof ligand-uitwisseling te vermijden en scheurvrije QD films met voldoende dikte te verkrijgen, werd een laag-per-laag depositietechniek voor quantum dots ontwikkeld.

Het aanbrengen van micropatronen in lagen quantum dots met anorganische liganden met behulp van selectief nat etsen

De geschiktheid van colloïdale QDs voor verwerking in oplossing biedt vooruitzichten om componenten gebaseerd op QDs te combineren met geïntegreerde elektronische of fotonische schakelingen. Dit vereist technieken om goed gedefinieerde en uitgelijnde lagen van colloïdale QDs te produceren. In de literatuur zijn verschillende werkwijzen onderzocht om micropatronen te creëren, elk met hun eigen voordelen en nadelen. De depositie op een driedimensionaal oppervlak (zoals een elektronische of fotonische geïntegreerde schakeling) en de vorming van een meerlaagse filmen in micropatronen blijft evenwel een uitdaging. Bovendien kan geen van de bestaande methoden direct toegepast worden voor de patroonvorming van QD films met anorganische liganden die typisch worden gebruikt als absorptielaag in zonnecellen en fotodetectoren of als geleidend kanaal in veldeffecttransistoren.

In dit werk maken we gebruik van PbS colloïdale QDs om een nieuwe techniek voor patroonvorming van QD films gestabiliseerd door anorganische liganden aan te tonen. De PbS QD films worden geproduceerd met een laag-per-laag benadering. Elke cyclus omvat het aanbrengen van een QD laag door dip coaten, de vervanging van de oorspronkelijke organische liganden door metaalvrije anorganische liganden, zoals OH^- en S^{2-}, gevolgd door een grondige reiniging van de verkregen film. Dit resulteert in gladde en scheurvrije QD films. De micropatronen worden gedefinieerd door een positieve fotoresist, gevolgd door verwijdering van de onbedekte QDs door nat etsen met een HCl/H_3PO_4 mengsel. De resulterende patronen kunnen gedefinieerd worden met een resolutie tot 500 nm, begrensd door de resolutie van het lithografische proces en het wordt aangetoond dat het proces ook kan worden toegepast op 3D substraten. Om de invloed van deze patroonvormingstechniek op de eigenschappen van het

colloïdale QDs verder te evalueren, werden films van sterk luminescent CdSe/CdS deeltjes behandeld met dezelfde techniek. Analyse van de fotoluminescentie toont aan dat meer dan 78% van de quantumopbrengst behouden blijft na fotolithografie en nat etsen. Dit geeft aan dat de voorgestelde aanpak een effectieve microstructurering van QD films mogelijk maakt zonder dat de QD eigenschappen ongunstig beïnvloed worden.

Luchtstabiele korte-golf infrarood PbS colloïdale quantum dot fotogeleiders gepassiveerd met Al_2O_3 atoomlaag depositie

Kritiek voor fotodetector en fotovoltaïsche toepassingen is de vervanging van de lange isolerende organische liganden die de gesynthetiseerde QDs omgeven door kortere eenheden om de mobiliteit van de ladingdragers in QD films te verbeteren. Bovendien is het bekomen van luchtstabiele colloïdale QD componenten van essentieel belang voor praktische toepassingen. Voor het verkrijgen van luchtstabiele QD componenten is het voornaamste doel om oxidatie van de QD film te voorkomen. Dit vereist een goed passiverende, pinhole-vrije laag die transparant is voor de golflengtes die we willen detecteren. Atoomlaagdepositie (ALD) resulteert meestal in films zonder 'pinholes' en is daarom zeer geschikt voor passiveren. Al_2O_3, waarschijnlijk het best bestudeerde ALD materiaal, is hier een natuurlijke keuze aangezien het een brede bandkloof isolator is en transparant voor het korte-golf infrarood. Al_2O_3 lagen met een dikte van 30 nm werden gebruikt in dit werk aangezien dergelijke lagen pinhole-vrij worden beschouwd.

In deze studie maken we gebruik van ALD om Al_2O_3 films te deponeren op PbS colloïdale QD films voor passivatie en aldus luchtstabiele SWIR fotodetectoren te implementeren. Homogene en scheurvrije QD films worden verkregen door een laag-per-laag (LBL) benadering. Voor oppervlakte verlichte detectoren worden de QD films gevormd op geprefabriceerde, geschrankte elektroden, waarbij nat etsen wordt gebruikt om de geometrie van de QD film te bepalen. De resulterende fotodetectoren worden daarna gepassiveerd met een aluminiumoxide laag via ALD. Op deze manier verkrijgen we PbS colloïdale QD fotodetectoren die luchtstabiel zijn op lange termijn, met een cut-off golflengte van 2.4 micrometer. Voor PbS/S^{2-} fotodetectoren verkrijgen we een responsiviteit tot 50 A/W en een specifieke detectiviteit van 3.4×10^8 Jones bij 1550 nm en 300 K. Voor PbS/OH^- fotodetectoren is de responsiviteit ~8 A/W en de overeenkomstige specifieke detectiviteit ~2.3×10^8 Jones onder dezelfde meetomstandigheden. De 3dB bandbreedte van de PbS/S^{2-} en PbS/OH^- fotodetector is 40 Hz en 11 Hz respectievelijk verkregen bij 1.1W/cm^2

verlichting bij 2250 nm golflengte. Deze techniek kan een goede aanpak worden om lage kost beeldsensoren en individuele fotodetectoren te realiseren.

Luchtstabiele PbS colloïdale quantum dot fototransistoren

Om luchtstabiele colloïdale quantum dot-gebaseerde componenten te verwezenlijken, werd ALD passivatie gebruikt. Echter, de fotostroom is gelimiteerd na ALD passivatie, hetgeen resulteert in een afname van de prestaties van de component. Teneinde de afname van de fotostroom te voorkomen, stelden we het gebruik voor van een extra laag nanokristallijn materiaal met grote bandkloof, als intermediaire laag, om indringing van alumina in de PbS laag te voorkomen.

Dit werk onderzocht twee nanokristallijne materialen met grote bandkloof, ZnSe en HfO_2, als intermediaire laag om de prestaties van de component te verbeteren. Beide materialen toonden een verbeterde fotostroom, maar door de moeilijkheid van ALD-groei op ZnSe met organische liganden blijft de implementatie van luchtstabiele componenten nog steeds een uitdaging. Bovendien leidt een uitwisseling van liganden voor ZnSe nanokristallen, ter bevordering van de ALD, gewoonlijk tot inhomogene en discontinue films, die niet geschikt zijn als intermediaire laag aluminiumoxide penetratie te voorkomen. Anderzijds liet HfO_2 wel toe om een homogene film te verkrijgen na liganduitwisseling, en het kan gemakkelijk worden bedekt met Al_2O_3 om een luchtstabiele component te maken. We demonstreren een PbS/S^{2-} fototransistor met ultrahoge responsiviteit tot 920 A/W onder een backgate-spanning van −100 V. De elektronische en opto-elektronische eigenschappen van de verkregen luchtstabiele PbS fototransistor werden onderzocht. De veldeffect mobiliteit van de gaten werd berekend op 0.025 $cm^2/(V{\cdot}s)$ en 0.01 $cm^2/(V{\cdot}s)$ voor S^{2-}-getermineerde en OH^--getermineerde PbS fototransistoren, respectievelijk. Voor een PbS/S^{2-} quantum dot transistor, onder een verlichtingssterkte van 1.1 W/cm^2 bij 1550 nm , bedroeg de 3 dB bandbreedte 3 Hz onder een backgate-spanning van −100 V, en de overeenkomstige 3 dB bandbreedte was 19 Hz bij een spanning van 100 V. Voor de PbS/OH^- quantum dot transistor bedroeg de 3 dB bandbreedte 12 Hz en 17 Hz onder een backgate-spanning van −100 V en 100 V respectievelijk. Dit maakt de componenten geschikt voor lage kost beeldsensoren en detectortoepassingen.

Conclusie

Dit proefschrift onderzoekt verschillende mogelijkheden voor colloïdale quantum dot componenten voor fotodetectortoepassingen in het korte golf

infrarood golflengtebereik. Nieuwe technologie voor het definiëren van micropatronen voor colloïdale QD films werd ontwikkeld, en luchtstabiele fotogeleiders en fototransistoren met hoge responsiviteit werden verkregen op basis van deze aanpak. Deze resultaten openen nieuwe mogelijkheden voor de ontwikkeling van colloïdale quantum dot-gebaseerde opto-elektronische componenten voor toepassingen in het korte-golf infrarood golflengtegebied.

English summary

Over the past few decades, there has been a tremendous development in photonic integrated circuits towards interconnects in the 1.3-1.55 μm wavelength range due to the rapid growth of personal communication. In recent years, the scope of applications has broadened due to the rise of high volume markets such as gas sensing and bio-medical instruments. Infrared absorption spectroscopy is an important method to address novel sensing applications. However, most of the infrared spectroscopic sensing systems consist of expensive discrete components such as lasers and photodetectors. In this thesis, we demonstrate a novel approach to implement infrared photodetectors based on solution-based semiconductor colloidal quantum dots (QDs), which enable to implement a low-cost and versatile photodetector technology, amenable to integration.

The increased interests in colloidal QDs for large scale integrated photodetector applications can be attributed to three factors. First, there is the low cost of the material and fabrication. Second, the absorption wavelength can be easily adjusted by choosing a proper QD material and corresponding QD size up to the mid-infrared wavelength range. This unique property makes colloidal QDs an attractive material, especially in the wavelength range above 0.9 μm which is not sensed by crystalline silicon, a routinely-used photodetector material. The third reason is the flexibility in heterogeneous integration through a solution-based approach, which provides high potential for large scale integration on CMOS read-out circuitry or photonic integrated circuits.

Solution-processed colloidal quantum dot films

In order to implement colloidal quantum dot films suitable for photodetector applications, we aim at developing an efficient solid state ligand exchange procedure to enhance carrier transport in quantum dot films enabling optoelectronic applications. Solution-based quantum dot deposition approaches, such as drop casting and dip coating, were explored to obtain homogenous quantum dot film. Various solid state ligand exchange approaches to enhance

photoconductivity were optimized and discussed. In order to eliminate film cracks during solid state ligand exchange and to obtain crack-free QD films with sufficient thickness, a layer-by-layer QD film deposition approach was developed.

The micropatterning of layers of quantum dots with inorganic ligands using selective wet etching

The suitability of colloidal QDs for solution based processing offers the perspective to combine QD based devices with integrated electronic or photonic circuits, which requires the formation of well-defined and aligned patterns of colloidal QD layers. In the literature, different micropatterning processes have been explored, each having their own specific benefits and disadvantages. However, the deposition on a three-dimensional surface such as an electronic or photonic integrated circuit and the formation of micropatterned multiple layer QD films still remains challenging. Moreover, none of the existing approaches can be directly applied for the patterning of QD films with inorganic ligands that are typically used as absorber layer in photovoltaic cells and photodetectors or as conductive channel in field effect transistors.

In this work, we use PbS colloidal QDs to demonstrate a novel technique to pattern films of QDs stabilized by inorganic ligands. The PbS QD films are defined using a layer-by-layer approach where each cycle involves the deposition of a QD layer by dipcoating, the replacement of the native organic ligands by metal-free inorganic ligands, such as OH^- and S^{2-}, followed by a thorough cleaning of the resulting film. This results in smooth and crack-free QD films. The micropatterns are defined by a positive photoresist, followed by the removal of uncovered QDs by wet etching using an HCl/H_3PO_4 mixture. The resulting patterns can have feature dimensions down to 500 nm, limited by the resolution of the lithographic process and it is shown that the process applies to 3D substrates as well. To further evaluate the influence of this patterning technique on the properties of the colloidal QDs, films of highly luminescent CdSe/CdS core/shell are treated and micropatterned with the same technique. Photoluminescence analyses demonstrate that more than 78% of the quantum yield remains after photolithography and wet etching. This indicates that the proposed approach allows for the effective micropatterning of QD films without affecting the QD properties.

Air-stable Short-wave Infrared PbS Colloidal Quantum Dot Photoconductors passivated with Al_2O_3 Atomic layer deposition

Critical for photodetector and photovoltaic applications is the replacement of the long isolating organic ligands capping as-synthesized QDs by shorter moieties to enhance carrier mobility in QD films. Moreover, making the colloidal QD devices air-stable is of key importance for a practical application. For the purpose of obtaining air-stable QD devices, the main issue is to avoid oxidation of the QD film. This requires a well-passivating, pinhole-free layer that is transparent at the detection wavelengths. Atomic layer deposition (ALD) usually results in films without pinholes and is therefore very suitable for passivation. Al_2O_3, which is probably the most extensively characterized material in ALD, is a natural choice in this respect since it is a wide bandgap insulator that is transparent in the short-wave infrared. Al_2O_3 layers 30 nm thick are used in this work since such layers are known to be pinhole-free.

In this study, we use ALD to deposit Al_2O_3 films on PbS colloidal QD films for passivation and implement air-stable SWIR photodetectors. Homogeneous and crack-free QD films are obtained by a layer-by-layer (LBL) approach. For surface illuminated detectors, the QD films are formed on prefabricated interdigitated electrodes, where selective wet etching is used to pattern the QD film. The resulting photodetectors are then passivated with an aluminum oxide coating through ALD. Long term air-stable PbS colloidal QD photodetectors with 2.4 μm cut-off wavelength are obtained this way. For PbS/S^{2-} photodetectors, a responsivity up to 50 A/W and a specific detectivity of 3.4×10^8 Jones are obtained at 1550 nm and 300 K. For PbS/OH^- photodetectors, the responsivity is ~8 A/W and the corresponding specific detectivity is $\sim2.3\times10^8$ Jones under the same measurement conditions. The 3-dB bandwidth of the PbS/S^{2-} and PbS/OH^- photodetector is 40 Hz and 11 Hz respectively, obtained under 1.1 W/cm^2 illumination at 2250 nm wavelength. This approach can become a viable approach to realize low-cost image sensors and single pixel photodetectors.

Air-stable PbS colloidal quantum dot phototransistors

To achieve air-stable colloidal quantum dot based devices, ALD passivation was used to implement this goal. However, the photocurrent is quenched after ALD passivation, which results in a decrease in device performance. Therefore, in order to avoid the photocurrent quenching, we proposed the use of an additional layer of nanocrystal material with large bandgap as sacrificial layer to prevent alumina infilling in the PbS device layer.

This work explored two large bandgap nanocrystal materials, ZnSe and HfO_2, as sacrificial layer to improve device performance. Although both materials showcase an improved photocurrent, the difficulty of ALD growth on ZnSe with organic shell make the implementation of air-stable devices still a challenge.

Moreover, a ligand exchange procedure on ZnSe nanocrystals to enhance ALD growth usually results in inhomogeneous and discontinuous films, which are not suitable as sacrificial layer to prevent alumina penetration. On the other hand, HfO_2 allows obtaining a homogenous film after ligand exchange, and can easily be covered with Al_2O_3 to create an air-stable device. We demonstrate a PbS/S^{2-} phototransistor with ultrahigh responsivity up to 920 A/W under a back-gate voltage of –100 V. The electronic and optoelectronic properties of the obtained air-stable PbS phototransistor are investigated. The calculated field effect hole mobility is 0.025 $cm^2/(V{\cdot}s)$ and 0.01 $cm^2/(V{\cdot}s)$ for S^{2-} terminated and OH^- terminated PbS phototransistors, respectively. Under 1.1 W/cm^2 illumination at 1550 nm, for a PbS/S^{2-} quantum dot transistor, the 3-dB bandwidth is 3 Hz under a back-gate voltage of −100 V, the corresponding 3-dB bandwidth is 19 Hz in the case of back-gate voltage of 100 V. For the PbS/OH^- quantum dot transistor, the 3-dB bandwidth is 12 Hz and 17 Hz under a back-gate voltage of −100 V and 100 V, respectively, which make these devices suitable for low-cost image sensor and detector applications.

Conclusion

This thesis investigates various potentials of colloidal quantum dot devices for short-wave infrared photodetection applications. Novel micropatterning technology for colloidal quantum dot film was developed, and the corresponding air-stable photoconductors and phototransistors with high responsivity based on this approach were obtained. This results open up new possibilities for development of colloidal quantum dot based optoelectronic devices for short-wave infrared applications.

1

Introduction

1.1 Introduction of research background

According to the wavelength of electromagnetic radiation, the electromagnetic spectrum can be divided into gamma rays, X-rays, ultraviolet, visible and infrared light, the microwave and radio range (Figure 1.1 [1]). The infrared range can be further divided in the near-infrared (NIR, 0.75-1 μm), short-wave infrared (SWIR, 1-3 μm), mid-infrared (MIR, 3-8 μm) and long-wave infrared (8-12 μm) range. Over the past few decades, there has been a tremendous development in photonic integrated circuits towards interconnects in the 1.3-1.55 μm wavelength range due to the rapid growth of personal communication [2]. In recent years, the scope of applications has broadened due to the rise of high volume markets such as gas sensing [3] and bio-medical instruments [4]. However, most of the infrared spectroscopic sensing systems consist of expensive discrete components such as lasers and photodetectors [5]. In this thesis, we demonstrate a novel approach to implement infrared photodetectors based on solution-based semiconductor colloidal quantum dots (QDs), which enable to implement a low-cost and versatile photodetector technology, amenable to integration.

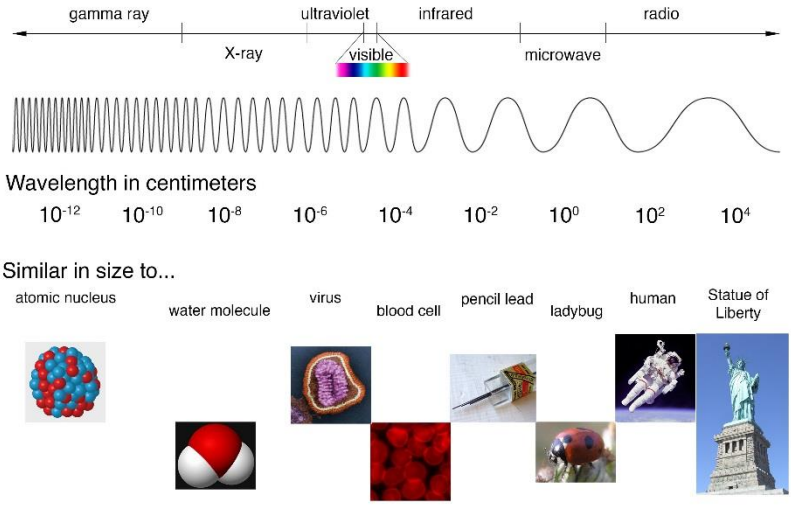

Figure 1.1: The full electromagnetic spectrum (reproduced from [1]).

1.2 Applications in the short-wave infrared range

1.2.1 Gas sensing

As shown in Figure 1.2 [6], many molecules that we want to detect or monitor in our environment have unique characteristic absorption peaks in the infrared range. This is due to the existence of atom vibration in the molecule such as stretching or twisting. When the transition energy of the molecular vibration matches the energy of incoming infrared radiation, the corresponding energy can be absorbed by the molecule. According to the material and molecular structure, each molecule has unique vibrational/rotational modes and corresponding energy levels, resulting in a unique absorption spectrum which acts as a "fingerprint" and enables their detection through infrared spectroscopy. Various molecules can be distinguished and identified corresponding to their characteristic absorption peaks through measuring the variation in transmission at different wavelengths.

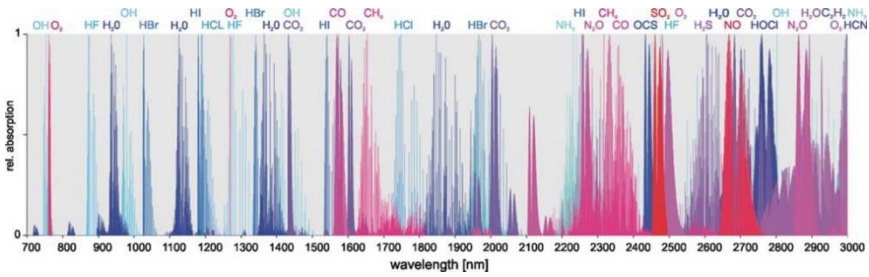

Figure 1.2: Absorption features of different gases in the 760-3000 nm wavelength range (Reproduced from [6]).

1.2.2 Enhanced vision or night vision applications

Human eyes can sense electromagnetic radiation from 390 nm to 700 nm [7], which is also called visible light. Moreover, our visual capability allows to identify the environment from reflected light just as a visible camera does. However, this capability is limited when there is insufficient light, for instance, during the night, bad weather with fog or heavy rain, a fire situation with lots of smoke, etc. Fortunately, infrared light with longer wavelength can penetrate through fog or smoke more than visible light due to the lower scattering of long-wavelength radiation. Nevertheless, certain materials such as glass may partially block mid infrared and long infrared light, which makes SWIR a promising candidate towards enhanced vision applications. A typical case is shown in Figure 1.3 [8], one can see that compared to a visible light camera, the SWIR camera (covering wavelength up to 1.7μm) contains most details, which enables to provide a safer condition for e.g. pilots or drivers. Most of the SWIR cameras and sensors are based on mercury cadmium telluride (HgCdTe) [9] or InGaAs [10] material, where an external mechanical cooling system is sometimes needed to reach low temperature and obtain the desired sensitivity. However, the high material and fabrication cost still remains an issue for large scale application of these cameras.

Figure 1.3: Images of San Francisco Bay show the difference between images produced by a visible light camera and a SWIR camera. The visible light image (left) shows mostly fog; the SWIR image (right) reveals detail through the fog. SWIR technology detects reflected light at wavelengths that the human eye cannot see, in bands of the electromagnetic spectrum between the visible and thermal infrared. (Reproduced from [8].)

1.2.3 Hyperspectral imaging

As shown in Figure 1.4 [11], hyperspectral imaging allows to collect spectral information at every location in an image of a scene. Therefore, it enables to measure the spectral features for each pixel in the image, providing additional information over a visible camera image. Considering a normal image taken by visible camera, the information only covers a narrow range of the electromagnetic spectrum, i.e. the visible range. On the contrary, hyperspectral imaging consists of a set of images which combine the full spatial and spectral information to form a three-dimensional hyperspectral data cube, i.e. (x, y, wavelength), where x and y are the two spatial dimensions of the scene in the image, and wavelength is the third (spectral) dimension.

Since small molecules or functional groups in larger molecules have characteristic absorption lines in the infrared range, several kinds of materials can be distinguished using hyperspectral imaging. Therefore, hyperspectral data which contains all the spectral information from the scene can be used for many applications, such as identifying materials [12], finding objects like oil fields [13], agriculture [14], etc.

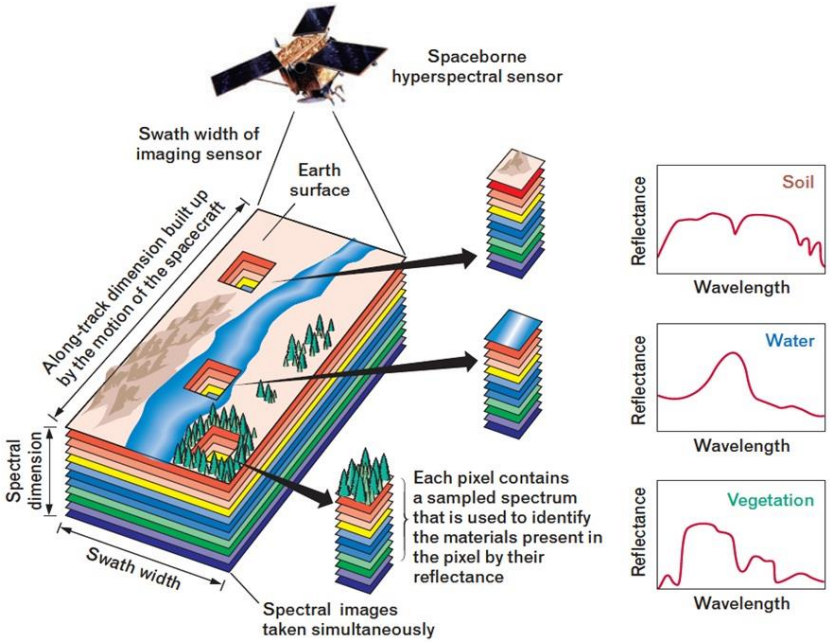

Figure 1.4: Illustration of hyperspectral imaging technique (Reproduced from [6].)

1.3 Semiconductor colloidal quantum dots as new optoelectronics material

1.3.1 Semiconductor colloidal quantum dots

Semiconductor quantum dots (QDs), which are also called semiconductor nanocrystals, are nanometer-sized crystallites that consist of hundreds to thousands of atoms. Their size usually ranges from 2 to 20 nm. Compared to bulk semiconductor material, QDs exhibit significant size-dependent properties due to size quantization. Nowadays there are mainly two approaches that can be used to obtain quantum dot material through bottom-up strategies: epitaxial QD growth through molecular beam epitaxy (MBE) [15] or metalorganic vapour phase epitaxy (MOVPE) [16], and QD synthesis through a wet, colloid chemistry approach [17-19]. The latter one is the subject of this thesis.

Compared to epitaxial growth, colloidal QD synthesis does not require any substrate and the resulting QD dispersion is compatible with various low-cost solution-based deposition approaches. In 1993, a milestone in colloidal QD synthesis was set by C. B. Murray and his colleagues through the realization of the hot injection method [18]. The theoretical study on properties of colloidal

QDs began in the early 1980s by scientists such as Ekimov [20-22], Brus [23-25] and Efros [26-28]. In 1981, Ekimov *et al* proposed that under the assumption of a spherically symmetric potential well of infinite depth, the energy shift resulting from the size quantization of a particle of mass m can be described by

$$\Delta E = \frac{\hbar^2 \pi^2}{2ma^2} \tag{1.1}$$

where a is the radius of quantum dot[21]. Assuming that the band-edges of the valence band and conduction band of a semiconductor are parabolic, the band-gap of a semiconductor will accordingly shift with the crystallite size according to:

$$E_c = E_g + \frac{\hbar^2 \pi^2}{2R^2}\left[\frac{1}{m_e} + \frac{1}{m_h}\right] \tag{1.2}$$

where m_e and m_h are the effective masses of the electron and hole, respectively. A more precise approximation proposed by Louis E.Brus in 1986 includes also the Coulomb interaction between the electron and hole that form an electron/hole pair or exciton in a QD, resulting in the Brus equation for the size-dependence of the QD band-gap transition [27]:

$$E_c = E_g + \frac{\hbar^2 \pi^2}{2R^2}\left[\frac{1}{m_e} + \frac{1}{m_h}\right] - \frac{1.8e^2}{\epsilon R} \tag{1.3}$$

where ϵ is dielectric constant. This equation shows that the band gap of a QD is larger (i.e. blue shifted) compared to the corresponding bulk semiconductor material and depends strongly on the QD size. The quantum confinement effect appears when the size of the semiconductor structure becomes comparable or smaller than the Bohr radius of the exciton a_{ex}, i.e. the most probable distance between a bound electron-hole pair or exciton in the corresponding bulk semiconductor, and results in a set of discrete energy levels.

As a result of the quantum confinement effect, the corresponding absorption and emission wavelength of colloidal quantum dots can de designed from the UV to the mid-infrared by choosing proper materials and size of QDs. Figure 1.5a shows the photoluminescence of cadmium-based colloidal quantum dot material with various size and composition in the visible range under ultraviolet excitation [29]. Colloidal QDs with longer emission/absorption wavelength into the short-wave infrared and the mid-infrared can be obtained from lead-based and mercury-based materials, respectively, and typical absorption spectra of such colloidal QDs are shown in Figure 1.5b [30] and c [19]. As a consequence, the flexible wavelength tuning and low cost make colloidal QDs very attractive

for inexpensive manufacturing of large scale devices. Over the past few years, the fast development in semiconductor fabrication, especially lithographic techniques, significantly expanded the possibility of inexpensive optoelectronic devices based on colloidal QD materials. In the following section, we will briefly introduce the state-of-the-art for optoelectronic devices based on colloidal QDs.

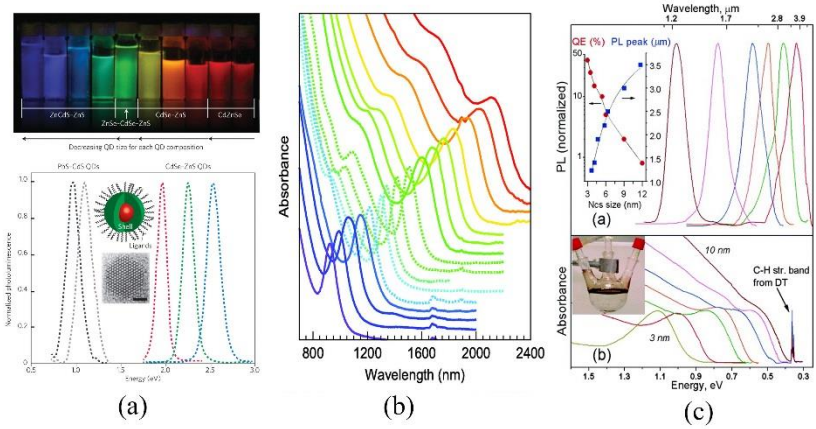

Figure 1.5: (a) Solution of colloidal QDs of varying size and composition in the visible range, exhibiting photoluminescence (PL) under optical (ultraviolet) excitation and corresponding PL spectra [29]. (b) Typical absorbance spectra of PbS QD suspensions [30]. (c) Typical PL and absorption spectra of HgTe QD suspensions, the inset shows the size dependence of the PL peaks with corresponding quantum efficiencies [19].

1.3.2 Colloidal QD photodetectors

This thesis is about the use of QD-based IR photodetectors. The increased interest in colloidal QDs for large scale integrated photodetector applications can be attributed to three factors. First, there is the low cost of the material and fabrication. Second, the absorption wavelength can be easily adjusted by choosing a proper QD material and corresponding QD size up to the mid-infrared range. This unique property makes colloidal QDs an attractive material, especially in the wavelength range above 0.9 μm which is not sensed by crystalline silicon, a routinely used photodetector material. The third reason is the flexibility in heterogeneous integration through a solution-based approach, which provides high potential for large scale integration on complementary metal-oxide-semiconductor (CMOS) read-out circuitry or photonic integrated circuits.

Generally, photodetector devices can be divided into photoconductors, phototransistors and photodiodes, based on the device geometries. The corresponding schematic illustrations of device architecture and configurations are shown in Figure 1.6 [35]. The photoconductivity of a photodetector originates from two kinds of photocurrent: the primary photocurrent, which originates directly from the extraction of photogenerated carriers and a secondary photocurrent which can be attributed to the injection and transit of charge carriers from the electrodes. The latter is generally accompanied with photoconductive gain. This is due to the fact that minority carriers get trapped by trap states, while the majority carriers are capable to circulate through the external circuit for many times until they recombine with the minority carriers, i.e. the life time of the majority carrier exceeds the transit time of the majority carrier.

In the case of PbS colloidal QDs, Klimov *et al.* indicated that midgap trap states can be introduced during a solid-state ligand exchange procedure [36]. The photoconductive gain in PbS colloidal QD detectors based on solid-state ligand exchange is principally determined by the occupancy of these midgap trap states, corresponding to the illumination intensity of the incident light [35]. At low level of illumination intensity, the density of trap states is higher than the density of photo-induced charge carriers. For instance, in a p–type colloidal QD film where holes can transit to the external circuit and electrons are trapped, the corresponding midgap trap states are partially filled at low light levels and photoconductive gain exists. At high illumination intensity, the trap states are filled more and the corresponding photoconductive gain reduces or even vanishes when the trap state are fully filled. Therefore, the photoconductive gain and corresponding responsivity of colloidal QD photoconductors exhibit a strong dependence on illumination intensity.

Phototransistors as a second type of photodetector are different compared to photoconductors due to the three terminal electrical contact architecture (Figure 1.6b). The existing gate voltage offers control over the drain-source current flow in the channel. The midgap trap states of the QD film can be populated or depopulated depending on the gate voltage, and the corresponding Fermi level can be adjusted. The third type of photodetector is the photodiode. Unlike photoconductors and phototransistors which are capable to have high gain, the quantum efficiency in a photodiode is generally smaller than unity (except if avalanche multiplication takes place). This is due to the fact that photogenerated electrons and holes in a photodiode are separated directly by the built-in electric field which origins from the spatial bending of bands, then move in an opposite direction and are collected by electrodes. An efficient collection of photoexcited carriers in a photodiode requires a carrier life time longer than the carrier transit time, which can be implemented by optimizing device thickness and carrier diffusion length. Compared to photoconductors, generally photodiodes can have

a much faster response time due to the faster carrier transport in the depletion region. According to the material stack, devices can be further divided into Schottky type, heterojunction type, p-n junction and p-i-n junction type.

The research on colloidal QD photodetectors was first launched in the visible range with cadmium-based material by Bawendi *et al.* [37-39]. Afterwards the working wavelength was extended to the near-infrared region up to 1.6 μm through lead-based QD material, and tremendous efforts were made by the Sargent Group in this field [40-42]. In the mid-infrared wavelength range, Hg-based colloidal QD material is routinely used because of the narrow bandgap property and wavelength tunability in the 3-5 μm range. An inkjet-printed HgTe colloidal QD photodetector operating up to 3 μm wavelength was obtained by Böberl *et al.* [43]. HgTe photodetectors with even longer working wavelength up to 5 μm were obtained by Lhuillier *et al.* and reported in [44].

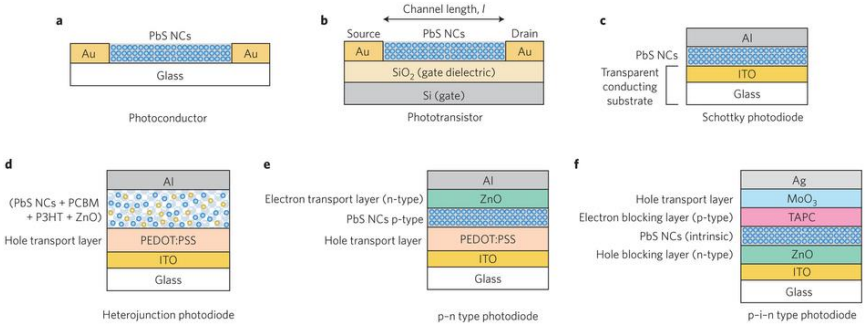

Figure 1.6: Device architecture and configuration of colloidal QD-based photodetectors. (a) A simple photoconductor device architecture. (b) A bottom gate phototransistor device. (c) A Schottky-type photodiode configuration. (d) A bulk heterojunction photodiode with QD-polymer blended film. (e) A p-n junction photodiode device. (f) A vertically stacked p-i-n photodiode device. (Reproduced from [35])

1.3.3 Colloidal QDs in solar cell applications

As a new optoelectronics material with very low lost, colloidal QDs do not only attract attention for photodetector applications, it is also considered for photovoltaics. The broadband absorption of colloidal QDs as solar cell sensitizers allows its working range to expand to the red and near-infrared range. Generally there are four types of colloidal QD based solar cells explored by scientists: the QD-polymer hybrid solar cells, the Schottky solar cell, the depleted heterojunction solar cells and the colloidal QD-sensitized solar cells (QDSSCs). The schematic illustrations for these four types of solar cells are shown in Figure 1.7 [45]. Hybrid solar cells are also called bulk-heterojunction

donor-acceptor solar cells, which blend colloidal QDs and conductive polymer as p-type and n-type material. The heterojunction on the interfaces of QDs and conductive polymer offers efficient charge separation through a percolation approach and solar cells based on this structure were reported by Huynh and his co-workers [46]. However, the conductive polymer as QD linker has low stability. In order to avoid performance degeneration, Schottky solar cells based on colloidal QDs were proposed. They can be implemented by embedding a colloidal QD solid between ITO-coated glass and a metal contact like Al or Mg to form a simple Schottky junction, normally accompanied by a ligand exchange procedure on the colloidal QDs. A built-in field is formed at the QD-metal interface to separate photogenerated carriers: holes are collected by the ITO and electrons are collected by the metal contact, respectively. Recent power conversion efficiencies are 4.5% and 6% obtained using PbSe [47] and PbS QDs [48], respectively. Compared to a Schottky solar cell, the depleted heterojunction solar cell has an additional transparent conducting oxide layer as electron-acceptor to enhance minority-carrier separation. A high power conversion efficiency of 8.55% was reported by Chuang *et al.* using a room-temperature solution processed ZnO/PbS QD solar cell [49]. Colloidal QDSSCs contain a QD-sensitized electrode and a counter electrode. The QD-sensitized electrode is highly porous and consists of semiconductor colloidal QDs and redox-coupling electrolyte. Two kinds of colloidal QD materials are used: semiconductor QDs such as InP as sensitizer and TiO_2 QDs as nanoporous electrodes with large interface area for efficient carrier transport. Colloidal QDs as sensitizer can absorb light and the photogenerated electrons are injected in the TiO_2 electrode. Afterwards, the QDs are reduced by the infiltrated redox-coupling electrolyte. Through a QDSSC structure, a power conversion efficiency beyond 8% was reported in [50].

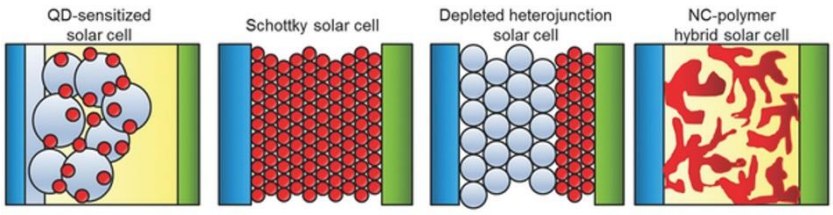

Figure 1.7: Schematic diagrams showing the four representative types of QD solar cells: the colloidal QD-sensitized solar cells, the Schottky solar cell, the depleted-junction solar cell and the QD-polymer hybrid solar cell [45].

1.3.4 Colloidal QDs light-emitting devices

In addition to using colloidal QDs as light harvesting materials, they can be also used as light emitting devices such as light emitting diodes (LEDs) due to the narrow emission band and tunability of emission wavelength. Generally a colloidal QD-based LED consists of an active QD layer as light-emitting material, which is sandwiched between a hole transport layer (HTL) and an electron transport layer (ETL). The HTL and ETL are used to implement efficient carrier injection into the colloidal QD film. Under external bias voltage, holes and electrons are injected from HTL and ETL, respectively. Then the electron-hole pairs recombine in the colloidal QD layer and photons are generated. The wavelength of the emitted photons is determined by the bandgap of the colloidal QD layer, i.e. the energy difference between the lowest unoccupied states and highest occupied states in the QD film. A schematic illustration of a typical colloidal QD based LED is shown in Figure 1.8 [51]. In 1994, the first colloidal QD based LED based on CdSe material was reported in [52] by the Alivisatos Group. After that many efforts have been made to improve the performance of QD-based LED devices, such as using colloidal QDs with core-shell structure to obtain high color purity and enhance resistance against oxidization [53], optimization of the QD layer thickness to obtain better efficiency and luminescence [54], choosing HTL and ETL with proper conduction and valence band energy to improve carrier injection and device efficiency [55], etc. In recent years, the electroluminescence wavelength of colloidal QD-based LEDs is extended from the visible range to the near-infrared range by using a small bandgap material such as silicon [56] or PbS QDs [57]. These developments make colloidal QD-based LEDs promising candidates for a broad range of appilications, including large-area displays, lighting devices and short-reach fiber-optic communication.

1.4 Structure of thesis

In this Chapter, we reviewed the background of short-wave infrared spectroscopy and semiconductor colloidal quantum dots with their applications. Given the above discussion, we aim for demonstrating a novel approach to implement photodetectors based on solution-based semiconductor QDs, which enables to implement a low-cost and versatile photodetector technology, amenable to integration.

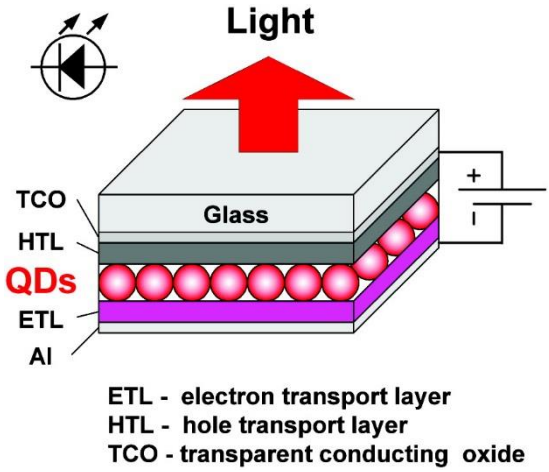

Figure 1.8: Schematic illustration and a typical structure of a thin film LED based on colloidal QD material [51].

In Chapter 2, we explore various solution-based film preparation methods to obtain a homogenous, crack-free quantum dot film. We also develop an efficient solid state ligand exchange approach with metal-free inorganic ligands, S^{2-} and OH^{-}, to enhance carrier transport thereby enabling further optoelectronic applications.

Chapter 3 presents a novel technique to pattern colloidal quantum dot films with inorganic ligands. The PbS QD films are fabricated using a layer-by-layer (LBL) approach. The micropatterns are defined by a positive photoresist, followed by the removal of uncovered QDs by wet etching using an HCl/H_3PO_4 mixture. The resulting patterns can have feature dimensions down to 500 nm, limited by the resolution of the lithographic process and it is shown that the process applies to 3D substrates as well. In addition, highly luminescent CdSe/CdS core/shell are treated and micropatterned with the same technique. Photoluminescence analyses demonstrate that more than 90% of the quantum yield remains after photolithography and wet etching. This indicates the proposed approach provides a pathway to implement large scale QD-based optoelectronic integration devices.

In Chapter 4, we use an atomic layer deposition (ALD) approach to deposit Al_2O_3 films on PbS colloidal QD films for passivation and implement air-stable SWIR photodetectors. For surface illuminated detectors, the QD films are formed on prefabricated interdigitated electrodes, where selective wet etching is used to pattern the QD film. Long term air-stable PbS colloidal QD photodetectors with high responsivity (50 A/W for PbS/S^{2-} photodetectors and 8 A/W for PbS/OH^{-} photodetectors) and 2.4 μm cut-off wavelength are obtained.

In order to avoid photocurrent quenching due to the ALD deposition, large bandgap nanocrystal materials, ZnSe and HfO_2, are explored as sacrificial layer to improve device performance in Chapter 5. Air-stable PbS/S^{2-} phototransistors with ultrahigh responsivity up to 920 A/W under a back-gate voltage of –100 V are obtained. We also present the electronic and optoelectronic properties of the obtained phototransistors. The 3dB bandwidth of the PbS/S^{2-} and PbS/OH^- phototransistors is 20 Hz and 11 Hz respectively under 1.1 W/cm^2 illumination at 1550 nm, which make these device suitable for low-cost imaging sensor and detector applications.

In Chapter 6, we summarize the work of this thesis and also discuss the future prospects toward further performance improvements of the devices.

1.5 Publications

Publications in international journals

1. **C. Hu**, A. Gassenq, Y. Justo, K. Devloo-Casier, H. Chen, C. Detavernier, Z. Hens, and G. Roelkens, "Air-stable short-wave infrared PbS colloidal quantum dot photoconductors passivated with Al2O3 atomic layer deposition," Applied Physics Letters 105, (2014).
2. **C. Hu**, Tangi Aubert, Yolanda Justo, Stijn Flamee, Marco Cirillo, A. Gassenq, Oksana Drobchak, Filip Beunis, G. Roelkens, Zeger Hens, "Micropatterning of Layers of Colloidal Quantum Dots with Inorganic Ligands Using Selective Wet Etching," Nanotechnology, 25, 175302 (2014).
3. S. Vandewiele, T. Brans, L. Van Landschoot, K. Komorowska, S. Verstuyft, A. Subramanian, **C. Hu**, F. Beunis, and R. Baets, "Single-mode air-clad liquid-core waveguides on a surface energy patterned substrate," Opt. Lett. 39, 4942-4945 (2014).
4. G. Roelkens, U. D. Dave, A. Gassenq, N. Hattasan, **C. Hu**, B. Kuyken, F. Leo, A. Malik, M. Muneeb, E. Ryckeboer, D. Sanchez, S. Uvin, R. Wang, Z. Hens, R. Baets, Y. Shimura, F. Gencarelli, B. Vincent, R. Loo, J. V. Campenhout, L. Cerutti, J. B. Rodriguez, E. Tourni, X. Chen, M. Nedeljkovic, G. Mashanovich, L. Shen, N. Healy, A. C. Peacock, X. Liu, R. Osgood, and W. M. J. Green, "Silicon-Based Photonic Integration Beyond the Telecommunication Wavelength Range," Ieee J Sel Top Quant 20, 394-404 (2014).
5. G. Roelkens, U. Dave, A. Gassenq, N. Hattasan, **C. Hu**, B. Kuyken, F. Leo, A. Malik, M. Muneeb, E. Ryckeboer, S. Uvin, Z. Hens, R. Baets, Y.

Shimura, F. Gencarelli, B. Vincent, R. Loo, J. Van Campenhout, L. Cerutti, J.-B. Rodriguez, E. Tournié, X. Chen, M. Nedeljkovic, G. Mashanovich, L. Shen, N. Healy, A. C. Peacock, X. Liu, R. Osgood, and W. Green, "Silicon-based heterogeneous photonic integrated circuits for the mid-infrared," Opt. Mater. Express 3, 1523-1536 (2013).

Publications in international conferences

1. **C. Hu**, A. Gassenq, Y. Justo Zarraquiños, K. Devloo-Casier, H. Chen, H. Zhao, C. Detavernier, Z. Hens, and G. Roelkens, "Short-wave infrared PbS colloidal quantum dot photodetectors with AlOx atomic layer deposition passivation," in 12th Conference on Mid-IR Optoelectronics: Materials and Devices (MIOMD 2014) (2014).
2. G. Roelkens, U.D. Dave, A. Gassenq, N. Hattasan, **C. Hu**, B. Kuyken, F. Leo, A. Malik, M. Muneeb, E.M.P. Ryckeboer, D. Sanchez, S. Uvin, R. Wang, Z. Hens, R. Baets, Y. Shimura, F. Gencarelli, B. Vincent, R. Loo, J. Van Campenhout, L. Cerutti, J.B. Rodriguez, E. Tournie, X. Chen, M. Nedeljkovic, G. Mashanovich, L. shen, N. Healy, A. Peacock, X. Liu, R. Osgood, W. Green, "Long-wavelength silicon photonic integrated circuits," in 11th International Conference on Group IV Photonics (GFP)(IEEE, 2014), 23-24 (2014).
3. **C. Hu**, A. Gassenq, Y. Justo, S. Yakunin, W. Heiss, Z. Hens, G. Roelkens, Short-wave infrared colloidal quantum dot photodetectors on silicon, 2013 SPIE Photonics West Conference, United States, 863127-863128 (2013).
4. **C. Hu**, A. Gassenq, E. M. Ryckeboer, Y. Justo, Z. Hens, and G. Roelkens, "Colloidal PbS Quantum Dot Photodetectors for Short-wave Infrared applications", Proceedings of the 2013 Annual Symposium of the IEEE Photonics Society Belenux Chapter, Netherlands, 41-44 (2013).
5. **C. Hu**, T. Aubert, Yolanda Justo, S. Flamee, A. Gassenq, G. Roelkens, Z. Hens, "Micropatterning of Colloidal Quantum Dot Layers by Selective Wet Etching, " E-MRS 2013 Spring Meeting, France, (2013).
6. **C. Hu**, A. Gassenq, Y. Justo, Z. Hens, G. Roelkens, "Colloidal Quantum Dot Photodetectors on Silicon for Short-wave Infrared applications, " E-MRS 2013 Spring Meeting, France, (2013).
7. G. Roelkens, B. Kuyken, F. Leo, N. Hattasan, E.M.P. Ryckeboer, M. Muneeb, **C. Hu**, A. Malik, Z. Hens, R. Baets, Y. Shimura, F. Gencarelli, B. Vincent, R. Loo, P. Verheyen, G. Lepage , J. Van Campenhout, L. Cerutti, J.B. Rodriguez, E. Tournie, X. Chen, M. Nedeljkovic, G.

Mashanovich, X. Liu, W. Green, "Long-wavelength III-V/silicon photonic integrated circuits," Advanced Photonics - OSA Optics & Photonics Congress (invited), United States, p.paper IT2A.1 (2013).

8. G. Roelkens, U.D. Dave, A. Gassenq, N. Hattasan, **C. Hu**, B. Kuyken, F. Leo, A. Malik, M. Muneeb, E.M.P. Ryckeboer, S. Uvin, Z. Hens, R. Baets, Y. Shimura, F. Gencarelli, B. Vincent, R. Loo, J. Van Campenhout, L. Cerutti, J. Rodriguez, E. Tournie, X. Chen, M. Nedeljkovic, G.Z. Mashanovich, L. Shen, N. Healy, A.C. Peacock, X. Liu, R. M. Osgood, W. Green, "Mid-IR heterogeneous silicon photonics," in SPIE OPTO (International Society for Optics and Photonics, 2013), 899316-899316 (2013).

References

[1] The full electromagnetic spectrum, NASA. http://imagine.gsfc.nasa.gov/science/toolbox/spectra1.html.

[2] C. Gunn, "CMOS Photonics for High-Speed Interconnects," IEEE Micro 26, 58-66 (2006).

[3] K. D. Vos, J. Girones, T. Claes, Y. D. Koninck, S. Popelka, E. Schacht, R. Baets, and P. Bienstman, "Multiplexed Antibody Detection With an Array of Silicon-on-Insulator Microring Resonators," IEEE Photonics Journal 1, 225-235 (2009).

[4] Y. Li, and R. Baets, "Homodyne laser Doppler vibrometer on silicon-on-insulator with integrated 90 degree optical hybrids," Opt. Express 21, 13342-13350 (2013).

[5] J. Crowder, S. Smith, A. Vass, and J. Keddie, "Infrared methods for gas detection," in Mid-Infrared Semiconductor Optoelectronics(Springer, 2006), pp. 595-613.

[6] W. Zeller, L. Naehle, P. Fuchs, F. Gerschuetz, L. Hildebrandt, and J. Koeth, "DFB Lasers Between 760 nm and 16 μm for Sensing Applications," Sensors 10, 2492 (2010)..

[7] C. Starr, C. Evers, and L. Starr, Biology: Concepts and applications without physiology (Cengage Learning, 2010).

[8] https://spinoff.nasa.gov/Spinoff2010/ip_2.html.

[9] L. O. Bubulac, W. E. Tennant, J. G. Pasko, L. J. Kozlowski, M. Zandian, M. E. Motamedi, R. E. De Wames, J. Bajaj, N. Nayar, W. V. McLevige, N. S. Gluck, R. Melendes, D. E. Cooper, D. D. Edwall, J. M. Arias, R. Hall, and A. I. D'souza, "High performance SWIR HgCdTe detector arrays," Journal of Elec Materi 26, 649-655 (1997).

[10] B. M. Onat, W. Huang, N. Masaun, M. Lange, M. H. Ettenberg, and C. Dries, "Ultra-low dark current InGaAs technology for focal plane arrays for low-light level visible-shortwave infrared imaging," (2007), pp. 65420L-65420L-65429.

[11] http://www.markelowitz.com/Hyperspectral.html.

[12] B. Johnson, R. Joseph, M. L. Nischan, A. B. Newbury, J. P. Kerekes, H. T. Barclay, B. C. Willard, and J. J. Zayhowski, "Compact active hyperspectral imaging system for the detection of concealed targets," (1999), pp. 144-153.

[13] J. Ellis, H. Davis, and J. Zamudio, "Exploring for onshore oil seeps with hyperspectral imaging," Oil and Gas Journal 99, 49-58 (2001).

[14] J. Xing, P. Van Hung, S. Symons, M. Shahin, and D. Hatcher, "Using a Short Wavelength Infrared (SWIR) hyperspectral imaging system to predict alpha amylase activity in individual Canadian western wheat kernels," Sensing and Instrumentation for Food Quality and Safety 3, 211 (2009).

[15] D. Leonard, M. Krishnamurthy, S. Fafard, J. L. Merz, and P. M. Petroff, "Molecular - beam epitaxy growth of quantum dots from strained coherent uniform islands of InGaAs on GaAs," Journal of Vacuum Science & Technology B 12, 1063-1066 (1994).

[16] Kazuhide Kumakura, Kazuaki Nakakoshi, Junichi Motohisa, Takashi Fukui, and Hideki Hasegawa, "Novel Formation Method of Quantum Dot Structures by Self-Limited Selective Area Metalorganic Vapor Phase 0 Epitaxy," Japanese Journal of Applied Physics 34, 4387 (1995).

[17] C. B. Murray, D. J. Norris, and M. G. Bawendi, "Synthesis and characterization of nearly monodisperse CdE (E = sulfur, selenium, tellurium) semiconductor nanocrystallites," Journal of the American Chemical Society 115, 8706-8715 (1993).

[18] L. Cademartiri, E. Montanari, G. Calestani, A. Migliori, A. Guagliardi, and G. A. Ozin, "Size-Dependent Extinction Coefficients of PbS Quantum Dots," Journal of the American Chemical Society 128, 10337-10346 (2006).

[19] M. V. Kovalenko, E. Kaufmann, D. Pachinger, J. Roither, M. Huber, J. Stangl, G. Hesser, F. Schäffler, and W. Heiss, "Colloidal HgTe Nanocrystals with Widely Tunable Narrow Band Gap Energies: From Telecommunications to Molecular Vibrations," Journal of the American Chemical Society 128, 3516-3517 (2006).

[20] A. I. Ekimov, and A. A. Onushchenko, "Quantum size effect in three-dimensional microscopic semiconductor crystals," ZhETF Pisma Redaktsiiu 34, 363 (1981).

[21] A. Ekimov, and A. Onushchenko, "Size quantization of the electron energy spectrum in a microscopic semiconductor crystal," Jetp Lett 40, 1136-1139 (1984).

[22] A. I. Ekimov, A. L. Efros, and A. A. Onushchenko, “Quantum Size Effect in Semiconductor Microcrystals,” Solid State Commun. 56(11), 921-924 (1985).

[23] L. Brus, "Electronic wave functions in semiconductor clusters: experiment and theory," The Journal of Physical Chemistry 90, 2555-2560 (1986).

[24] L. E. Brus, "Electron – electron and electron - hole interactions in small semiconductor crystallites: The size dependence of the lowest excited electronic state," The Journal of Chemical Physics 80, 4403-4409 (1984).

[25] M. G. Bawendi, M. L. Steigerwald, and L. E. Brus, "The quantum mechanics of larger semiconductor clusters (" quantum dots")," Annual Review of Physical Chemistry 41, 477-496 (1990).

[26] G. Medeiros-Ribeiro, F. G. Pikus, P. M. Petroff, and A. L. Efros, "Single-electron charging and Coulomb interaction in InAs self-assembled quantum dot arrays," Physical Review B 55, 1568-1573 (1997).

[27] A. L. Efros and, and M. Rosen, "The Electronic Structure of Semiconductor Nanocrystals," Annual Review of Materials Science 30, 475-521 (2000).

[28] D. J. Norris, A. L. Efros, M. Rosen, and M. G. Bawendi, "Size dependence of exciton fine structure in CdSe quantum dots," Physical Review B 53, 16347-16354 (1996).

[29] Y. Shirasaki, G. J. Supran, M. G. Bawendi, and V. Bulovic, "Emergence of colloidal quantum-dot light-emitting technologies," Nat Photon 7, 13-23 (2013).

[30] I. Moreels, Y. Justo, B. De Geyter, K. Haustraete, J. C. Martins, and Z. Hens, "Size-Tunable, Bright, and Stable PbS Quantum Dots: A Surface Chemistry Study," ACS Nano 5, 2004-2012 (2011).

[31] K. Szendrei, F. Cordella, M. V. Kovalenko, M. Böberl, G. Hesser, M. Yarema, D. Jarzab, O. V. Mikhnenko, A. Gocalinska, and M. Saba, "Solution - Processable Near - IR Photodetectors Based on Electron Transfer from PbS Nanocrystals to Fullerene Derivatives," Advanced Materials 21, 683-687 (2009).

[32] C. A. Leatherdale, C. R. Kagan, N. Y. Morgan, S. A. Empedocles, M. A. Kastner, and M. G. Bawendi, "Photoconductivity in CdSe quantum dot solids," Physical Review B 62, 2669-2680 (2000).

[33] H. Kim, K. Cho, H. Song, B. Min, J.-S. Lee, G.-T. Kim, S. Kim, S. H. Kim, and T. Noh, "Photocurrent mechanism in a hybrid system of 1-thioglycerol-capped HgTe nanoparticles," Applied Physics Letters 83, 4619-4621 (2003).

[34] H. Wei, Y. Fang, Y. Yuan, L. Shen, and J. Huang, "Trap Engineering of CdTe Nanoparticle for High Gain, Fast Response, and Low Noise

P3HT:CdTe Nanocomposite Photodetectors," Advanced Materials 27, 4975-4981 (2015).

[35] R. Saran, and R. J. Curry, "Lead sulphide nanocrystal photodetector technologies," Nat Photon 10, 81-92 (2016).

[36] P. Nagpal, and V. I. Klimov, "Role of mid-gap states in charge transport and photoconductivity in semiconductor nanocrystal films," Nat Commun 2, 486 (2011).

[37] C. A. Leatherdale, C. R. Kagan, N. Y. Morgan, S. A. Empedocles, M. A. Kastner, and M. G. Bawendi, "Photoconductivity in CdSe quantum dot solids," Physical Review B 62, 2669-2680 (2000).

[38] M. V. Jarosz, V. J. Porter, B. R. Fisher, M. A. Kastner, and M. G. Bawendi, "Photoconductivity studies of treated CdSe quantum dot films exhibiting increased exciton ionization efficiency," Physical Review B 70, 195327 (2004).

[39] V. J. Porter, S. Geyer, J. E. Halpert, M. A. Kastner, and M. G. Bawendi, "Photoconduction in Annealed and Chemically Treated CdSe/ZnS Inorganic Nanocrystal Films," The Journal of Physical Chemistry C 112, 2308-2316 (2008).

[40] G. Konstantatos, I. Howard, A. Fischer, S. Hoogland, J. Clifford, E. Klem, L. Levina, and E. H. Sargent, "Ultrasensitive solution-cast quantum dot photodetectors," Nature 442, 180-183 (2006).

[41] G. Konstantatos, J. Clifford, L. Levina, and E. H. Sargent, "Sensitive solution-processed visible-wavelength photodetectors," Nat Photon 1, 531-534 (2007).

[42] J. P. Clifford, G. Konstantatos, K. W. Johnston, S. Hoogland, L. Levina, and E. H. Sargent, "Fast, sensitive and spectrally tuneable colloidal-quantum-dot photodetectors," Nat Nano 4, 40-44 (2009).

[43] M. Böberl, M. V. Kovalenko, S. Gamerith, E. J. W. List, and W. Heiss, "Inkjet-Printed Nanocrystal Photodetectors Operating up to 3 μm Wavelengths," Advanced Materials 19, 3574-3578 (2007).

[44] E. Lhuillier, S. Keuleyan, P. Zolotavin, and P. Guyot-Sionnest, "Mid-Infrared HgTe/As2S3 Field Effect Transistors and Photodetectors," Advanced Materials 25, 137-141 (2013).

[45] J. Yang, M. K. Choi, D.-H. Kim, and T. Hyeon, "Designed Assembly and Integration of Colloidal Nanocrystals for Device Applications," Advanced Materials 28, 1176-1207 (2016).

[46] W. U. Huynh, J. J. Dittmer, and A. P. Alivisatos, "Hybrid Nanorod-Polymer Solar Cells," Science 295, 2425-2427 (2002).

[47] O. E. Semonin, J. M. Luther, S. Choi, H.-Y. Chen, J. Gao, A. J. Nozik, and M. C. Beard, "Peak External Photocurrent Quantum Efficiency Exceeding 100% via MEG in a Quantum Dot Solar Cell," Science 334, 1530-1533 (2011).

[48] J. Tang, K. W. Kemp, S. Hoogland, K. S. Jeong, H. Liu, L. Levina, M. Furukawa, X. Wang, R. Debnath, D. Cha, K. W. Chou, A. Fischer, A. Amassian, J. B. Asbury, and E. H. Sargent, "Colloidal-quantum-dot photovoltaics using atomic-ligand passivation," Nat Mater 10, 765-771 (2011).

[49] C.-H. M. Chuang, P. R. Brown, V. Bulović, and M. G. Bawendi, "Improved performance and stability in quantum dot solar cells through band alignment engineering," Nat Mater 13, 796-801 (2014).

[50] K. Zhao, Z. Pan, I. Mora-Seró, E. Cánovas, H. Wang, Y. Song, X. Gong, J. Wang, M. Bonn, J. Bisquert, and X. Zhong, "Boosting Power Conversion Efficiencies of Quantum-Dot-Sensitized Solar Cells Beyond 8% by Recombination Control," Journal of the American Chemical Society 137, 5602-5609 (2015).

[51] D. V. Talapin, J.-S. Lee, M. V. Kovalenko, and E. V. Shevchenko, "Prospects of colloidal nanocrystals for electronic and optoelectronic applications," Chemical reviews 110, 389-458 (2009).

[52] V. Colvin, M. Schlamp, and A. P. Alivisatos, "Light-emitting-diodes made from cadmium selenide nanocrystals and a semiconducting polymer," Nature 370, 354-357 (1994).

[53] M. C. Schlamp, X. Peng, and A. P. Alivisatos, "Improved efficiencies in light emitting diodes made with CdSe(CdS) core/shell type nanocrystals and a semiconducting polymer," Journal of Applied Physics 82, 5837-5842 (1997).

[54] W. K. Bae, J. Kwak, J. Lim, D. Lee, M. K. Nam, K. Char, C. Lee, and S. Lee, "Multicolored Light-Emitting Diodes Based on All-Quantum-Dot Multilayer Films Using Layer-by-Layer Assembly Method," Nano Letters 10, 2368-2373 (2010).

[55] B. S. Mashford, M. Stevenson, Z. Popovic, C. Hamilton, Z. Zhou, C. Breen, J. Steckel, V. Bulovic, M. Bawendi, S. Coe-Sullivan, and P. T. Kazlas, "High-efficiency quantum-dot light-emitting devices with enhanced charge injection," Nat Photon 7, 407-412 (2013).

[56] K.-Y. Cheng, R. Anthony, U. R. Kortshagen, and R. J. Holmes, "High-Efficiency Silicon Nanocrystal Light-Emitting Devices," Nano Letters 11, 1952-1956 (2011).

[57] L. Sun, J. J. Choi, D. Stachnik, A. C. Bartnik, B.-R. Hyun, G. G. Malliaras, T. Hanrath, and F. W. Wise, "Bright infrared quantum-dot light-emitting diodes through inter-dot spacing control," Nat Nano 7, 369-373 (2012).

2

Solution-processed colloidal quantum dot films

2.1 Introduction

The capability of light detection with high sensitivity in the short-wave infrared range is key for enhanced vision systems including night-vision, sensing through fog and hyperspectral imaging. Traditional high-sensitivity photodetectors used in these systems are based on III-V epitaxial materials [1, 2]. While III-V semiconductors lead to the highest performance, the high material and integration cost prohibits large volume applications. Low-cost MidIR photodetectors based on colloidal quantum dots (QDs) offer an alternative way to realize this functionality, either as discrete components, focal plane arrays or integrated on photonic integrated circuits [3-5]. By tuning the size of the quantum dots, the electrical and optical properties (such as the absorption cut-off wavelength) can be tuned due to the quantum size effect [6, 7]. Moreover, by choosing different materials, such as CdSe, PbS, HgTe, etc., the emission and absorption spectrum can range from the ultraviolet to the mid-infrared range [6-8].

In this chapter, we aim at developing an efficient solid state ligand exchange procedure to enhance carrier transport in quantum dot films enabling

optoelectronic applications. Solution-based quantum dot deposition approaches, such as drop casting and dip coating, were explored to obtain homogenous quantum dot films. Various solid state ligand exchange approaches to enhance photoconductivity are optimized and discussed. In order to eliminate film cracks during solid state ligand exchange and to obtain crack-free QD films with sufficient thickness, a layer-by-layer (LBL) QD film deposition approach was developed. The demonstration of a first generation of solution-processed PbS colloidal quantum dot photoconductors through this approach is also discussed.

2.2 Synthesis of colloidal quantum dots

The synthesis of OlAm-terminated PbS quantum dots was based on the method developed by Cademartiri *et al* [9] and described in detail in [10]. A stock solution was prepared by heating a mixture of 0.16 g (5 mmol) S in 15 mL of OlAm under nitrogen for 30 min at 120 ℃. In the first step of the synthesis, a mixture of 0.834 g (3 mmol) of $PbCl_2$ and 7.5 mL of OlAm in a three-neck flask was degassed under nitrogen for 30 min at 125 ℃. After that, the mixed $PbCl_2$ solution was heated up to reach the required injection temperature, and then a mixture of 2.25 mL of the OlAm-S stock solution (0.75 mmol of S) and 170 μL (375 μmol, half of the amount of S) of TOP were injected into the flask. After injection, the temperature dropped by ~ 5-10 ℃, and the resulting growth temperature was maintained through the whole reaction. After the designed growth time, the reaction was quenched by adding a mixture of 10 mL of toluene and 15 mL of MeOH. The resulting synthesis suspension was centrifuged and the supernatant was removed by decantation, after which the PbS QDs were resuspended in 10 mL of toluene. For the PbS QDs studied in this thesis, the growth temperature was 160 ℃ and the growth time was 2 h 30 min. After synthesis, the OlAm ligands were replaced by oleic acid (OlAc) to obtain a ligand shell that can stand successive purification cycles. The ligand exchange was realized by adding OlAc to a toluene suspension of PbS QDs in a volume ratio of 1.5:10 OlAc/toluene. Afterwards, the suspension was purified using methanol (MeOH) and toluene as the non-solvent and the solvent, respectively. Typically, the ligand exchange was repeated twice. After a final precipitation with MeOH, the PbS QDs were resuspended in toluene. The concentration of the resulting QD suspension was determined from the QD absorbance spectrum through the molar extinction coefficient at 400 nm (ϵ_{400}) [10].

For the QD solution used in this work, Moreels et al. have constructed a size curve to relate the TEM QD diameter to the QD bandgap E_0 (eV) measured through absorbance spectroscopy and shown in Figure 2.1 [10]. This allows to

determine the size d (nm) of the QDs directly from the first absorption peak of the absorbance spectrum [10], i.e.:

$$E_0 = 0.41 + \frac{1}{0.0252d^2 + 0.283d} \tag{2.1}$$

The QD molar extinction coefficient at 400 nm can be determined by

$$\epsilon_{400} = 0.0234 \cdot d^3, \text{cm}^{-1}/\mu\text{M} \tag{2.2}$$

Moreover, the QD solution concentration c_0 can be obtained directly from the absorbance at 400 nm A_{400} by using Beer's law:

$$A = \epsilon_{400} \cdot c_0 \cdot L \tag{2.3}$$

where L is the sample length.

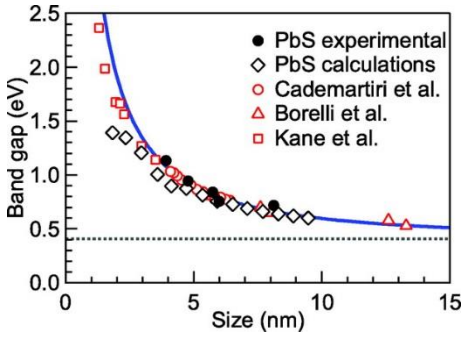

Figure 2.1: Relation between the PbS quantum dot band gap and the particle size. (Reproduced from [10].)

2.3 Fabrication of quantum dot solids

Unlike traditional epitaxial inorganic semiconductor QD materials, which are normally obtained using a high cost epitaxial growth technique, such as molecular beam epitaxy (MBE) [11] or metalorganic chemical vapor deposition (MOCVD) [12], colloidal quantum dots are mainly prepared by inexpensive solution-phase hot injection synthesis. The obtained colloidal quantum dots are formed as monodispersed nanoparticles with organic ligand shell dissolved in a solvent, such as toluene, chloroform, etc. Therefore, solution-based film preparation methods, such as spin coating [13], dip coating [14], drop casting [15], etc., can be used to fabricate colloidal quantum dot films offering significant cost reductions for electronic and optoelectronic device applications.

For colloidal quantum dot material, the surface capping ligands realize the stability of the colloidal solution [16]. However, they also have a critical effect when the individual quantum dots are assembled into a 3-D assembled semiconductor film, which is also called a "quantum dot solid" [17]. The initial long organic hydrocarbon chain, which prevents the quantum dots from aggregation in their solution, are mainly isolating and therefore prohibit carrier transport. Therefore, an additional ligand exchange step is needed to obtain effective carrier transport and enhance film conductivity. Generally this step can be carried out either in solution-phase before the deposition of the quantum dots, or after quantum dot film deposition by a solid-state ligand exchange procedure. Over the past years, different types of surface ligands were explored to enhance film conductivity, including short-chain molecules with single head group [13], cross-linking molecules with two end groups [18], metal chalcogenides [19], etc. In addition to choosing proper surface capping ligands to enhance carrier transport, a homogenous, crack-free quantum dot film is also required. For colloidal quantum dots, several solution-based deposition methods can be used, each with unique advantages and disadvantages. A comparison between different methods is listed in Table 2.1 [20].

Deposition Type	Equipment	Material waste	Film thickness	Uniformity	Layer-by-layer continuous process
Drop casting	None	Little	Monolayer to several micrometers	Very low	No
Spin coating	Spin coater	Significant	Monolayer to hundreds of nanometers	High	No
Dip coating	Dip coater	Little	Monolayer	Moderate	Yes
Langmuir-Blodgett deposition	Langmuir-Blodgett trough	Little	Monolayer to several layers	Extremely high within monolayer	Yes
Doctor blading	Blade	None	Several micrometers	Moderate	Yes

Table 2.1: Comparison of the film-forming techniques for colloidal quantum dots (from [20]).

In this thesis, for the purpose of maximum utilization of the quantum dot material, two deposition methods, drop casting and dip coating were investigated to fabricate a quantum dot film. Drop casting is the simplest method without expensive equipment requirement. The procedure consists of casting a colloidal quantum dot solution on the substrate and drying of the cast film. The

obtained film morphology is mainly determined by the drying step, which relates to the evaporation rate of the solvent at the liquid/vapor interface. In this work different organic solvents were explored in the drop casting procedure, such as hexane, a hexane/heptane mixture, a hexane/octane mixture, toluene, 1,2-dichlorobenzene, etc., and the obtained PbS QD films with different solvents are shown in Figure 2.2a. The best film morphology was obtained by 1,2-dichlorobenzene with heating at 30 ℃ and the corresponding film is shown in Figure 2.2b. However, the film with best surface morphology fabricated by drop casting still exhibit non-uniformity, especially in the edge area. In order to improve the uniformity and considering the comparison between different film forming methods as shown in Table 2.1, dip coating method was proposed as a substitution for drop casting in the followed work to obtain highly uniform films.

Dip coating is a thin film deposition technique where the target substrate is immersed into the quantum dot solution and then pulled up at a controlled speed. During the pulling up process, a quantum dot film is deposited on the substrate while the solvent evaporates. The obtained film thickness is mainly determined by the withdrawal speed and the concentration of the dipping solution. In order to get a homogenous quantum dot film, at least one monolayer should be deposited. Therefore, different withdrawal speeds and quantum dot concentrations were explored, and the morphology of the resulting quantum dot films were checked by atomic force microscopy (AFM) and shown in Figure 2.3. As one can see, regardless of the withdrawal speed, the quantum dot films obtained through 100 nM concentration of QD solution are full of small pin holes and cracks. With 1 μM concentration, continuous quantum dot films with much better surface morphology were obtained. At lower withdrawal speed (20 mm/min), a continuous film with RMS roughness of ~ 3.5 nm was obtained. A better surface roughness of ~ 2 nm was obtained with higher withdrawal speed (80 mm/min), and the corresponding film thickness is ~ 25 nm. Considering the diameter of PbS quantum dots used in this experiment is ~ 9 nm, generally a 3 monolayer quantum dot film can be deposited through a single dip coating step. Since the dip coating approach is compatible with layer-by-layer deposition, a thicker film can be obtained by repeated dip coating.

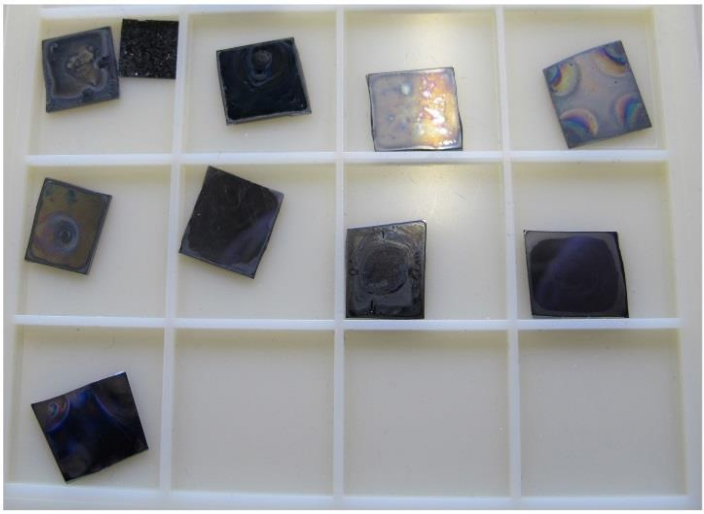

20% Toluene / 80% 1,2-Dichlorobenzene; Heating at 60 ℃	Toluene; heating at 60 ℃	Toluene; Without heating	Heptane; Without heating
Toluene; Heating at 30 ℃	1,2-Dichlorobenzene; Heating at 30 ℃	1,2-Dichlorobenzene; Heating at 60 ℃	1,2-Dichlorobenzene; Heating at 30 ℃
20% Hexane / 80% Octane; Without heating			

(a)

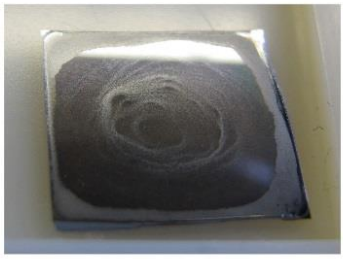

(b)

Figure 2.2: (a) Colloidal PbS quantum dot films prepared by drop casting with different solvent and heating condition. (b) Colloidal PbS quantum film prepared by 1, 2-Dicholrobenzene with heating at 30 ℃.

In addition to obtain a quantum dot film with high uniformity for device application, another issue is exploring different surface capping ligands to improve carrier transport. Normally the ligand exchange procedure is realized by exposing the colloidal quantum dots to a large excess of competitive ligands [21, 22], either in the quantum dot solution or in the solid state film. In this thesis, inorganic short ligands, such as S^{2-} and OH^{-}, were studied to obtain high conductivity quantum dot films. Instead of realizing the ligand exchange procedure in the quantum dot solution, a solid-state ligand exchange procedure was proposed. Compared to a ligand exchange in solution, one significant advantage of solid exchange is that there is no requirement for a stable QD dispersion with short ligands. For S^{2-} ligands, PbS colloidal quantum dot films formed by dip coating were immersed into an excess amount of ligand exchange solution (10 mg/mL of $Na_2S{\cdot}9H_2O$ dissolved in formamide), followed by a thorough cleaning step to remove impurities. Different ligand exchange times were examined to achieve complete ligand exchange. The degree of ligand exchange was probed by Fourier-transform infrared spectroscopy (FTIR) as shown in Figure 2.4a. For oleic acid there exist three absorption peaks in the FTIR spectrum: the peak around 3010 cm^{-1} indicates =C–H stretching; the peak around 2920 cm^{-1} corresponds to CH_2 asymmetric stretching and the peak around 2850 cm^{-1} is due to CH_3 symmetric stretching. The disappearance of these absorption peaks in the FTIR spectrum indicates that more than 30 seconds ligand exchange duration can obtain complete ligand exchange. In order to obtain complete ligand exchange, 1 min S^{2-} ligand exchange duration was chosen in the following study.

In the case of OH^{-} ligand replacement, KOH dissolved in formamide was used as ligand exchange bath. When the concentration of the KOH solution is too high (more than 1 mg/mL), ligand exchange cannot be realized, yet most of the quantum dots are removed from the substrate due to etching of the quantum dot films. Therefore, a proper KOH concentration and corresponding ligand exchange time should be found. Various concentrations and ligand exchange times were explored and the obtained QD films were analyzed by FTIR. The corresponding results are shown in Figure 2.4b. In all cases, most of the organics can be removed from the QD films. In order to minimize the etching effect, 0.01 mg/mL KOH concentration with 10 seconds ligand exchange duration was chosen in the following study. In addition, transmission electron microscopy (TEM) was used to analyze the interparticle distance between two quantum dots and the results are shown in Figure 2.5. One can see that after ligand exchange, the interparticle distance clearly decreased and the particles formed a close packed cluster (Figure 2.5b).

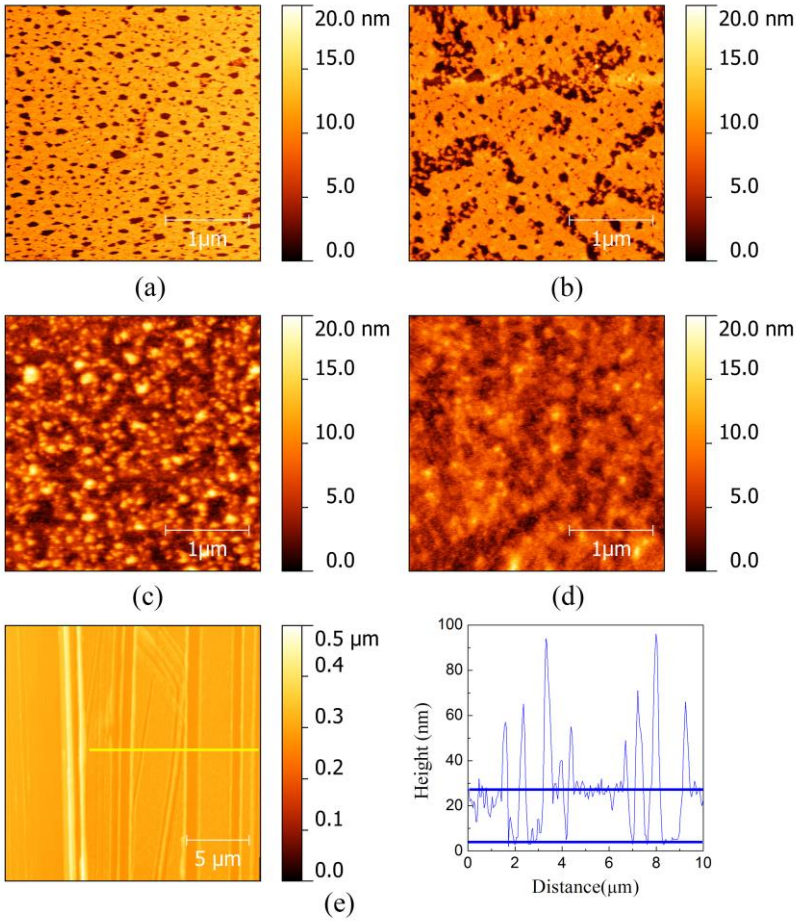

Figure 2.3: AFM images obtained on OlAc-terminated PbS QD films prepared by 1 time dip coating with (a) 20 mm/min withdrawal speed and 100 nM concentration of QD solution; (b) 80 mm/min withdrawal speed and 100 nM concentration of QD solution; (c) 20 mm/min withdrawal speed and 1 μM concentration of QD solution and (d) 80 mm/min withdrawal speed and 1 μM concentration of QD solution. The film thickness is determined by the topographic analysis of a deliberately scratched film for (e) PbS-OlAc films prepared with 80 mm/min withdrawal speed and 1 μM concentration of QD solution. The yellow lines mark the respective cross section shown.

As an excess of $Na_2S{\cdot}9H_2O$ was used during the S^{2-} ligand exchange procedure, the resulting films contain significant impurities and a thorough cleaning is required. TEM images of $Na_2S{\cdot}9H_2O$ treated PbS quantum dots cleaned by a successive immersion in a formamide bath, an acetone bath and an

isopropanol bath are shown in Figure 2.5b. As one can see, impurities still exist, which suggests the sample cleaning is incomplete. FTIR results in Figure 2.6 further reveals that apart from Na_2S, formamide was also present in the non-thorough cleaning case: the peak around 1150 cm^{-1} indicates C−N stretching, which corresponds to the existence of formamide. Hence a complete cleaning process is needed to remove all the impurities which were introduced during the ligand exchange procedure. The optimized cleaning procedure consists of a double immersion in formamide, followed by a double dip in acetone and a final cleaning in isopropanol. The duration for each cleaning step is 1 min. TEM images in Figure 2.5c and d show a clean quantum dot cluster after ligand exchange, which indicates most of the impurities were removed. Moreover, FTIR results in Figure 2.6b imply that the absorption peak from formamide also disappeared, which again confirms that the cleaning procedure is efficient and thorough.

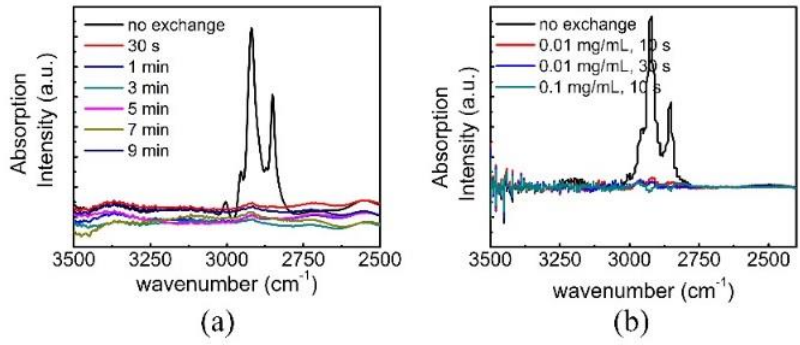

Figure 2.4: (a) Reflection-Fourier transform infrared (FTIR) spectra of OlAc-capped PbS colloidal quantum dot films and S^{2-} capped PbS colloidal quantum dot films treated with different ligand exchange time. (b) Reflection-FTIR spectra of an OlAc-capped PbS colloidal quantum dot film and OH^- capped PbS colloidal quantum dot film treated with different ligand exchange time and concentration.

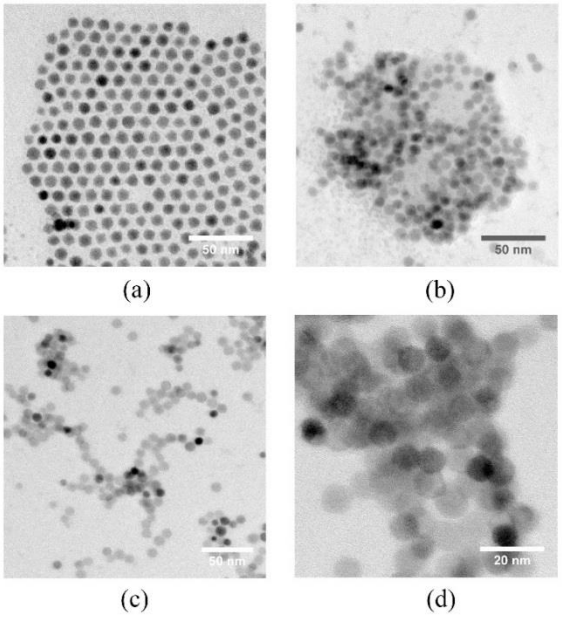

Figure 2.5: TEM images of (a) OlAc-terminated colloidal PbS QDs. PbS QDs after $Na_2S{\cdot}9H_2O$ treatment, followed by (a) 1 time immersion in formamide, 1 time immersion in acetone and 1 time immersion in isopropanol, respectively; (c) and (d) thorough cleaning with 2 time immersion in formamide, 2 time immersion in acetone and 1 time immersion in isopropanol, respectively.

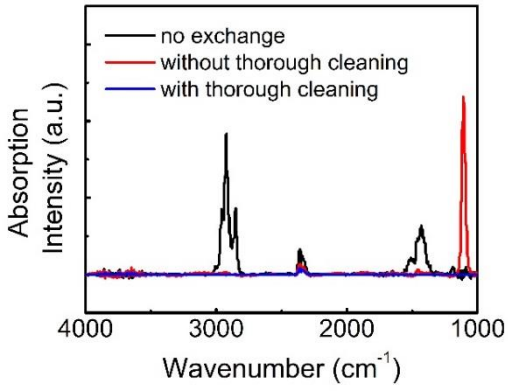

Figure 2.6: Reflection- FTIR spectra of OlAc-terminated PbS colloidal quantum dot film and a S^{2-}-terminated PbS colloidal quantum dot film after $Na_2S{\cdot}9H_2O$ treatment with various cleaning procedures.

Unlike ligand exchange in solution, solid state ligand exchange does not need a stable quantum dot dispersion with short ligands. However, accompanied with the replacement of the organic ligands by short inorganic moieties in solid state, the significant volume loss can lead to cracks and pinholes that will hamper carrier transport in the quantum dot solid. As shown in Figure 2.7a, after direct S^{2-} ligand exchange, the obtained film is full of cracks which are indicated by the yellow circles in the AFM measurement. The corresponding height difference due to the cracks is also observed in the height profile of Figure 2.7a. Therefore, a layer-by-layer method was proposed to overcome this problem, where each cycle involves the deposition of a QD layer by dip coating, and the replacement of the native organic ligands by inorganic moieties (such as S^{2-} and OH^{-}), followed by a thorough cleaning of the resulting film. Through this approach, the cracks are refilled in the next deposition step, and a thorough cleaning followed each ligand exchange cycle to remove excess impurities. Quantum dot films prepared through two times and 6 times layer-by-layer deposition are shown in Figure 2.8. One can see that most of the cracks are refilled, and homogeneous and continuous quantum dot film were obtained through this procedure.

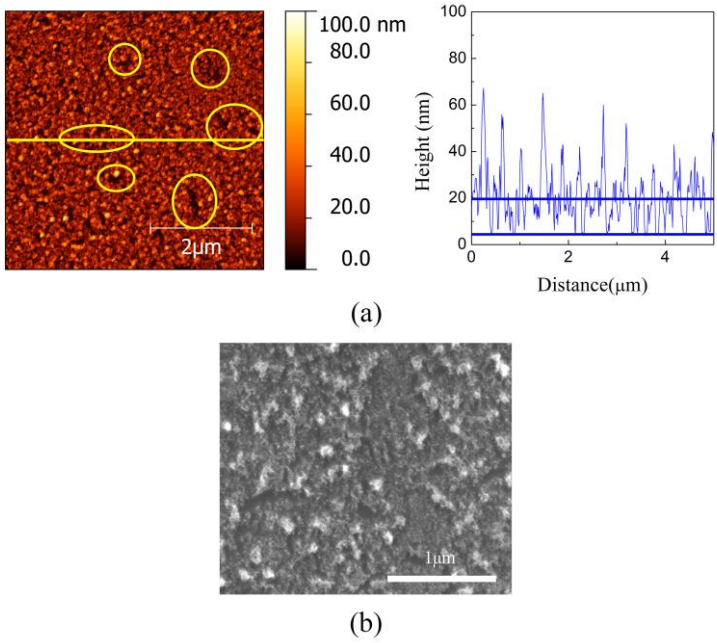

Figure 2.7: (a) AFM image and (b) SEM image of S^{2-}-terminated PbS colloidal quantum dot film prepared by 1 time dip coating with $Na_2S{\cdot}9H_2O$ treatment.

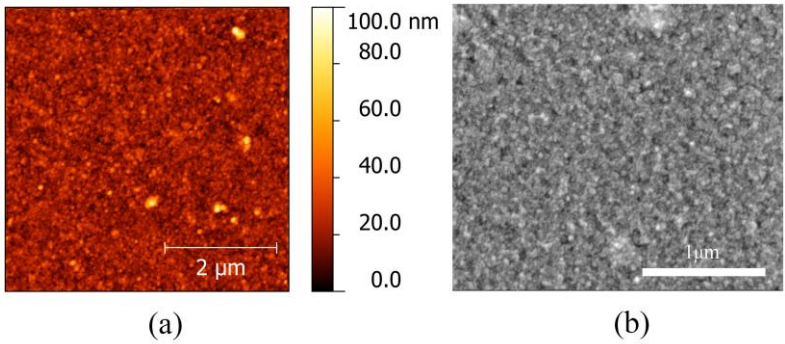

Figure 2.8: (a) AFM image and (b) SEM image of S^{2-}-terminated PbS colloidal quantum dot film prepared by 6 times layer-by-layer dip coating with $Na_2S{\cdot}9H_2O$ treatment.

2.4 Carrier transport mechanism in quantum dot solids

Generally a colloidal quantum dot solid film can be treated as close-packed nanoparticles embedded in a ligand matrix. Therefore, the properties of a quantum dot film should not only take account of the individual quantum dot properties, but also considering the collective properties of a coupled quantum dot array. To understand the carrier transport mechanism in a quantum dot solid film, a lot of efforts have been made [17, 23]. The carrier transport mechanism in colloidal quantum dot solids can be divided into several aspects, which will be briefly discussed in this section.

2.4.1 Exchange coupling energy

Unlike an ordinary semiconductor crystal film obtained by epitaxial growth, there is a significant lattice disorder and interparticle distance variation in colloidal quantum dot solids. This can be attributed to the size and shape distribution of colloidal quantum dots since the individual colloidal quantum dots are faceted instead of perfectly spherical. Moreover, colloidal quantum dot solids are assembled together through Van der Waals force, which strength and direction are very different compared to the covalent or ionic bonds in the ordinary bulk material [17]. The interparticle distance between colloidal quantum dots is mainly determined by the length of the surface capping ligands. In the weak coupling regime, the discrete quantum confined wave functions are localized in individual quantum dots [23, 24]. When the colloidal quantum dots are brought close to each other, their electronic wave function can interact and

delocalized "molecular orbitals" are formed, which is also referred as "coupling". The quantum mechanical coupling between the energy levels can be expressed in terms of a coupling energy $\beta = h\Gamma$, where h is Planck's constant and Γ is the tunneling rate between two orbitals of nanocrystal neighbors [17]. The electronic coupling energy depends strongly on the extension of the orbitals in the nanocrystals, and the width and height of the energy barrier between two nanocrystal neighbors. In the weak coupling regime, where $h\Gamma \ll k_B T$, carriers can only tunnel to neighboring dots; in the strong coupling regime where $h\Gamma \gg k_B T$, the molecular orbitals can extend over many quantum dots [17].

2.4.2 Coulombic charging energy

Coulombic charging energy E_C is the energy cost that has to be paid to put an additional electron on a nanocrystal, which is also referred to as the self-capacitance of individual quantum dots [17, 23-25]. Therefore, the existence of E_C determines the facile migration of an electron from one quantum dot to another. During this process, E_C must be paid twice, i.e. $QD + QD \rightarrow QD^+ + QD^-$ [25]. In a weakly coupled quantum dot solid, Coulombic charging energy creates the Coulomb energy gap, which is also called the Hubbard gap. This will suppress conductivity at low bias, known as the Coulomb blockade effect [23, 25]. When the exchange coupling energy exceeds the Coulombic charging energy, the Coulomb gap disappears and carriers can move freely throughout the quantum dot solid [23, 24].

2.4.3 Disorder in site energy

The size dispersion in colloidal quantum dot material results in a finite dispersion of the orbital energies. The most efficient electron transfer between two quantum dots is obtained when their energies are equal, which corresponds to the condition of resonant tunneling [24]. When the exchange coupling energy is larger than disorder in site energy, sufficiently strong coupling can overcome the dispersion in energy levels of individual quantum dots. As a consequence, an extended wave function can exist [17]. Otherwise the system breaks into small isolated regions where strong coupling prevails, separated by weakly conducting regions.

2.5 Photoconductivity measurement

The fabrication of quantum dot photoconductors consisted of deposition of a SiO_2 isolating layer, electrodes formation and LBL deposition of the colloidal quantum dot film on a silicon substrate. First of all, a SiO_2 film with 500 nm

thickness was deposited through plasma enhanced chemical vapor deposition (PECVD). After that a pair of interdigitated electrodes were fabricated by optical lithography and lift-off process. The electrodes were made by TiAu, in which Ti enhances adhesion to the substrate and Au is used to implement an ohmic contact between the electrodes and the PbS quantum dot film. The spacing between the two electrodes was 2 μm. This is the minimum value obtainable by the optical lithography system. Afterwards, quantum dot films passivated with S^{2-} and OH^- ligands were deposited on the substrates with prefabricated electrodes through LBL deposition.

The current-voltage characteristics of PbS-oleate capped films are shown in Figure 2.9a. As one can see, due to the isolating long organic chain, almost no current flows through the film. The PbS-OlAc QD film is highly insulating ($\sigma \sim 10^{-9}$ S·cm^{-1}). As shown in Figure 2.9b and 2.9c, after ligand exchange, the obtained quantum dot films exhibit photoconductivity. In both cases, efficient carrier transport after ligand exchange was obtained. Under illumination, the resistance of S^{2-} capped PbS QD photodetectors decreases from a dark resistivity of 2.67 kΩ to 1.22 kΩ under 16 mW optical illumination at a wavelength of 1550 nm; the OH^- capped PbS photodetector shows a similar trend from dark resistivity of 7.35 kΩ to 1.57 kΩ under the same illumination. The OH^- capped PbS colloidal QD detectors shows a lower conductivity compared to S^{2-} capped PbS QD detectors, which can be attributed to the more close packing of S^{2-} capped PbS QDs after ligand exchange. For S^{2-} capped PbS QD photodetectors, in darkness the conductivity of the sample is 0.12 S·cm^{-1}, and it increases to 0.26 S·cm^{-1} under illumination with an intensity of 35.2 W/cm^2. In the case of OH^- capped QD photodetectors, the conductivity in darkness is 0.043 S·cm^{-1} and it increases 5 times to 0.20 S·cm^{-1} under same illumination condition. In previous research, various chemical treatments and ligands were used to enhance the conductivity of PbS colloidal QD films. For example, short organic molecules such as diluted 1,2-Ethanedithiol (EDT) was used to treat PbS QD films and the corresponding resistivity is in the range of 10^8 – 10^9 Ω·cm. With a mild annealing a ~ 4 order of magnitude increase in conductivity was reported for PbS QD annealed films [26]. In recent years, short inorganic ligands such as metal chalcogenide complexes (MCCs) were further explored to increase the conductivity. Sergii *et al.* reported a As_2S_3 capped PbS QD film with conductivity in the dark of 2×10^{-6} S cm^{-1} , increasing by 2 orders of magnitude under 20 mW/cm^2 illumination intensity [27]. Compared to these previous research, the S^{2-} and OH^- capped QD film exhibits much higher conductivity, which can be attributed to the high doping level of the QD film.

FTIR-based calibration measurements are used to get the spectral response of the PbS photodetector. An internal tungsten halogen source in the FTIR spectrometer is modulated by a Michelson interferometer and is used to illuminate the photodetector with a set of gold mirrors. The photoconductor is

biased at 0.3 mA current and the resulting voltage drop over the photoconductor is sent back to the FTIR to calculate the spectral dependence of the responsivity (in arbitrary units). The normalized detector responsivity as a function of wavelength for PbS QD photodetectors is presented in Figure 2.10. The two spectral response curves illustrate that the first transition peak of PbS QDs (around 2.0 μm) still exists after ligand exchange, and photodetection up to 2.2 μm can be achieved.

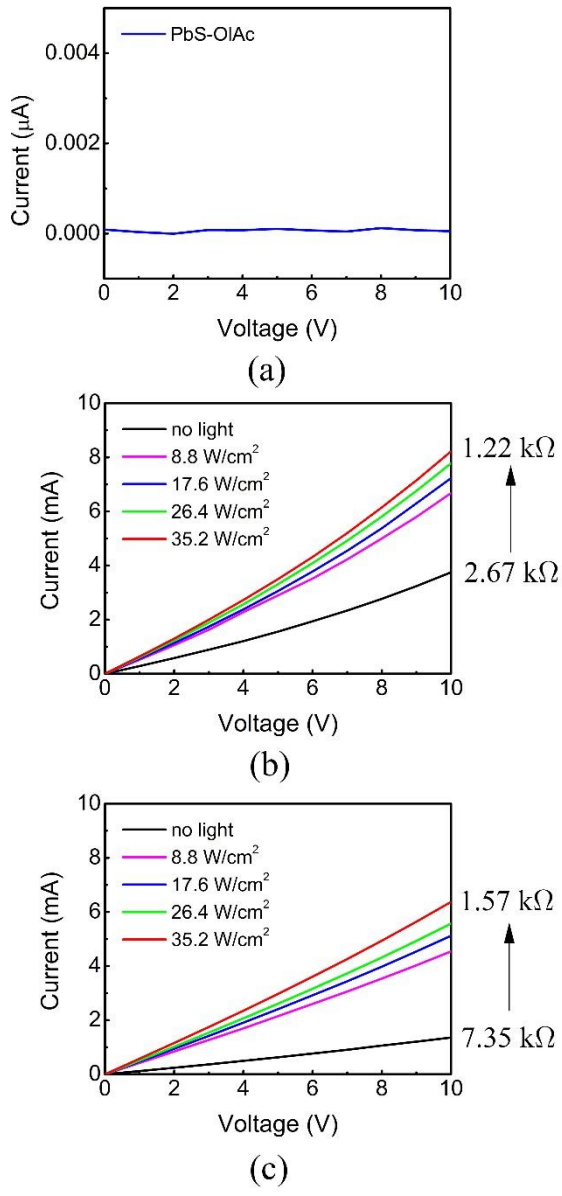

Figure 2.9: Current-voltage characteristics of processed (a) OlAc-terminated PbS (b) S^{2-}-terminated PbS (c) OH^{-}-terminated PbS colloidal quantum dot photoconductive photodetectors.

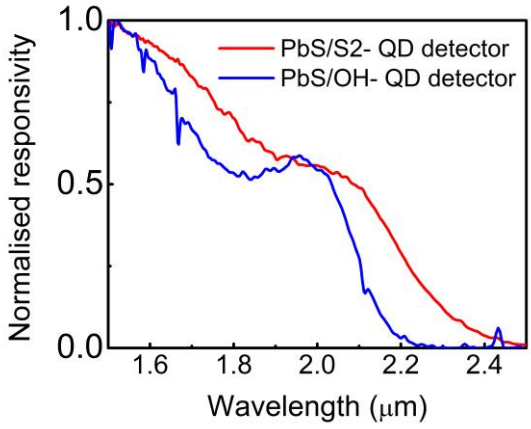

Figure 2.10: Normalized detector responsivity as a function of wavelength for S^{2-} and OH^- capped PbS QD photoconductive photodetectors.

2.6 Conclusion

In this chapter, PbS colloidal QDs as a new optoelectronic material for SWIR photodetector applications was explored. Drop casting and dip coating as quantum dot film preparation methods were explored. Metal-free inorganic ligands, such as S^{2-} and OH^-, are investigated to facilitate the charge carrier transport. A solid state ligand exchange approach with these short inorganic moieties to enhance photoconductivity was optimized. In order to remove film cracks during the ligand exchange procedure, a layer-by-layer approach was developed. Uniform, ultra-smooth colloidal QD films without cracks were obtained through this approach. The first generation photoconductors was obtained with cut-off wavelength up to 2.2 μm. Fabrication of patterned quantum dot films is still an issue. In addition, these quantum dot photodetectors degenerate over time when exposed to air. These issues will be discussed and tackled in the following chapter.

References

[1] S.-F. Tang, S.-Y. Lin, and S.-C. Lee, "Near-room-temperature operation of an InAs/GaAs quantum-dot infrared photodetector," Applied Physics Letters 78, 2428-2430 (2001).

[2] A. D. Stiff, S. Krishna, P. Bhattacharya, and S. W. Kennerly, "Normal-incidence, high-temperature, mid-infrared, InAs-GaAs vertical quantum-dot infrared photodetector," IEEE Journal of Quantum Electronics 37, 1412-1419 (2001).

[3] W. Haowei, L. Zhixiao, F. Chunjie, Y. Dan, Z. Li, Y. Shengyi, and Z. Bingsuo, "Solution-Processed PbSe Colloidal Quantum Dot-Based Near-Infrared Photodetector," Photonics Technology Letters, IEEE 27, 612-615 (2015).

[4] E. Lhuillier, S. Keuleyan, and P. Guyot-Sionnest, "Colloidal quantum dots for mid-IR applications," Infrared Physics & Technology 59, 133-136 (2013).

[5] S. Keuleyan, E. Lhuillier, V. Brajuskovic, and P. Guyot-Sionnest, "Mid-infrared HgTe colloidal quantum dot photodetectors," Nat Photon 5, 489-493 (2011).

[6] I. Moreels, Y. Justo, B. De Geyter, K. Haustraete, J. C. Martins, and Z. Hens, "Size-Tunable, Bright, and Stable PbS Quantum Dots: A Surface Chemistry Study," ACS Nano 5, 2004-2012 (2011).

[7] M. V. Kovalenko, E. Kaufmann, D. Pachinger, J. Roither, M. Huber, J. Stangl, G. Hesser, F. Schäffler, and W. Heiss, "Colloidal HgTe Nanocrystals with Widely Tunable Narrow Band Gap Energies: From Telecommunications to Molecular Vibrations," Journal of the American Chemical Society 128, 3516-3517 (2006).

[8] S. Flamee, R. Dierick, M. Cirillo, D. Van Genechten, T. Aubert, and Z. Hens, "Synthesis of metal selenide colloidal nanocrystals by the hot injection of selenium powder," Dalton Transactions 42, 12654-12661 (2013).

[9] L. Cademartiri, E. Montanari, G. Calestani, A. Migliori, A. Guagliardi, and G. A. Ozin, "Size-Dependent Extinction Coefficients of PbS Quantum Dots," Journal of the American Chemical Society 128, 10337-10346 (2006).

[10] I. Moreels, K. Lambert, D. Smeets, D. De Muynck, T. Nollet, J. C. Martins, F. Vanhaecke, A. Vantomme, C. Delerue, G. Allan, and Z. Hens, "Size-

Dependent Optical Properties of Colloidal PbS Quantum Dots," ACS Nano 3, 3023-3030 (2009).

[11] D. Bimberg, M. Grundmann, N. N. Ledentsov, S. S. Ruvimov, P. Werner, U. Richter, J. Heydenreich, V. M. Ustinov, P. S. Kop'ev, and Z. I. Alferov, "Self-organization processes in MBE-grown quantum dot structures," Thin Solid Films 267, 32-36 (1995).

[12] S. Kim, H. Mohseni, M. Erdtmann, E. Michel, C. Jelen, and M. Razeghi, "Growth and characterization of InGaAs/InGaP quantum dots for midinfrared photoconductive detector," Applied Physics Letters 73, 963-965 (1998).

[13] G. Konstantatos, I. Howard, A. Fischer, S. Hoogland, J. Clifford, E. Klem, L. Levina, and E. H. Sargent, "Ultrasensitive solution-cast quantum dot photodetectors," Nature 442, 180-183 (2006).

[14] J. M. Luther, M. Law, Q. Song, C. L. Perkins, M. C. Beard, and A. J. Nozik, "Structural, Optical, and Electrical Properties of Self-Assembled Films of PbSe Nanocrystals Treated with 1,2-Ethanedithiol," ACS Nano 2, 271-280 (2008).

[15] E. J. D. Klem, H. Shukla, S. Hinds, D. D. MacNeil, L. Levina, and E. H. Sargent, "Impact of dithiol treatment and air annealing on the conductivity, mobility, and hole density in PbS colloidal quantum dot solids," Applied Physics Letters 92, 212105-212103 (2008).

[16] J. A. Dahl, B. L. S. Maddux, and J. E. Hutchison, "Toward Greener Nanosynthesis," Chemical Reviews 107, 2228-2269 (2007).

[17] D. Vanmaekelbergh, and P. Liljeroth, "Electron-conducting quantum dot solids: novel materials based on colloidal semiconductor nanocrystals," Chemical Society Reviews 34, 299-312 (2005).

[18] D. Yu, C. Wang, and P. Guyot-Sionnest, "n-Type Conducting CdSe Nanocrystal Solids," Science 300, 1277-1280 (2003).

[19] M. V. Kovalenko, M. Scheele, and D. V. Talapin, "Colloidal Nanocrystals with Molecular Metal Chalcogenide Surface Ligands," Science 324, 1417-1420 (2009).

[20] J. Yang, M. K. Choi, D.-H. Kim, and T. Hyeon, "Designed Assembly and Integration of Colloidal Nanocrystals for Device Applications," Advanced Materials 28, 1176-1207 (2016).

[21] M. Kuno, J. K. Lee, B. O. Dabbousi, F. V. Mikulec, and M. G. Bawendi, "The band edge luminescence of surface modified CdSe nanocrystallites:

Probing the luminescing state," The Journal of Chemical Physics 106, 9869-9882 (1997).

[22] C. B. Murray, C. R. Kagan, and M. G. Bawendi, "Synthesis and characterization of monodisperse nanocrystals and close-packed nanocrystal assemblies," Annual Review of Materials Science 30, 545-610 (2000

[23] F. Remacle, and R. D. Levine, "Quantum Dots as Chemical Building Blocks: Elementary Theoretical Considerations," ChemPhysChem 2, 20-36 (2001).

[24] D. V. Talapin, J.-S. Lee, M. V. Kovalenko, and E. V. Shevchenko, "Prospects of colloidal nanocrystals for electronic and optoelectronic applications," Chemical reviews 110, 389-458 (2009).

[25] I. S. Beloborodov, A. V. Lopatin, V. M. Vinokur, and K. B. Efetov, "Granular electronic systems," Reviews of Modern Physics 79, 469-518 (2007).

[26] Seung Jae Baik, Kyungnam Kim, Koeng Su Lim, SoMyung Jung, Yun-Chang Park, Dong Geon Han, Sooyeon Lim, Seunghyup Yoo, and Sohee Jeong, The Journal of Physical Chemistry C 115 (3), 607 (2010).

[27] Sergii Yakunin, Dmitry N. Dirin, Loredana Protesescu, Mykhailo Sytnyk, Sajjad Tollabimazraehno, Markus Humer, Florian Hackl, Thomas Fromherz, Maryna I. Bodnarchuk, Maksym V. Kovalenko, and Wolfgang Heiss, ACS Nano 8 (12), 12883 (2014).

3

The micropatterning of layers of quantum dots with inorganic ligands using selective wet etching

3.1. Introduction to patterning of QDs

Colloidal quantum dots (QDs) are new optoelectronic materials that raise a great interest in the photonics community. Various applications, such as solar cells [1-3], photodetectors [4-6] and light emitting diodes (LEDs) [7, 8] have been demonstrated by using different semiconductor QD materials. The hot injection chemical synthesis allows for a low-cost, precise and versatile production [9, 10]. In addition, by varying their size, the QD electrical and optical properties (absorption cut-off wavelength, luminescence wavelength) can be easily tuned through the quantum size effect [11]. Furthermore, the fact that these QDs are available in solution allows for large-area heterogeneous integration on substrates by solution-based processes, such as spin casting [12], inkjet printing [13, 14, 15], evaporation-controlled self-assembly [16], and Langmuir–Blodgett

(LB) [17] or Langmuir–Schaeffer deposition [18, 19]. This offers a considerable cost reduction as compared to thermally evaporated or epitaxially grown layer stacks.

As a new optoelectronic material, one of the applications of colloidal QDs that stands out is the use of QD films as a medium for light absorption and charge carrier transport in photovoltaic energy conversion [20, 21], photodetection [22, 23] and electronics [24, 25]. For example, colloidal quantum dots solar cells with a certified efficiency up to 7% were recently reported [26], while a hybrid phototransistor consisting of a combination of colloidal quantum dots with graphene was shown to achieve an ultrahigh gain of up to 10^8 electrons per photon [27]. A crucial step for these applications is the replacement of the long, electrically insulating organic ligands that cap as-synthesized QDs by much shorter moieties to enhance the mobility of charge carriers in QD films. While initial procedures involved the exchange of the original ligands for short, bifunctional organic molecules such as hydrazine or dietheylamine, more recent approaches make use of the replacement of long organic ligands by short, inorganic species such as $Sn_2S_6^-$ or Cl^-. Very often, layers of QDs with short ligands are formed using a layer-by-layer deposition approach, involving the repeated deposition of a layer of QDs stabilized by their long, as-synthesized ligands, followed each time by a ligand exchange step [28, 29, 30]. Importantly, this approach does not require a stable dispersion of QDs with short ligands and it enables cracks formed in the layer due to the ligand exchange to be filled in the next deposition step. High electron mobility exceeding 15 $cm^2/(V{\cdot}s)$ was reported recently for III-V nanocrystals capped with molecular metal chalcogenide ligands by Liu et al [31].

Especially in the case of photodetectors or transistors, the suitability of colloidal QDs for solution based processing offers the perspective to combine QD based devices with integrated electronic or photonic circuits. This however requires the formation of well-defined and aligned patterns of colloidal QD layers. In the literature, different micropatterning processes have been explored, each having their own specific benefits and disadvantages. Lambert et al. proposed to use Langmuir-Blodgett layer deposition on a silicon substrate that is covered by a patterned resist, which results in a monolayer pattern with micrometer resolution after lift-off [32]. High-resolution nanoscale patterning of QD films was also demonstrated through electron beam lithography (EBL) [33, 34]. Nevertheless, the long writing time and high cost of the electron beam lithography makes it less attractive for mass production. A high-throughput micropatterning method with sub-micrometer scale resolution was realized by a contact printing process [35, 36]. With a key-lock system, a nanoscale patterned QD film can be implemented by e-beam lithography and highly discriminatory binding in a DNA-mediated approach [37, 38]. However, the deposition on a three-dimensional surface such as a photonic or electronic integrated circuit and

the formation of micropatterned multiple layer QD films still remains challenging. Moreover, none of these approaches can be directly applied for the patterning of QD films with inorganic ligands that are typically used as absorber layer in photovoltaic cells and photodetectors or as conductive channel in field effect transistors.

In this chapter, we use PbS colloidal QDs to demonstrate a novel technique to pattern films of QDs stabilized by inorganic ligands. The PbS QD films are defined using a layer-by-layer approach where each cycle involves the deposition of a QD layer by dip coating, the replacement of the native organic ligands by metal-free inorganic ligands, such as OH^- and S^{2-} [39], followed by a thorough cleaning of the resulting film. This results in smooth and crack-free QD films. The micropatterns are defined by a positive photoresist, followed by the removal of uncovered QDs by wet etching using an HCl/H_3PO_4 mixture. The resulting patterns can have feature dimensions down to 500 nm, limited by the resolution of the lithographic process and it is shown that the process applies to 3D substrates as well. To further evaluate the influence of this patterning technique on the properties of the colloidal QDs, films of highly luminescent CdSe/CdS core/shell are treated and micropatterned with the same technique. Photoluminescence analysis demonstrates that more than 90% of the quantum yield remains after photolithography and wet etching. This indicates that the proposed approach allows for the effective micropatterning of QD films without affecting the QD properties.

3.2. Experimental details

3.2.1. Synthesis of colloidal quantum dots

OlAm-teminated PbS QDs used in this study were the same as the one used in Chapter 2.

The CdSe/CdS core/shell QD synthesis was accomplished by adapting the CdSe/CdS dot-in-rod synthesis procedure developed by Carbone et al [40]. CdO (0.25 g), TOPO (3 g) and OlAc (2.35 g) were added to a three-neck flask, the resulting mixture was flushed with nitrogen and heated at 120 ℃ for 1 hour. The temperature was then increased to 330 ℃ and 1.8 mL of TOP was injected when the mixture solution became colorless. After the temperature recovered to 330 ℃, a mixture of CdSe core QDs (86 mmol) and sulfur (0.12 g) in 1.8 mL of TOP was injected in the flask. The reaction was quenched after 3 min by a sudden drop of the temperature using a water bath, followed by the injection of 10 mL of toluene. Then the QDs were precipitated with isopropanol and MeOH and centrifuged. After the supernatant was decanted, the QDs were resuspended

in toluene. The precipitation and resuspension were repeated three more times and the CdSe/CdS core/shell QDs were finally resuspended in toluene.

3.2.2. Fabrication of QD films

In this study, QD films were prepared with a layer-by-layer approach. The corresponding process flow is shown in Figure 3.1. Each cycle involves the deposition of a QD layer by dip coating, the replacement of the native organic ligands by metal-free inorganic ligands, followed by a thorough cleaning of the resulting film. The dipping procedure with ligand exchange can be done repeatedly to implement a multi-layer film. Here, PbS QD thin films were formed on Si substrates. CdSe/CdS QD films were formed on cover glass substrates. A layer-by-layer approach was used by dipping the substrate into a PbS or CdSe/CdS QD dispersion in toluene with a QD concentration in the range of 0.75 to 1 μM and pulling it out at a speed of 10 mm min^{-1}. Before layer-by-layer deposition of the QD films, the Si substrates were treated with HF solution (~10%) for 1 min to remove the native oxide and enhance the hydrophobicity of the surface. After complete drying, the QD film was re-immersed into a solution of either $Na_2S{\cdot}9H_2O$ (10 mg mL^{-1}) or KOH (0.01 mg mL^{-1}) in formamide to exchange the OlAc ligands by S^{2-} and OH^- moieties, respectively. After the desired ligand exchange time (typically 60 s for S^{2-} and 10 s for OH^-), the sample was washed by immersing it twice in formamide and twice in acetone, followed by a final dip in isopropanol to remove residual impurities induced by ligand exchange. Afterwards, the sample was dried under nitrogen. The time needed for one cycle of layer-by-layer deposition is ~ 10 min, therefore, in order to obtain a QD film with sufficient layer thickness through multiple times of layer-by-layer deposition is quite time consuming. Depending on the experiment, the QD films used in this chapter were prepared by repeating the layer-by-layer deposition four to six times. The resulting PbS QD films exhibit a remarkable improvement of photoconductivity compared with OlAc-terminated PbS colloidal QD films as reported in [41], which illustrates that this novel technique is promising for integrated photodetector and photovoltaic applications.

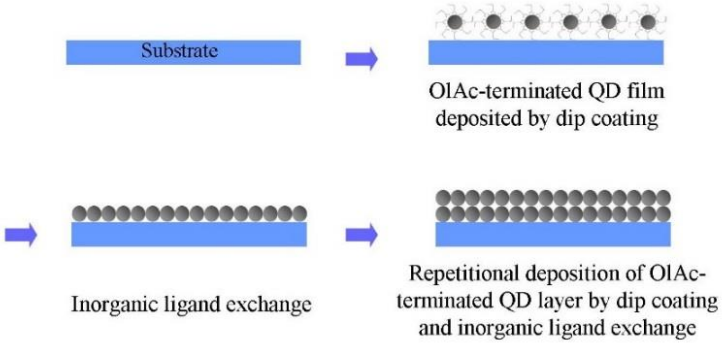

Figure 3.1: Illustration of the layer-by-layer deposition of the QD film.

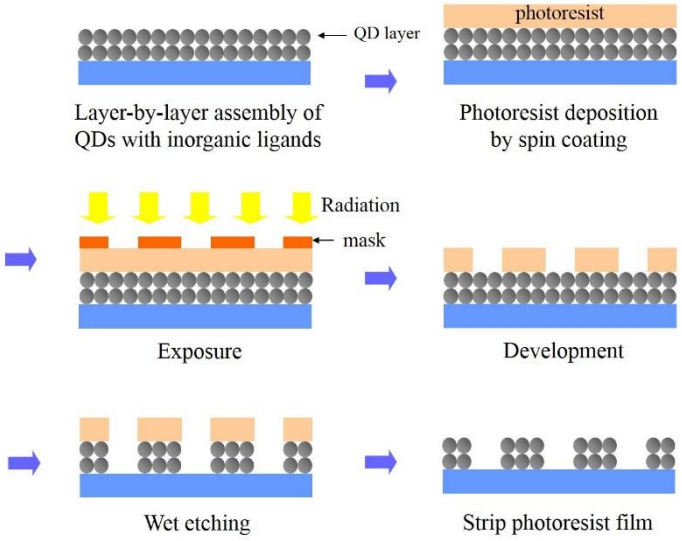

Figure 3.2: Process flow of the QD film micropatterning.

3.2.3. Photolithography and wet etching

The process flow of the patterning of a QD film formed by the layer-by-layer approach is shown in Figure 3.2. In the first step, an AZ® 5214E image reversal resist was spun on top of the QD film by spin coating, and then the sample was prebaked for 3 mins at 100 ℃ to form a robust photoresist layer. Following light exposure and development using a SUSS MA6 mask aligner, a pattern was transferred from a mask to the photoresist layer. Afterwards, an HCl/H_3PO_4

mixture, prepared by mixing 37% HCl and 85% H_3PO_4 solutions, was used as etchant to remove the uncovered parts of the QD film. The volume ratio between the HCl and H_3PO_4 solution in the etchant was ≈1:10. The QD film, covered with patterned photoresist, was immersed into the HCl/H_3PO_4 mixed etchant for the desired etching time to remove the uncovered QDs. The etching of the QDs is attributed to the formation of $Pb_3(PO_4)_2$, $PbCl_2$ and H_2S. In the end, the remaining photoresist layer was stripped from the QD film using acetone, and the sample was cleaned with isopropanol to obtain a micropatterned QD film.

3.2.4. Characterization of quantum dot films

The absorbance of the colloidal solutions and thin films was evaluated by UV-vis-NIR spectroscopy (Perkin Elmer Lambda 950). Ligand exchange was analyzed at the level of individual QDs by transmission electron microscopy (TEM, Jeol, FE2200). Samples for TEM were prepared by transferring the QD film to a copper grid with carbon film through dipping. For the ligand exchange sample, the TEM grid with QDs on top was dipped into the ligand exchange solution, followed by a thorough cleaning to get rid of impurities. A Fourier transform infrared spectrometer (FTIR spectrometer, Nicolet 6700) was used to analyze residual organic species in the QD film. The overall morphology of the films was analyzed by means of atomic force microscopy (AFM) measurements (Picoplus, Molecular Imaging) and scanning electron microscopy (SEM, FEI Nova 600 Nanolab Dual-Beam FIB). The film thickness was also derived from AFM by measuring the average height profile of a scratch over the entire substrate surface. Photoluminescence measurements were made using an Edinburgh Instruments FLSP920 UV-vis-NIR spectrofluorimeter, using a 450 W xenon lamp as the steady state excitation source and a Hamamatsu R928P PMT detector, which has a response curve between 200 and 900 nm. All measurements were performed for an excitation wavelength of 365 nm and were corrected for the sensitivity of the detector. The quantum yield (QY) of the QDs dispersed in toluene was determined for an excitation wavelength of 365 nm and by comparison with coumarin 2, which has a known PLQY of 92% in ethanol [42]. The QY of the QD films was measured using an integrating sphere. Fluorescence microscopy (Nikon Eclipse Ti inverted microscope) was used to get the photoluminescence mapping of the micro-patterned film.

3.3. Results and discussion

3.3.1. Layer-by-layer assembly of quantum dots with inorganic ligands

In this study, colloidal PbS QDs with a band gap at 2.2 μm are used, which corresponds to a diameter of 9.4 nm according to the PbS sizing curve. The corresponding absorbance spectrum of these PbS QDs in tetrachloroethylene (C_2Cl_4) is presented in Figure 3.3. In order to explore the ligand exchange upon exposure to $Na_2S{\cdot}9H_2O$ or KOH solutions, a reflection-FTIR spectrometer was used to analyze organic residues in the QD film. Figure 3.4a shows the reflection-FTIR spectra of a film of OlAc-terminated PbS QDs and of the corresponding QD film after exposure to $Na_2S{\cdot}9H_2O$. The characteristic peaks corresponding to C=C stretching around 3010 cm^{-1}, $–CH_2$ asymmetric stretching around 2920 cm^{-1} and $–CH_3$ symmetric stretching around 2850 cm^{-1} are almost completely eliminated after ligand exchange, which indicates that most of the OlAc ligands were removed from the QD film. Similar results can be seen in figure 3.4b, which shows spectra obtained before and after a KOH treatment. The ligand exchange on a small scale is examined by TEM. The micrographs clearly show that the distance between the PbS QDs—originally dictated by the long chain oleate ligands (Figure 3.5(a))—decreases after $Na_2S{\cdot}9H_2O$ (Figure 3.5(b)) or KOH (Figure 3.5(c)) treatments, which is promising to form a close-packed QD film for device applications. Moreover, it appears that the S^{2-} terminated QDs tend to aggregate, opposite from the OH^- terminated QDs. We found that if the QD film was too thick before ligand exchange, i.e., when multiple layers were deposited after dip coating, the top few layers of QDs detach from the film during the ligand exchange. Due to the material loss in the ligand exchange procedure, generally a ~1 monolayer QD film with cracks can be obtained in one cycle of dip coating/ligand exchange. The corresponding film cracks can be refilled in the followed deposition step, however, the introduction of film cracks in each ligand exchange cycle causes the evolution of the total layer thickness to be less than expected. Nevertheless, this can be compensated for by multiple depositions through the layer-by-layer approach.

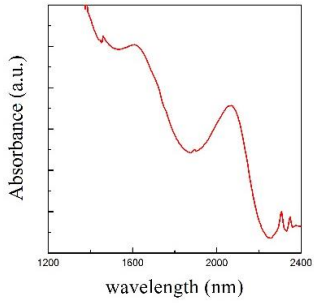

Figure 3.3: Absorbance spectrum of the PbS QDs used (solvent: tetrachloroethylene).

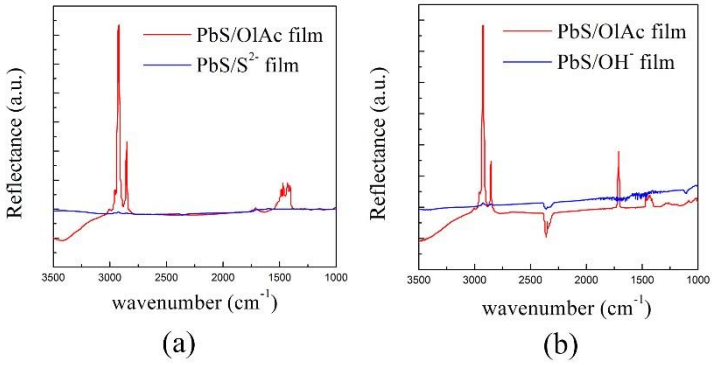

Figure 3.4: (a) Reflection-Fourier Transform Infrared (FTIR) spectra of OlAc-terminated PbS colloidal QD film and S^{2-}-terminated PbS colloidal QD film after $Na_2S{\cdot}9H_2O$ treatment. (b) Reflection-FTIR spectra of OlAc-terminated PbS colloidal QD film and OH^--terminated PbS colloidal QD film after KOH treatment.

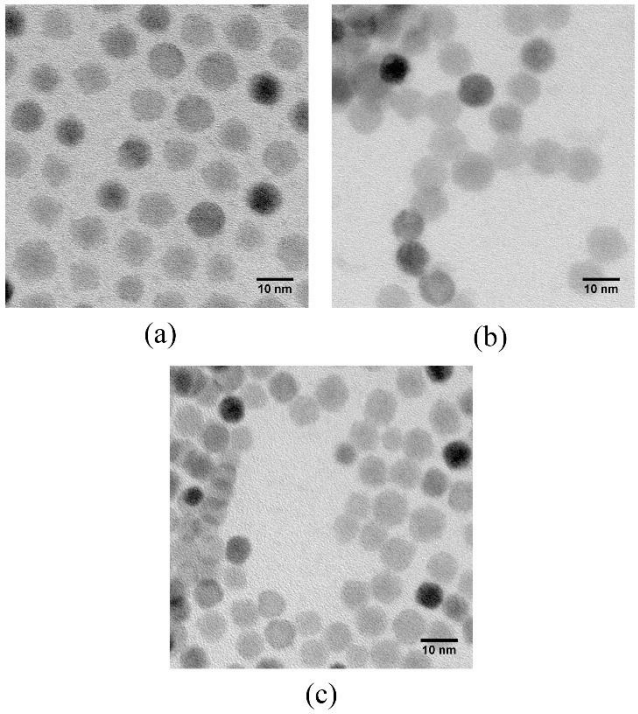

Figure 3.5: TEM images of (a) OlAc, (b) S^{2-} and (c) OH^- -terminated colloidal PbS QDs.

Figure 3.6 (a) and (b) show AFM images of QD films made using six deposition cycles of PbS/S^{2-} and PbS/OH^- QDs, each involving dipping the substrate into a 0.75 μM PbS QD suspension in toluene and pulling it out at a speed of 80 mm min^{-1}. Corresponding SEM images are shown in Figure 3.7. The surface morphology of S^{2-} and OH^- terminated QD films measured by SEM on different scales confirms that a homogeneous and crack-free film can be realized with this method. The RMS roughness as determined from the AFM image amounts to 5.5 nm and 6 nm for PbS/S^{2-} and PbS/OH^- QD films, respectively, a number smaller than the diameter of a single nanocrystal. Before photolithography and micropatterning, a layer thickness of ≈75 nm and ≈65 nm is found for S^{2-} and OH^- terminated QD films (see Figure 3.8), respectively, indicating that about one QD monolayer is deposited in each cycle. We thus conclude that the process developed results in smooth and homogeneous films that are well-suited for testing the subsequent process steps.

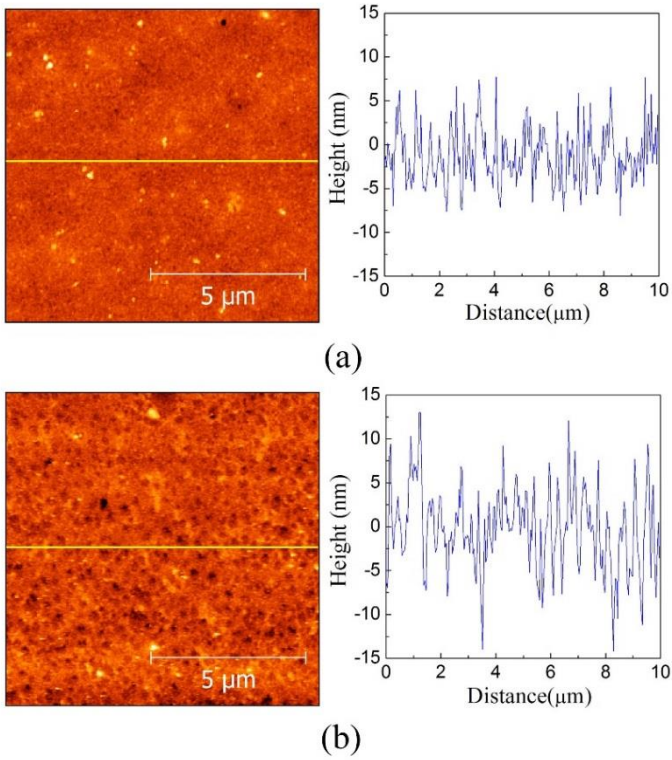

Figure 3.6: AFM images obtained on (a) PbS/S^{2-} and (b) PbS/OH^- QD films prepared by 6 times layer-by-layer deposition before lithography and micropatterning.

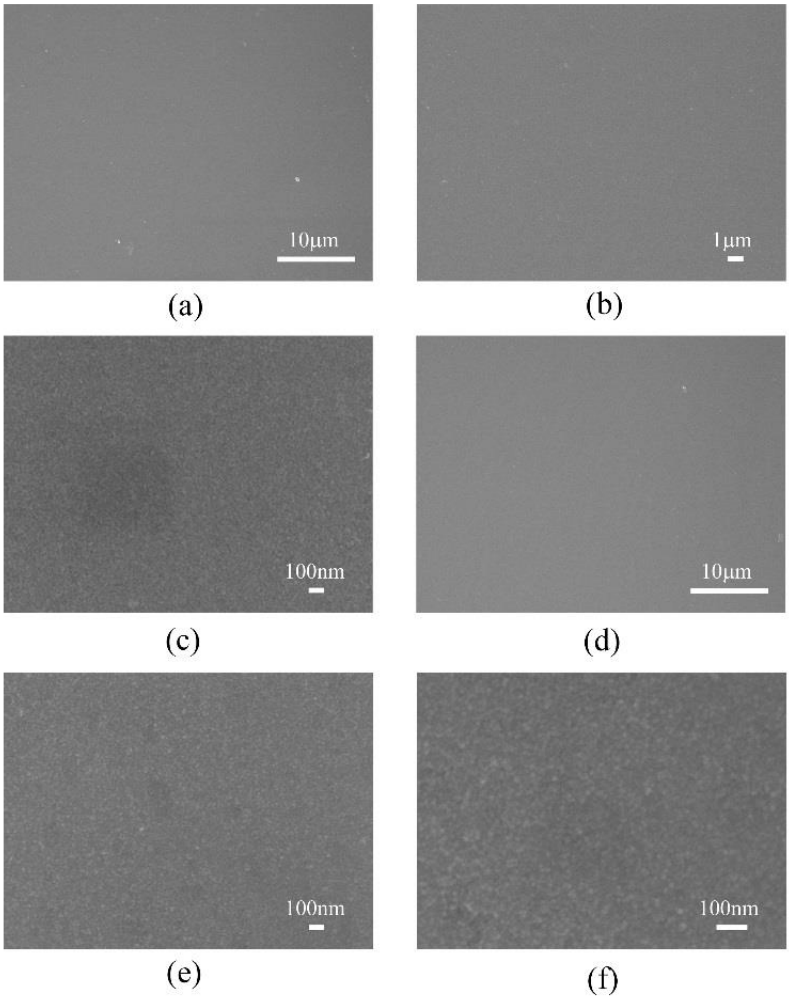

Figure 3.7: SEM images of (a, b and c) S^{2-} and (d, e and f) OH^{-}-terminated PbS QD films at different magnifications. The films were prepared by 6 times layer-by-layer deposition.

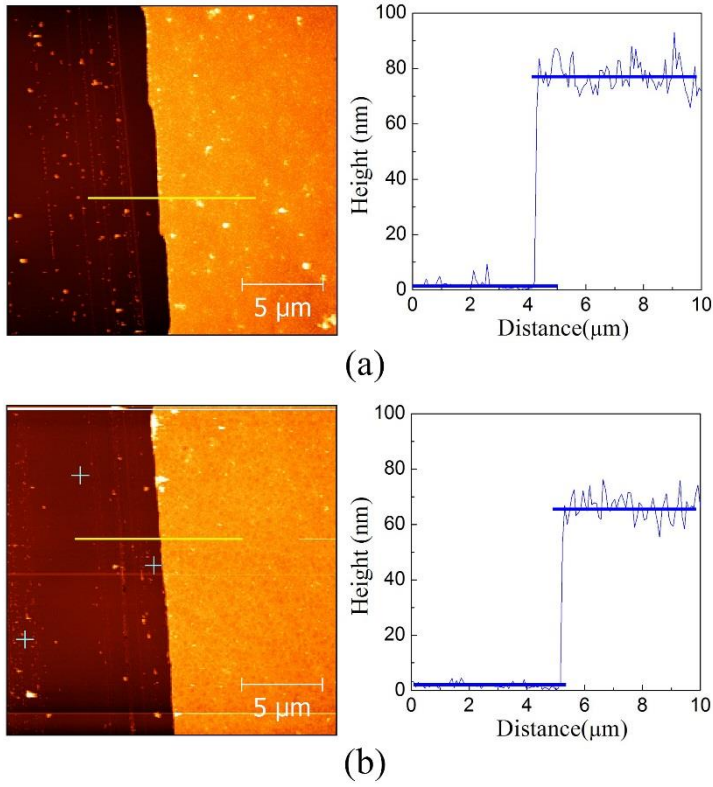

Figure 3.8: Film thickness is determined by the topographic analysis of a deliberately scratched film, both for (c) PbS/S^{2-} and (d) PbS/OH^{-} films. The yellow lines mark the respective cross sections shown.

3.3.2 Micro-patterned QD films—2D substrates

To put the proposed micropatterning scheme into practice, a first set of films of PbS QD films was formed by layer-by-layer deposition using four deposition cycles, each involving dipping the substrate into a 1 μM PbS QD suspension in toluene and pulling it out at a speed of 80 mm min^{-1}. To optimize the etching step, etching solutions with different HCl/H_3PO_4 ratios were investigated and the etching time was varied. Figure 3.9(a) and (b) show SEM images of the micro-patterned PbS/S^{2-} QD films with photoresist on top after a 30 s wet etch using HCl and H_3PO_4 mixing ratios of 1:8 and 1:10, respectively. The gap under the photoresist visible when the higher HCl ratio is used (figure 3.9a) indicates that under-etching occurs under these conditions, which is prevented by lowering the HCl concentration (figure 3.9b). Possibly, this is due to the lower viscosity and

the concomitantly higher etching speed of etching solutions with a higher HCl content. SEM images of the micro-patterned PbS/S^{2-} QD films after stripping of the photoresist for different etching times are displayed in figure 3.9 (c) and (d). One can see that after ≈30 s of wet etching (figure 3.9(c)), the uncovered QD film was almost fully removed from the substrate and a well-defined patterned QD film was obtained. As shown in figure 3.9(d), increasing the etching time to ≈60 s only promotes under-etching, resulting in the disappearance of the outermost parts of the QD film covered by the photoresist over a depth of 410-420 nm. As a result, we kept the HCl:H_3PO_4 volume ratio for further studies fixed at 1:10 and limited the etching time—depending on the layer thickness—to the lowest time needed to remove all uncovered QDs. The etching rate for PbS/S^{2-} and PbS/OH^- films is ~ 40 nm/min and 45 nm/min, respectively.

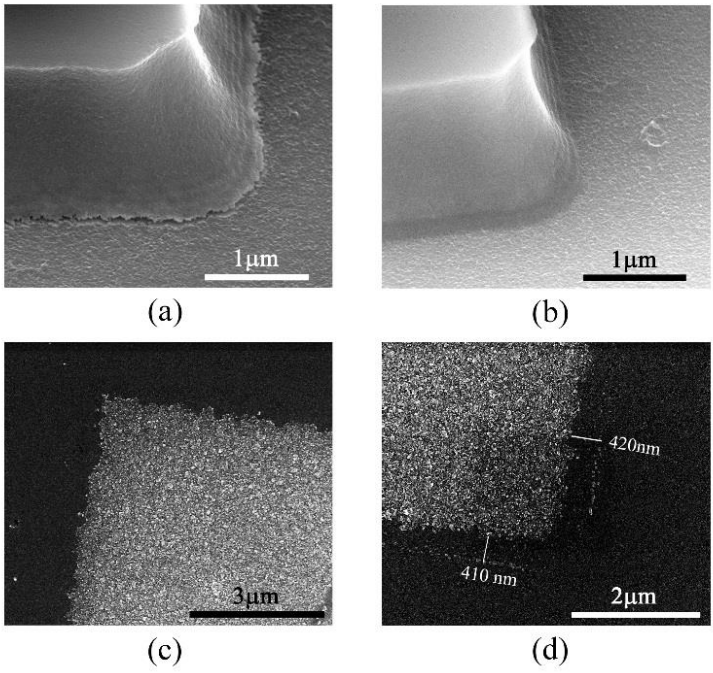

Figure 3.9: SEM images of 30 seconds etching of a micro-patterned S^{2-} terminated PbS QD film with photoresist formed by etching with a mixture of (a) 1HCl:8H_3PO_4 or (b) 1HCl:10H_3PO_4. SEM images of (c) 30 seconds and (d) 60 seconds etching with 1HCl:10H_3PO_4 of S^{2-} terminated PbS QD film.

Figure 3.10 shows SEM images at different magnifications of the micropatterned OH^- terminated PbS QD films formed with the optimized process (etching solution: 1:10 HCl:H_3PO_4; etching time: 100 s and 150 s for

PbS/OH^- and PbS/S^{2-}, respectively). For comparison with untreated films, they were again formed using six layer-by-layer deposition cycles in total, dipping the substrate into a 0.75 μM PbS QD suspension in toluene and pulling it out at a speed of 80 mm min^{-1}. As shown in figure, after stripping the photoresist film, a well-defined QD film is obtained. The resolution of the micropatterning is mainly limited by the optical lithography process, which is ≈0.5 μm. As show in figure 3.11, similar results are obtained using S^{2-} terminated PbS QD films. An AFM analysis of similar micropatterned films yields an RMS roughness of ≈5.5 nm and ≈4.5 nm for S^{2-} and OH^- terminated PbS QD films, respectively (see figure 3.12 (a) and (b)). Moreover, the layer thickness—in this case simply measured by imaging the transition between the uncovered substrate and the remaining PbS film—for both films amounts to ≈70 nm and ≈50 nm (figure 3.13 (a) and (b)). Hence, only in the case of PbS/OH^-, a somewhat thinner layer is obtained compared to the un-patterned QD films (~ 65 nm). Therefore, we conclude that the proposed micropatterning process leads to well-defined patterns of PbS QD films with a resolution determined by that of the lithography process used and without affecting the original morphology of the films.

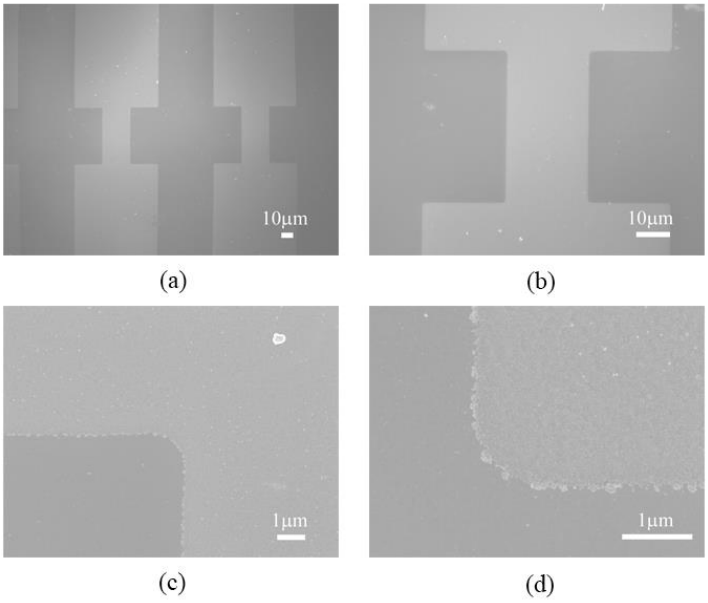

Figure 3.10: SEM images of 1 min 40 seconds etching of a micro-patterned OH^- terminated PbS QD film by etching with a mixture of 1HCl:10H_3PO_4 on different magnification scales.

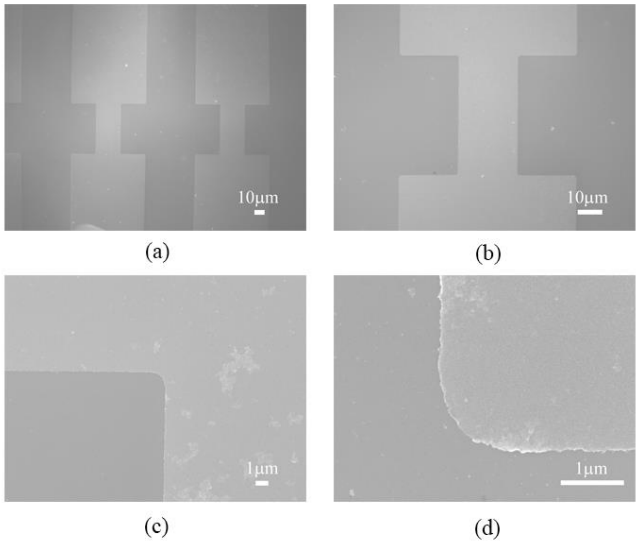

Figure 3.11: SEM images of 2 min 30 seconds etching of a micro-patterned S^{2-} terminated PbS QD film formed by etching with a mixture of 1HCl:10H_3PO_4 on different magnification scales.

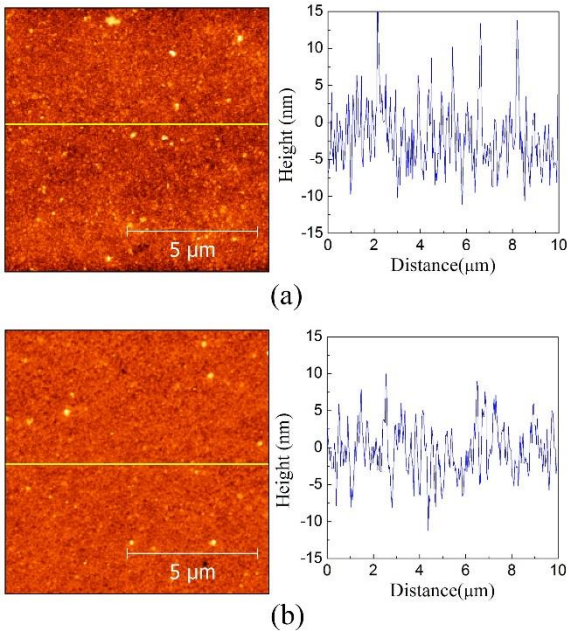

Figure 3.12: AFM images obtained on (a) PbS/S^{2-} and (b) PbS/OH^- QD films after micropatterning.

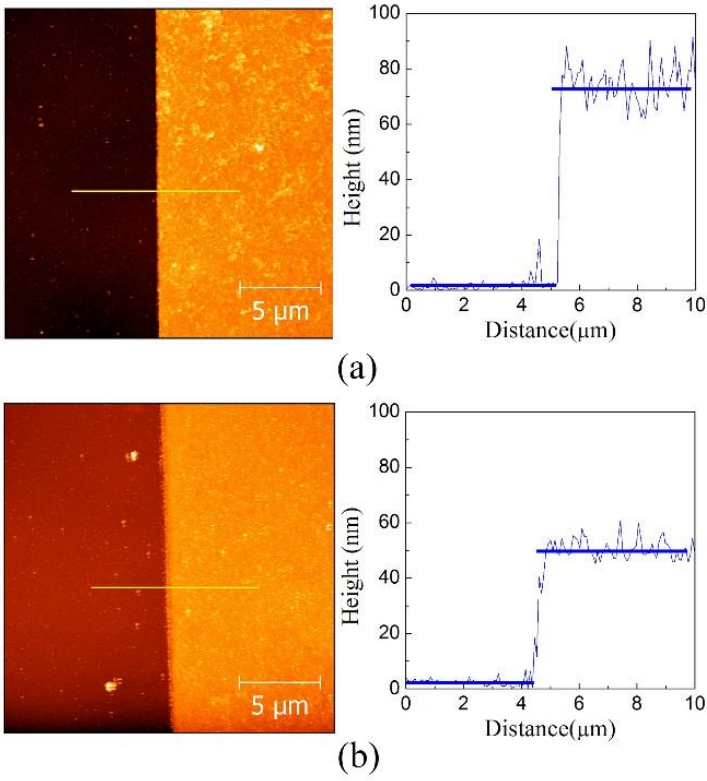

Figure 3.13: The layer thickness is determined by imaging the edge of the QD film, both for (c) PbS/S^{2-} (d) and PbS/OH^{-} (d) QD films. The films were prepared by 6 times layer-by-layer deposition. The yellow lines mark the respective cross sections shown.

3.3.3 Micro-patterned QD films—3D substrates

So far, the micropatterning method has been used for pattern formation on flat, 2D substrates. However, to form patterned QD films on more complex integrated circuits that contain, e.g., air cladding silicon waveguides or metal electrodes, pattern formation should be extended to substrates with 3D topography. To evaluate the potential of the introduced method for 3D topography micropatterning, we used it on silicon substrates with 3D topography.

To fabricate such substrates, a photoresist was spun on top of a silicon substrate by spin coating and was prebaked to form a robust photoresist layer. After exposure and development, a patterned photoresist layer was formed on

top of the silicon substrate. Then reactive-ion etching (RIE) was used to make a 3D structure about 220 nm in height. Afterwards, the photoresist was removed by acetone. The corresponding SEM images of 3D silicon substrates are shown in figure 3.14(a) and (b). Before the layer-by-layer deposition of the QD film, the 3D substrates were treated with an HF solution (~10%) to enhance the hydrophobicity of the surface and obtain a good wetting of the substrate during the dip-coating. As shown in figure 3.15, films prepared on Si substrates with a native oxide show clear dewetting in the case of 3D substrates. The QD films were prepared using six layer-by-layer deposition cycles, and the same wet etching approach was used to pattern the QD films. An HCl/H_3PO_4 mixture in a 1:10 ratio was used for etching, and the same etching times as for the 2D micropatterned QD films were used (see figure 3.10 and 3.11). Under the same etching condition, a considerable amount of PbS QDs were left on the surface, especially at the edges of the trenches. This indicates an inhomogeneous coverage with little QDs deposited in the middle of the trench and an accumulation of dots at the edges. The SEM images of micropatterned, S^{2-} and OH^- terminated PbS QD films on HF treated 3D silicon substrates are shown in figure 3.16 and 3.17, respectively. The images show that well-defined micropatterned PbS QD films were realized on top of the 3D silicon substrates. Unlike OH^- terminated QD films, S^{2-} terminated PbS QD films on 3D substrates sometimes show some cracks along the sharp edge. This is attributed to the difference in the silicon etch rather than the exact quantum dot termination used. When coating silicon waveguides with similar topography with OH- and S-terminated PbS quantum dot films, no cracks were observed in either case.

We conclude that the layer-by-layer deposition and selective wet etching approach can be used to form micropatterned QD films on both 2D and 3D substrates. Clearly, this makes the method highly suitable for the local deposition of films of QDs with inorganic ligands, to be used as active materials in integrated electronic or photonic devices.

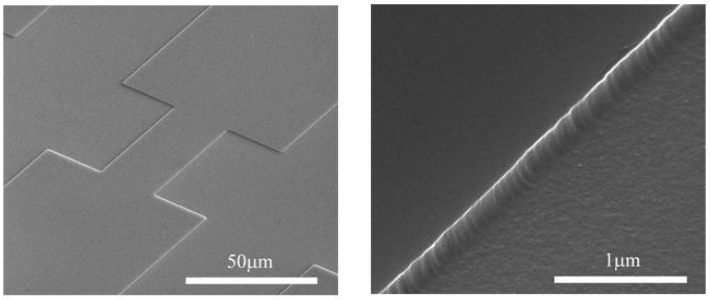

Figure 3.14: SEM images of 3D silicon substrates.

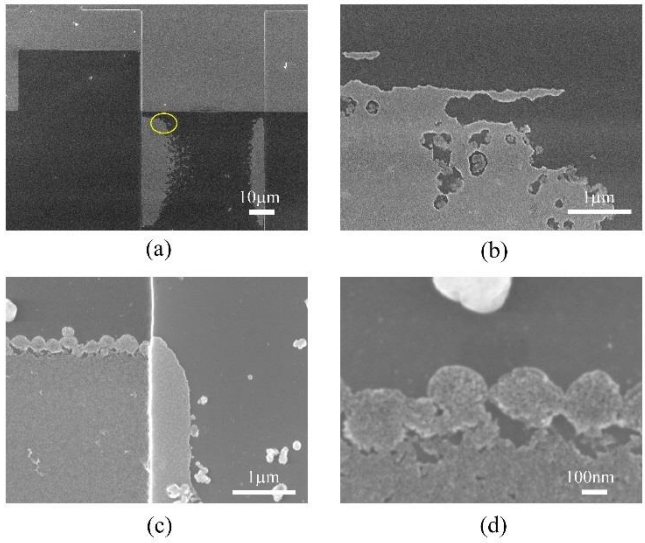

Figure 3.15: SEM images of S^{2-} (a and b) and OH^{-} (c and d) terminated PbS QD films on 220 nm topography Si substrate (without HF treatment).

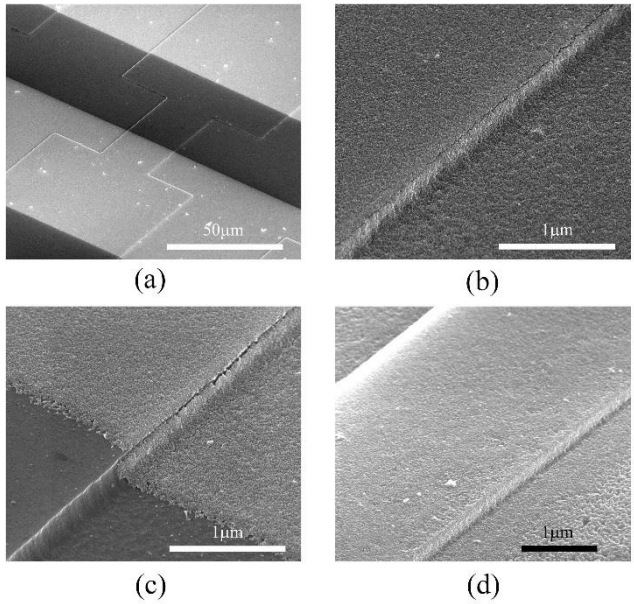

Figure 3.16: SEM images of 2 min 30 seconds etching of a micro-patterned S^{2-} terminated PbS QD film on 3D silicon substrates, formed by etching with a mixture of 1HCl:10H_3PO_4 on different magnification scales.

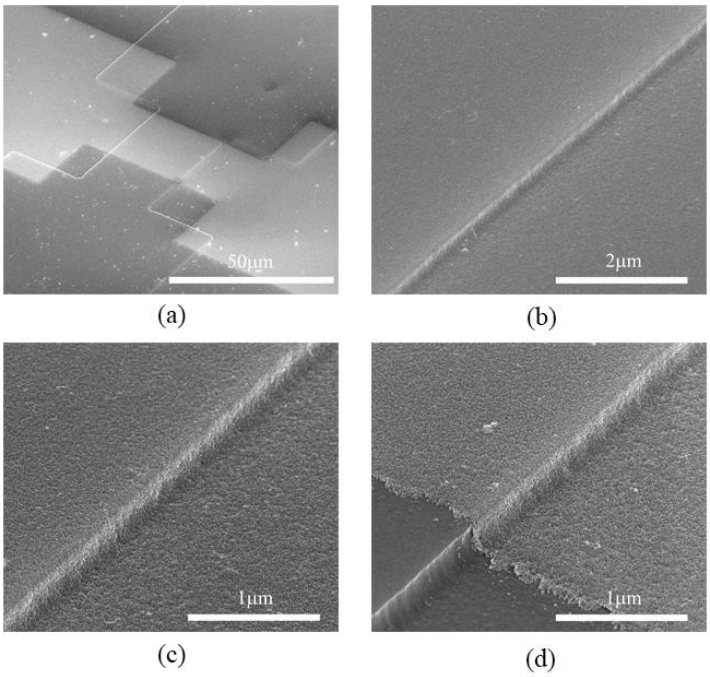

Figure 3.17: SEM images of OH^- terminated PbS QD films on 220 nm topography Si substrate.

3.3.4 Investigation of the CdSe/CdS QD film

To illustrate the versatility of the patterning recipe, we extended it to CdSe/CdS core/shell QDs by preparing CdSe/CdS QD films under the same conditions as for the PbS films. Also here, TEM analysis evidenced that the original phosphonic acid ligand could be efficiently exchanged for OH^- or S^{2-} moieties. As shown in figure 3.18, the results illustrate that the distance between CdSe/CdS QDs due to phosphonic acid long chain organic ligands (figure 3.18 (a)) slightly decreases after KOH (figure 3.18 (b)) treatment, which is similar to the ligand exchange of PbS QDs. The interparticle distance is larger however compared to the PbS-OH^- capped dots, which is attributed to an incomplete ligand exchange. The SEM images shown in figure 3.19 (a)—(c) give an overview of the patterns made, while the fluoresce microscopy image (figure 3.19 (d)) of the sample gives a first indication that the photoluminescence of the QDs is preserved during the whole process.

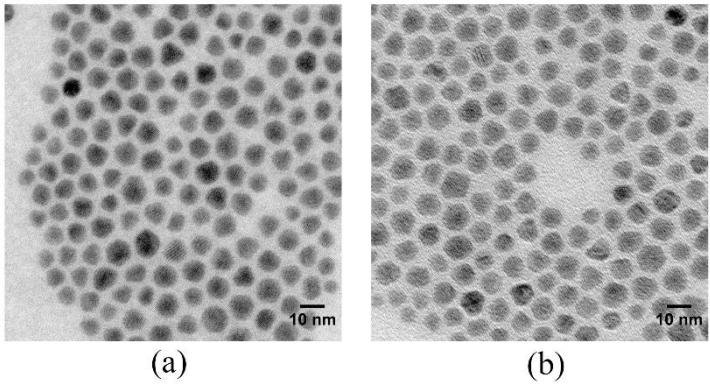

Figure 3.18: TEM images of (a) phosphonic acid and (b) OH^- capped colloidal CdSe/CdS QDs.

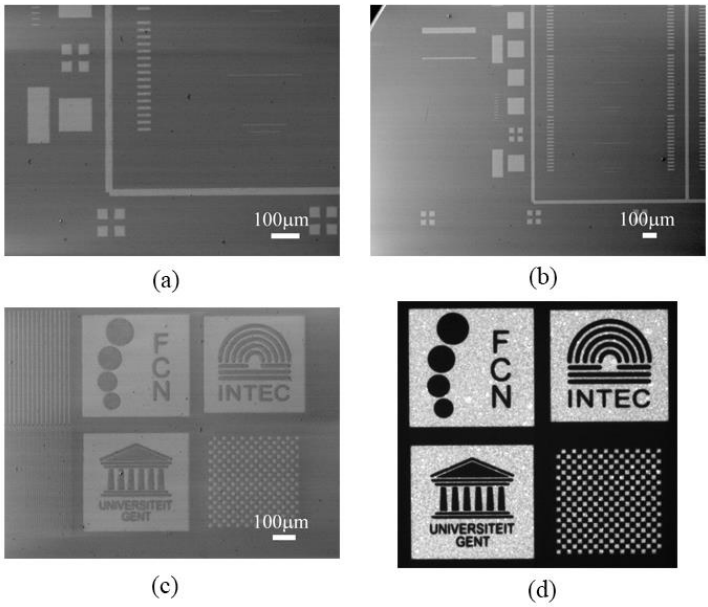

Figure 3.19: SEM images of a micro-patterned CdSe/CdS QD film on different scales (a, b and c). (d) Fluorescence microscope image of a CdSe/CdS micropatterned film.

In order to estimate the effect of micropatterning on the QY of the film, the corresponding QY of the QD films was measured using an integrating sphere that equips the Edinburgh Instruments FLSP920 spectrometer (see Appendix A). A more detailed analysis of the photoluminescence during the different steps of

process showed that the micropatterning hardly affects the emission spectrum of the QDs. As shown in figure 3.20(a), only a small red shift is found upon film formation, which is not affected by any subsequent treatment. Comparing films of CdSe/CdS QDs with their original ligands, with OH^- ligands and after micropatterning, we find that especially the replacement of the phosphonic acid ligands by OH^- (figure 3.21(b)) leads to a major drop (~56%) in photoluminescence quantum yield. The micropatterning itself only induces a minor further reduction of the PLQY by about 22%. We thus conclude that the micropatterning—including the wet etching step—leaves the QD's properties largely unaffected.

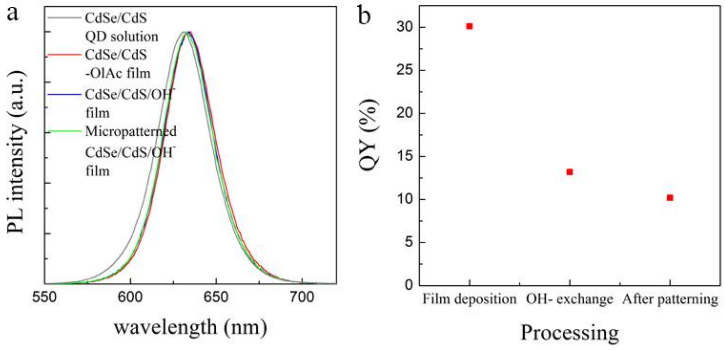

Figure 3.20: (a) Normalized photoluminescence spectra of CdSe/CdS QD suspension in toluene (grey) and CdSe/CdS QD films terminated with phosphonic acid (red), after OH^- ligand exchange (blue) and after selective wet etching (green). (b) QY of CdSe/CdS QDs in solution, after deposition, after ligand exchange with OH^- and after micro-patterning with lithography and wet etching.

3.4 Conclusions

In this chapter, we have developed a method for the micro-patterning of films of colloidal QD stabilized by inorganic ligands. Using both PbS and CdSe/CdS QDs, films were made by a layer-by-layer approach, where each cycle involves the deposition of a QD layer by dip-coating, the replacement of the native organic ligands by inorganic moieties, such as OH^- and S^{2-}, followed by a thorough cleaning of the resulting film. We demonstrated that with this method, a smooth and crack-free QD film is formed, on which a photoresist can be spun. The micropatterned films are defined by optical lithography with a positive photoresist, followed by the removal of uncovered QDs by wet etching using a HCl/H_3PO_4 mixture ($1HCl:10H_3PO_4$). High resolution films with feature dimensions down to 500 nm can be realized by this selective wet etching method, limited by the resolution of the lithographic process and a slight over-

etching, both on planar and on 3D substrates. Comparing the films of CdSe/CdS QDs with their original ligands, the replacement of the phosphonic acid ligands by OH^- leads to a major drop (~56%) in photoluminescence quantum yield. For CdSe/CdS core/shell QDs, the micro-patterned films still retained their photoluminescence after lithography and wet etching. Nearly 78% of the QY remains in this procedure. These results indicate that the low-cost micro-patterning method based on a layer-by-layer approach and selective wet etching is a very promising way to achieve the large-scale device integration of colloidal QDs, not only for light detection but also for integrated light source applications.

References

[1] H. Liu, D. Zhitomirsky, S. Hoogland, J. Tang, I. J. Kramer, Z. Ning, and E. H. Sargent, "Systematic optimization of quantum junction colloidal quantum dot solar cells," Applied Physics Letters 101, 151112 (2012).

[2] A. C. Arango, D. C. Oertel, Y. Xu, M. G. Bawendi, and V. Bulović, "Heterojunction Photovoltaics Using Printed Colloidal Quantum Dots as a Photosensitive Layer," Nano Letters 9, 860-863 (2009).

[3] W. Ma, S. L. Swisher, T. Ewers, J. Engel, V. E. Ferry, H. A. Atwater, and A. P. Alivisatos, "Photovoltaic Performance of Ultrasmall PbSe Quantum Dots," ACS Nano 5, 8140-8147 (2011).

[4] S. Keuleyan, E. Lhuillier, V. Brajuskovic, and P. Guyot-Sionnest, "Mid-infrared HgTe colloidal quantum dot photodetectors," Nat Photon 5, 489-493 (2011).

[5] J. P. Clifford, G. Konstantatos, K. W. Johnston, S. Hoogland, L. Levina, and E. H. Sargent, "Fast, sensitive and spectrally tuneable colloidal-quantum-dot photodetectors," Nat Nano 4, 40-44 (2009).

[6] T. Rauch, M. Boberl, S. F. Tedde, J. Furst, M. V. Kovalenko, G. Hesser, U. Lemmer, W. Heiss, and O. Hayden, "Near-infrared imaging with quantum-dot-sensitized organic photodiodes," Nat Photon 3, 332-336 (2009).

[7] C. Dang, J. Lee, Y. Zhang, J. Han, C. Breen, J. S. Steckel, S. Coe-Sullivan, and A. Nurmikko, "A Wafer-Level Integrated White-Light-Emitting Diode Incorporating Colloidal Quantum Dots as a Nanocomposite Luminescent Material," Advanced Materials 24, 5915-5918 (2012).

[8] B. N. Pal, Y. Ghosh, S. Brovelli, R. Laocharoensuk, V. I. Klimov, J. A. Hollingsworth, and H. Htoon, "'Giant' CdSe/CdS Core/Shell Nanocrystal Quantum Dots As Efficient Electroluminescent Materials: Strong Influence of Shell Thickness on Light-Emitting Diode Performance," Nano Letters 12, 331-336 (2012).

[9] I. Moreels, Y. Justo, B. De Geyter, K. Haustraete, J. C. Martins, and Z. Hens, "Size-Tunable, Bright, and Stable PbS Quantum Dots: A Surface Chemistry Study," ACS Nano 5, 2004-2012 (2011).

[10] M. V. Kovalenko, E. Kaufmann, D. Pachinger, J. Roither, M. Huber, J. Stangl, G. Hesser, F. Schäffler, and W. Heiss, "Colloidal HgTe Nanocrystals with Widely Tunable Narrow Band Gap Energies: From Telecommunications to Molecular Vibrations," Journal of the American Chemical Society 128, 3516-3517 (2006).

[11] I. Moreels, K. Lambert, D. Smeets, D. De Muynck, T. Nollet, J. C. Martins, F. Vanhaecke, A. Vantomme, C. Delerue, G. Allan, and Z. Hens, "Size-Dependent Optical Properties of Colloidal PbS Quantum Dots," ACS Nano 3, 3023-3030 (2009).

[12] S. Coe-Sullivan, J. S. Steckel, W. K. Woo, M. G. Bawendi, and V. Bulović, "Large-Area Ordered Quantum-Dot Monolayers via Phase Separation During Spin-Casting," Advanced Functional Materials 15, 1117-1124 (2005).

[13] M. Singh, H. M. Haverinen, P. Dhagat, and G. E. Jabbour, "Inkjet Printing—Process and Its Applications," Advanced Materials 22, 673-685 (2010).

[14] M. Böberl, M. V. Kovalenko, S. Gamerith, E. J. W. List, and W. Heiss, "Inkjet-Printed Nanocrystal Photodetectors Operating up to 3 μm Wavelengths," Advanced Materials 19, 3574-3578 (2007).

[15] E. Tekin, P. J. Smith, S. Hoeppener, A. M. J. van den Berg, A. S. Susha, A. L. Rogach, J. Feldmann, and U. S. Schubert, "Inkjet Printing of Luminescent CdTe Nanocrystal–Polymer Composites," Advanced Functional Materials 17, 23-28 (2007).

[16] J. J. Urban, D. V. Talapin, E. V. Shevchenko, and C. B. Murray, "Self-Assembly of PbTe Quantum Dots into Nanocrystal Superlattices and Glassy Films," Journal of the American Chemical Society 128, 3248-3255 (2006).

[17] J. Yolanda, M. Iwan, L. Karel, and H. Zeger, "Langmuir?Blodgett monolayers of colloidal lead chalcogenide quantum dots: morphology and photoluminescence," Nanotechnology 21, 295606 (2010).

[18] K. Lambert, R. K. Čapek, M. I. Bodnarchuk, M. V. Kovalenko, D. Van Thourhout, W. Heiss, and Z. Hens, "Langmuir−Schaefer Deposition of Quantum Dot Multilayers," Langmuir 26, 7732-7736 (2010).

[19] H. Bourvon, S. Le Calvez, H. Kanaan, S. Meunier-Della-Gatta, C. Philippot, and P. Reiss, "Langmuir–Schaeffer Monolayers of Colloidal Nanocrystals for Cost-Efficient Quantum Dot Light-Emitting Diodes," Advanced Materials 24, 4414-4418 (2012).

[20] J. Tang, K. W. Kemp, S. Hoogland, K. S. Jeong, H. Liu, L. Levina, M. Furukawa, X. Wang, R. Debnath, D. Cha, K. W. Chou, A. Fischer, A. Amassian, J. B. Asbury, and E. H. Sargent, "Colloidal-quantum-dot photovoltaics using atomic-ligand passivation," Nat Mater 10, 765-771 (2011).

[21] Z. Ning, D. Zhitomirsky, V. Adinolfi, B. Sutherland, J. Xu, O. Voznyy, P. Maraghechi, X. Lan, S. Hoogland, Y. Ren, and E. H. Sargent, "Graded Doping for Enhanced Colloidal Quantum Dot Photovoltaics," Advanced Materials 25, 1719-1723 (2013).

[22] G. Konstantatos, and E. H. Sargent, "Nanostructured materials for photon detection," Nat Nano 5, 391-400 (2010).

[23] M. Chen, H. Yu, S. V. Kershaw, H. Xu, S. Gupta, F. Hetsch, A. L. Rogach, and N. Zhao, "Fast, Air-Stable Infrared Photodetectors based on Spray-Deposited Aqueous HgTe Quantum Dots," Advanced Functional Materials 24, 53-59 (2014).

[24] J.-H. Choi, A. T. Fafarman, S. J. Oh, D.-K. Ko, D. K. Kim, B. T. Diroll, S. Muramoto, J. G. Gillen, C. B. Murray, and C. R. Kagan, "Bandlike Transport in Strongly Coupled and Doped Quantum Dot Solids: A Route to High-Performance Thin-Film Electronics," Nano Letters 12, 2631-2638 (2012).

[25] D. V. Talapin, J.-S. Lee, M. V. Kovalenko, and E. V. Shevchenko, "Prospects of colloidal nanocrystals for electronic and optoelectronic applications," Chemical reviews 110, 389-458 (2009).

[26] A. H. Ip, S. M. Thon, S. Hoogland, O. Voznyy, D. Zhitomirsky, R. Debnath, L. Levina, L. R. Rollny, G. H. Carey, A. Fischer, K. W. Kemp, I. J. Kramer, Z. Ning, A. J. Labelle, K. W. Chou, A. Amassian, and E. H. Sargent, "Hybrid passivated colloidal quantum dot solids," Nat Nano 7, 577-582 (2012).

[27] G. Konstantatos, M. Badioli, L. Gaudreau, J. Osmond, M. Bernechea, F. P. G. de Arquer, F. Gatti, and F. H. L. Koppens, "Hybrid graphene-quantum dot phototransistors with ultrahigh gain," Nat Nano 7, 363-368 (2012).

[28] E. Talgorn, M. A. de Vries, L. D. A. Siebbeles, and A. J. Houtepen, "Photoconductivity Enhancement in Multilayers of CdSe and CdTe Quantum Dots," ACS Nano 5, 3552-3558 (2011).

[29] W. K. Bae, J. Kwak, J. Lim, D. Lee, M. K. Nam, K. Char, C. Lee, and S. Lee, "Multicolored Light-Emitting Diodes Based on All-Quantum-Dot Multilayer Films Using Layer-by-Layer Assembly Method," Nano Letters 10, 2368-2373 (2010).

[30] O. E. Semonin, J. M. Luther, S. Choi, H.-Y. Chen, J. Gao, A. J. Nozik, and M. C. Beard, "Peak External Photocurrent Quantum Efficiency Exceeding 100% via MEG in a Quantum Dot Solar Cell," Science 334, 1530-1533 (2011).

[31] W. Liu, J.-S. Lee, and D. V. Talapin, "III–V Nanocrystals Capped with Molecular Metal Chalcogenide Ligands: High Electron Mobility and Ambipolar Photoresponse," Journal of the American Chemical Society 135, 1349-1357 (2013).

[32] K. Lambert, I. Moreels, D. V. Thourhout, and Z. Hens, "Quantum Dot Micropatterning on Si," Langmuir 24, 5961-5966 (2008).

[33] P. Yeonsang, R. Young-Geun, K. Un Jeong, C. Dae-Young, S. Hwansoo, K. Jineun, C. Sangmo, L. Jaesoong, K. Tae-Ho, C. Kyung-Sang, and L. Chang-Won, "Nanoscale patterning of colloidal quantum dots on transparent and metallic planar surfaces," Nanotechnology 23, 355302 (2012).

[34] V. Nandwana, C. Subramani, Y.-C. Yeh, B. Yang, S. Dickert, M. D. Barnes, M. T. Tuominen, and V. M. Rotello, "Direct patterning of quantum dot nanostructuresviaelectron beam lithography," Journal of Materials Chemistry 21, 16859-16862 (2011).

[35] L. Kim, P. O. Anikeeva, S. A. Coe-Sullivan, J. S. Steckel, M. G. Bawendi, and V. Bulović, "Contact Printing of Quantum Dot Light-Emitting Devices," Nano Letters 8, 4513-4517 (2008).

[36] J. J. Gassensmith, P. M. Erne, W. F. Paxton, M. Frasconi, M. D. Donakowski, and J. F. Stoddart, "Patterned Assembly of Quantum Dots onto Surfaces Modified with Click Microcontact Printing," Advanced Materials 25, 223-226 (2013).

[37] R. K. Kramer, N. Pholchai, V. J. Sorger, T. J. Yim, R. Oulton, and X. Zhang, "Positioning of quantum dots on metallic nanostructures," Nanotechnology 21, 145307 (2010).

[38] C. H. Lalander, Y. Zheng, S. Dhuey, S. Cabrini, and U. Bach, "DNA-Directed Self-Assembly of Gold Nanoparticles onto Nanopatterned Surfaces: Controlled Placement of Individual Nanoparticles into Regular Arrays," ACS Nano 4, 6153-6161 (2010).

[39] A. Nag, M. V. Kovalenko, J.-S. Lee, W. Liu, B. Spokoyny, and D. V. Talapin, "Metal-free Inorganic Ligands for Colloidal Nanocrystals: S^{2-}, HS^{-}, Se^{2-}, HSe^{-}, Te^{2-}, HTe^{-}, TeS_3^{2-}, OH^{-}, and NH_2^{-} as Surface Ligands," Journal of the American Chemical Society 133, 10612-10620 (2011).

[40] L. Carbone, C. Nobile, M. De Giorgi, F. D. Sala, G. Morello, P. Pompa, M. Hytch, E. Snoeck, A. Fiore, I. R. Franchini, M. Nadasan, A. F. Silvestre, L. Chiodo, S. Kudera, R. Cingolani, R. Krahne, and L. Manna, "Synthesis and

Micrometer-Scale Assembly of Colloidal CdSe/CdS Nanorods Prepared by a Seeded Growth Approach," Nano Letters 7, 2942-2950 (2007).

[41] C. Hu, A. Gassenq, Y. Justo, S. Yakunin, W. Heiss, Z. Hens, and G. Roelkens, "Short-wave infrared colloidal quantum dot photodetectors on silicon," in SPIE OPTO(International Society for Optics and Photonics, 2013), pp. 863127-863127-863128.

[42] M. Montalti, A. Credi, L. Prodi, and M. T. Gandolfi, Handbook of photochemistry (CRC press, 2006).

4

Air-stable Short-wave Infrared PbS Colloidal Quantum Dot Photoconductors passivated with Al_2O_3 Atomic layer deposition

4.1 Introduction

Many molecules what we want to detect in our environment have bands of absorption lines in the short-wave infrared (SWIR). Traditional high-sensitivity photodetectors used in these spectroscopic systems are discrete components based on epitaxial III-V materials [1]. While the III-V semiconductor leads to be the highest performance, the high material and integration cost of such devices prohibits large scale deployment, especially when used in a linear or two-dimensional focal plane array. Low-cost SWIR photodetectors based on colloidal QDs offers an alternative way to realize this functionality, either as

discrete components, focal plane arrays or integrated on photonic integrated circuits [2-4].

Using colloidal QDs as new photonic materials gets a lot of attention in the photonic community. The simple hot injection chemical synthesis method allows low-cost production. The fact that these QDs are available in solution and can be integrated on any substrate, including silicon, using techniques such as spin casting [5], inkjet printing [6], and Langmuir-Blodgett (LB) deposition [7], offers a route to the cost reduction of SWIR components as compared to epitaxially grown layer stacks. Furthermore, due to the quantum size effect, the QDs electrical and optical properties (such as the absorption cut-off wavelength, luminescence wavelength) can be easily tuned by varying the QD size [8]. The interest in these materials is therefore not limited to photodetection [9] but also encompasses light emitting diodes [10] and photovoltaics [11]. Critical for photodetector and photovoltaic applications is the replacement of the long isolating organic ligands capping as-synthesized QDs by shorter moieties to enhance carrier mobility in QD films [12]. Also, making the colloidal QD devices air-stable is of key importance for a practical application. For the purpose of obtaining air-stable QD devices, the main issue is to avoid oxidation of the QD film. This requires a well passivating, pinhole-free layer that is transparent at the detection wavelengths. Atomic layer deposition (ALD) usually results in films without pinholes and is therefore very suitable for passivation. Al_2O_3, which is probably the most extensively characterized material in ALD, is a natural choise in this respect since it is a wide bandgap insulator that is transparent in the short-wave infrared. Al_2O_3 layers 30 nm thick are used in this work since such layers are known to be pinhole free.

In this study, we use ALD to deposit Al_2O_3 films on PbS colloidal QD films for passivation and implement air-stable SWIR photodetectors. Homogeneous and crack-free QD films are obtained by a layer-by-layer (LBL) approach, where each cycle involves a QD layer deposition through dip coating, followed by a replacement of the native organic ligand by a metal-free inorganic ligand, such as OH^- and S^{2-} [13]. Afterwards, a thorough cleaning procedure is used to remove impurities. One significant advantage of this approach is that there is no need for a stable QD dispersion with short ligands, and that the cracks formed during ligand exchange in the layer-by-layer approach are refilled in the next deposition step. For surface illuminated detectors, the QD films are formed on prefabricated interdigitated electrodes, where selective wet etching is used to pattern the QD film [13]. The resulting photodetectors are then passivated with an aluminum oxide coating through ALD [14-17]. Long term air-stable PbS colloidal QD photodetectors with 2.4 μm cut-off wavelength are obtained this way.

4.2 Photodetector: Figures of merit

Many materials and devices are under development to improve light detection for different purposes. Photodetectors come in various flavors including photoconductors, photodiodes and phototransistors. In this work we mainly focus on photoconductors. Several figures of merit are used to characterize and evaluate the performance of photoconductive photodetectors, such as responsivity, detectivity, etc. They will be summarized in this section.

4.2.1 Detector responsivity

Responsivity R (A/W) is introduced to quantify the signal output from the photodetector i_{ph} per unit optical input power P_{in} and is expressed as:

$$R = \frac{i_{ph}}{P_{in}} \tag{4.1}$$

Generally responsivity is dependent on many parameters, such as modulation frequency (f), incident photon wavelength (λ), applied bias voltage, working temperature, incident power level, etc. The spectral response can be used to describe the dependence of responsivity on the incident photon wavelength.
The photocurrent i_{ph} in a photoconductive photodetector is usually described as:

$$i_{ph} = \eta q N_\lambda G_i \tag{4.2}$$

where η is the quantum efficiency and defined as the ratio between electron generation rate and the incident photon flux ($P_{in}/h\nu$), q is the elementary charge, N_λ is the number of photons incident per unit time on the sample at wavelength λ, and G_i is the internal photoconductive gain of the device.

The internal photoconductive gain of the photodetector, G_i, is determined by the ratio between free carrier lifetime τ and carrier transit time T_t between the two electrodes of the device:

$$G_i = \frac{\tau}{T_t} \tag{4.3}$$

When the carrier lifetime is longer than the carrier transit time, i.e. $G_i > 1$, this indicates the majority carriers can flow in an external circuit for multiple cycles before they recombine. By engineering carrier life and carrier transit time, the corresponding photoconductive gain can be properly controlled. The carrier

life time can be mainly adjusted through engineering long-living traps in the material. The carrier transit time τ has the following relation with the conducting channel length L, carrier mobility μ, and the electric field E:

$$T_t = \frac{L}{\mu E} \tag{4.4}$$

Therefore, the carrier transit time can be modified through device design and improving the mobility of the material.

When the applied bias voltage is V, considering the relation V = EL and $N_\lambda = P_{in}/h\nu$, the photocurrent can be expressed as follows:

$$i_{ph} = \eta q \left(\frac{P_{in}}{h\nu}\right)\left(\frac{\mu\tau V}{L^2}\right) \tag{4.5}$$

4.2.2 Photoconductor noise

In photoconductive photodetectors, several internal noise sources exist: Johnson noise, shot noise, generation-recombination (G-R) noise, and 1/f noise.

Thermal noise, which is also called Johnson noise or Nyquist noise, is due to the random thermal motion of charge carriers in resistors even in absence of an applied bias voltage. It can be expressed as

$$i_T = \sqrt{\frac{4kTB}{R}} \tag{4.6}$$

Where k is the Boltzmann constant, T is the absolute temperature, B is the effective noise bandwidth and R is the detector resistance. From the expression, one can see that the thermal noise is independent of the applied bias.

Shot noise originates from the random fluctuations of carrier flux in a DC current due to the discrete charges making up that electric current. The expression for shot noise is given by

$$i_s = \sqrt{2qIB} \tag{4.7}$$

where q is the electron elementary charge, I is the DC current and B is the effective noise bandwidth.

Generation-recombination noise is a consequence of random generation and recombination of nonequilibrium free charge carriers. Many expressions for G-R noise exist which depends on the internal properties of the semiconductors.

$1/f$ noise, as the name indicates, has a $1/f$ noise power spectrum. At low frequencies $1/f$ noise becomes dominant in infrared detectors. At high

frequencies its amplitude drops below the other types of noise, such as Johnson noise or generation-recombination noise. It is usually expressed as follows:

$$i_{1/f} = \sqrt{\frac{KI^{\alpha}B}{f^{\beta}}} \tag{4.8}$$

where K is a proportionality factor, I is bias current, f is the frequency, α is a constant whose value is approximately 2 and β is also constant whose value is about unity. $1/f$ noise is normally associated with the potential barriers at the contacts and surface trap states. The reduction of $1/f$ noise is an experimental art which mainly relies on contacts and surface trap states preparation.

4.2.3 Noise equivalent power (NEP) and detectivity

Due to the existence of internal noise inside of the photodetector, for a signal to be detected should be higher than the noise level. Signal-to-noise ratio (SNR) is defined by

$$SNR = \frac{RP_{in}}{i_{in}} \tag{4.9}$$

Where R is the responsivity, P_{in} is the incident optical power and i_n is the noise current. The noise equivalent power is the minimum power which can be detected by the photodetector. It is defined as the optical power for which the SNR is equal to unity:

$$NEP = \frac{i_n}{R} \tag{4.10}$$

However, the noise equivalent power cannot be used to compare the performance between different kinds of photodetector since it scales with the surface area. Therefore, an surface area independent figure of merit, detectivity D^*, is proposed to compare the performance between different photodetectors. The expression for the detectivity D^* is given by

$$D^* = \frac{\sqrt{AB}}{NEP} = \frac{\sqrt{AB}R}{i_n} \tag{4.11}$$

In this expression, A is the active detector area, B is the effective noise bandwidth, R is the responsivity and i_n is the noise current. Like responsivity,

the detectivity D^* is also determined by many parameters, e.g., modulation frequency (f), incident photon wavelength (λ), applied bias voltage, working temperature, etc. The detectivity indicates the signal-to-noise ratio under 1 Watt optical incident power impinging on a 1 cm^2 detector surface area for a 1 Hz measurement bandwidth. The unit of detectivity is $cm \cdot Hz^{1/2}W^{-1}$, which is also named Jones.

4.2.4 Response time and frequency response

Response time is also called the time constant τ, being the time duration over which the photodetector signal drops to e^{-1} when the optical signal is switched off, i.e., approximately 37 % from its steady value. It is expressed as

$$\tau = \frac{1}{2\pi f_{3dB}} \tag{4.12}$$

where f_{3dB} is the 3 dB bandwidth of photodetector. In a photoconductor f_{3dB} is reached when the photocurrent value reduced to $1/\sqrt{2}$ (~ 0.707) from its peak value at zero frequency (DC photocurrent case).

In frequency domain, the responsivity of a photodetector can be written as:

$$R(f) = \frac{R_0}{\sqrt{1 + (2\pi f\tau)^2}} \tag{4.13}$$

where R_0 is the responsivity at zero frequency, f is the frequency and τ is the response time.

4.2.5 Dynamic range

Dynamic range (DR) is defined as the ratio of the maximum and the minimum optical power that can be detected. The unit of dynamic range is usually in decibel (dB) and it can be expressed as

$$DR = 20lg\frac{P_{max}}{P_{min}} \tag{4.14}$$

where P_{max} is the maximum optical incident power where photocurrent saturation occurs and P_{min} is the minimum incident power that can be detected, i.e., the NEP.

4.3 Fabrication of colloidal QD photodetectors

As shown in Figure 4.1, the fabrication of the PbS photodetectors started with the deposition of a 500 nm thick insulating SiO_2 layer with plasma enhanced chemical vapor deposition (PECVD) on a silicon substrate. Afterwards, a pair of interdigitated Ti/Au (10 nm Ti, 100 nm Au) finger electrodes was defined through optical lithography and lift-off. The electrodes were designed to be 2 μm apart (limited by the resolution of the lithography system). Afterwards, QD films were deposited by LBL deposition, dipping the substrates with the prefabricated metal electrodes into a PbS QD dispersion in toluene with a QD concentration of 1 μM and pulling it out at a speed of 80 mm min^{-1}. After complete drying, the QD film was re-immersed into a solution of either $Na_2S{\cdot}9H_2O$ (10 mg mL^{-1}) or KOH (0.01 mg mL^{-1}) in formamide to exchange the OlAc ligands by S^{2-} or OH^- moieties respectively for the desired ligand exchange time, typically 60 s for S^{2-} and 10 s for OH^-. After that the sample was washed by immersing it twice in formamide and acetone, followed by a final dip in isopropanol to remove residual impurities introduced during ligand exchange. The resulting films were dried under nitrogen. A multilayer film can be formed by repeating this dip coating/ligand exchange procedure. The photodetectors were fabricated by 15 times LBL deposition. Afterwards a selective wet-etching approach was used to realize micropatterned QD films on the prefabricated electrodes, resulting in PbS QD films of 130 μm by 104 μm. Then atomic layer deposition of Al_2O_3 was used to passivate the devices. Al_2O_3 was used since it is a very well characterized material in ALD and it is transparent in the SWIR. The depositions were carried out in a home-built hot wall ALD reactor. The ALD chamber was pumped by a turbomolecular pump to a base pressure of 10^{-4} Pa. Samples were introduced via a load lock and placed on a resistive heating element located at the center of the chamber. A thermal ALD process at 100 ℃ was used to grow Al_2O_3. The samples were sequentially exposed to 3 seconds of TMA (trimethylaluminum) and 3 seconds of water vapor at a pressure of $5{\cdot}10^{-1}$ Pa. 300 ALD cycles were performed, resulting in a 30 nm thick pinhole free alumina film on a silicon reference (measured on a silicon reference by ellipsometry).

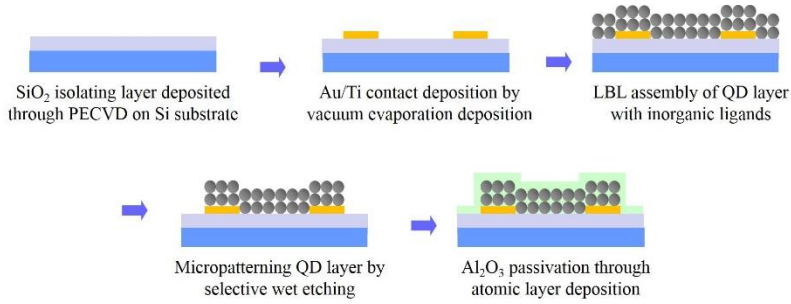

Figure 4.1: Process flow of PbS colloidal photodetector fabrication.

A top view of a processed PbS QD photodetector for surface illumination is shown in Figure 4.2(a). In this study, we used PbS QDs with an excitation peak wavelength at 2.09 µm, according to the PbS sizing curve, this corresponds to an inorganic core diameter of 9 nm as confirmed by TEM measurement (Figure 4.2(b, c)). Due to the size dispersion of the QDs, the absorption edge extends to about 2.4 µm. In order to investigate the relationship between the film thickness and the number of LBL deposition cycles, samples with 2, 4, 6, 8, and 10 LBL deposition cycles were realized. To determine the QD film thickness, we measured the average height profile of the micropatterned QD films by atomic force microscopy (AFM), both before and after Al_2O_3 deposition (see Figure 4.3). For both PbS/S^{2-} and PbS/OH^-, a linear trend can be observed accounting to a 6.5 nm and 5.5 nm thickness increase per LBL cycle, respectively. This is less than the diameter of a single nanocrystal, which is most likely related to the ligand exchange inducing a volume loss and particle clustering by removal of the long organic ligands. The resulting voids are then refilled in the following deposition cycle, which reduces the thickness increase per cycle. As shown in Figure 4.3(a), Al_2O_3 growth by ALD does not affect this thickness increase per deposition cycle. This is due to the conformal nature of ALD, the ALD coating has been added over the complete device surface, retaining the underlying geometry.

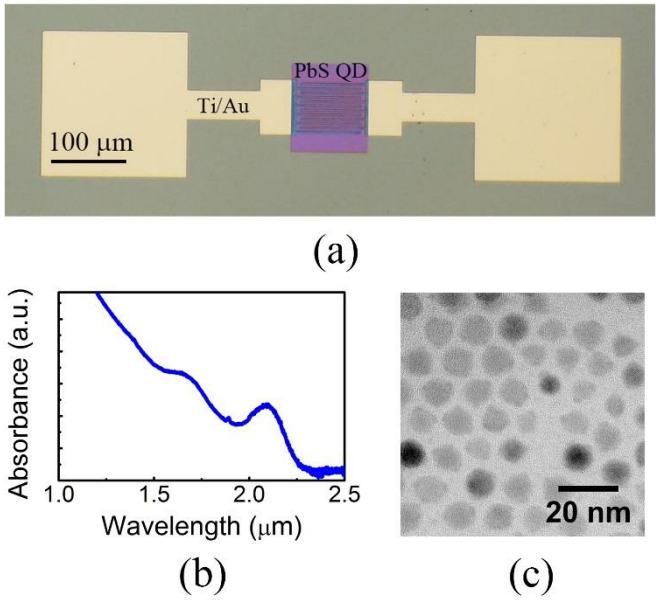

Figure 4.2: (a) Top view of the PbS QD photoconductor. (b) Absorbance spectrum of the PbS QDs used (solvent: tetrachloroethylene). (c) A TEM image of OlAc-terminated colloidal PbS QDs.

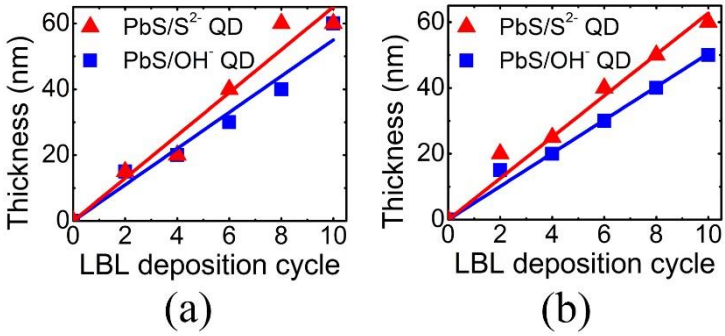

Figure 4.3: (a) Thickness of micropatterned PbS films as a function of the number of LBL cycles without Al_2O_3 deposition (b) The same, after Al_2O_3 deposition.

4.4 Photodetector characterization

4.4.1 Photoconductivity studies

The current-voltage characteristics of PbS photoconductors under different illumination intensity were measured by surface illumination with a fiber coupled laser at 1550 nm. The I-V characteristics as a function of incident optical power for PbS/S^{2-} and PbS/OH^- photoconductors with 15 LBL deposition cycles are shown in Figure 4.4. Under illumination, the S^{2-} terminated device resistance decreased from 3.30 kΩ in the dark to 1.09 kΩ under 11W/cm^2 optical illumination intensity. After passivation with a 30 nm thick Al_2O_3 film, the dark resistivity became 28.0 kΩ and decreased to 4.18 kΩ under the same illumination intensity of 11W/cm^2. As shown in Figure 4.4(c) and 4.4(d), similar results are obtained using OH^- terminated PbS QD detectors. The I-V characteristic difference between PbS/S^{2-} and PbS/OH^- photoconductors mainly comes from the different passivation ligands, which change the electronic coupling between the QDs. As TEM images illustrate in Chapter 3, after ligand exchange, the S^{2-} terminated QDs tend to connect epitaxially, opposed to the OH^- terminated QDs. The closer spacing of S^{2-} terminated QDs result in a higher electrical conductivity in these devices.

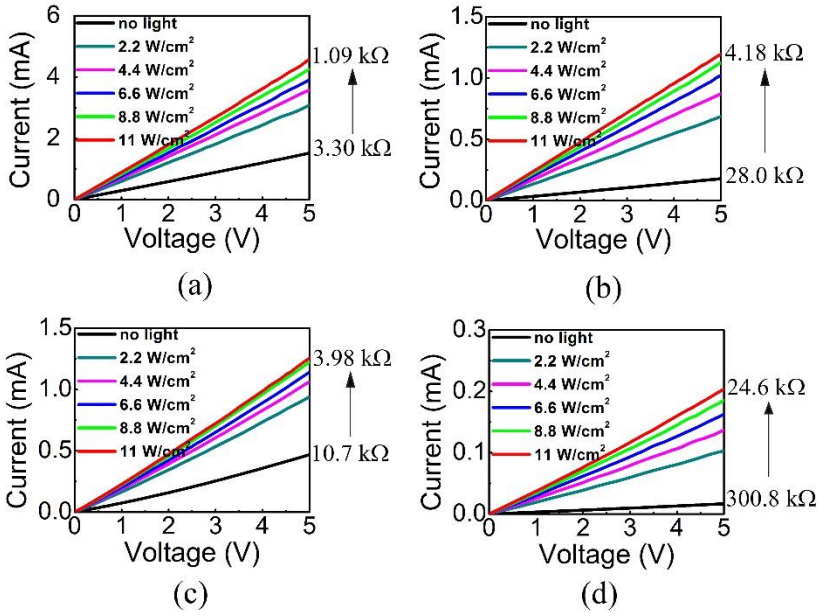

Figure 4.4: Current-Voltage characteristics of processed PbS colloidal QD photoconductors: PbS/S^{2-} detector (a) without and (b) with 30 nm Al_2O_3 passivation; PbS/OH^- detector (c) without and (d) with 30 nm Al_2O_3 passivation.

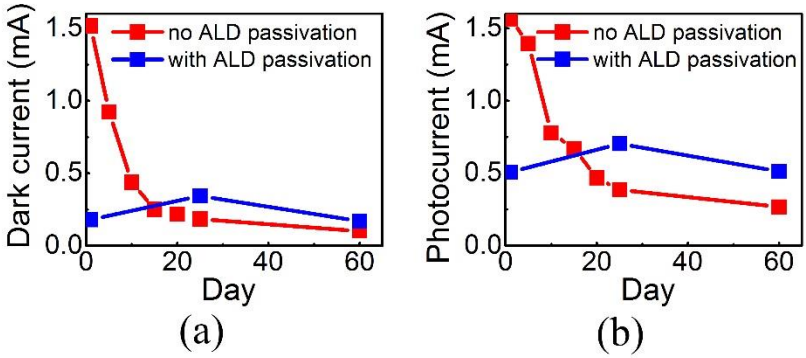

Figure 4.5: PbS/S^{2-} QD photodetector dark current (a) and photocurrent under 2.2 W/cm^2 optical illumination (b) and 5V bias as a function of time.

The characteristics of the photodetectors based on unpassivated QD films were found to degrade with time, which we attribute to oxidation of the PbS QD surface. Overcoating the PbS QD films by Al_2O_3 proved to be an efficient way to avoid this degradation, by avoiding exposure of the quantum dots to oxygen and water. Figure 4.5(a) and 4.5(b) show the dark current and photocurrent of the PbS/S^{2-} QD photodetector under 2.2 W/cm^2 illumination at 5 V bias as a function of time. The unpassivated device showed a pronounced progressive decay of both the dark current and the photocurrent. On the other hand, the response of the PbS/S^{2-} QD based photodetector passivated by a 30 nm Al_2O_3 film proved to be air-stable for 60 days at least. Moreover, although the ALD passivation led to a decrease in both dark current and photocurrent (opposite to what is reported in other reports in literature [18]), which is attributed to the penetration of Al_2O_3 in the QD film, its responsivity exceeds that of the unpassivated device after 20 days in air. We thus conclude that the ALD deposition of Al_2O_3 can be used to passivate PbS QD films and form air-stable QD photodetectors.

4.4.2 Film characterization

After ALD passivation, a decrease in both dark current and photocurrent was observed. For the purpose of understanding this phenomenon, X-ray photoelectron spectroscopy (XPS) was used to analyze the elemental composition of the QD films. All measurements were recorded on an X-ray photoelectron spectroscopy S-Probe XPS spectrometer with monochromated Al (1486 eV) exciting radiation from Surface Science Instruments (VG). Samples were attached to the stage with conducting carbon tape. In order to compensate

the charging of the sample, a nickel grid was used. It was placed ~ 2 mm above the sample. A low energy electron flood gun (3 eV) was used as neutralizer and bridges with conducting Cu tape were made. Calculation of the atomic concentrations and peak fittings were performed using Shirley background substraction and Scoffield sensitivity factors with Casa XPS software.

The sputtering experiment was used to analyze the entire depth profile. For a PbS/S^{2-} QD film without ALD coating, oxygen was present on the surface due to surface contamination. In the measurement after 200 s of sputtering, no oxygen was observed anymore (Figure 4.6a). With the appearance of Si in the sample, oxygen re-appears, this is probably due to the SiO_2 layer on the substrate. Within the bulk Si substrate again, no S^{2-} was observed any more. Shown in Figure 4.6b is the depth profile of a PbS/S^{2-} QD film with 30 nm Al_2O_3 coating. At the surface almost pure Al_2O_3 was observed, with traces of Pb. After 1000 seconds, the Pb 4f peaks became more pronounced and S 2p peaks were observed. In the depth profile there is a clear overlap of Al 2s and Pb 4f/S 2p peaks, this indicated that there is an infill of Al into interstitial spaces of PbS QD film during the ALD process, resulting a pure top Al_2O_3 coating film and a PbS/Al_2O_3 coating nanocomposite film. This barrier leads to the quenching of dark current and photocurrent after ALD deposition. Similar results were found in PbS/OH^- films (Figure 4.7).

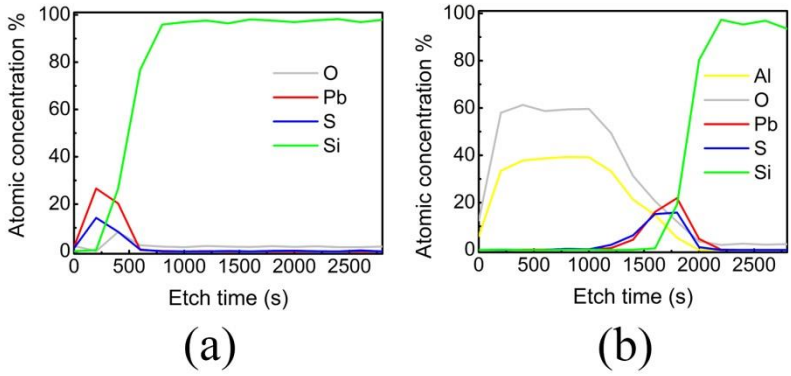

Figure 4.6: Sputtering experiment, XPS depth profile of PbS/S^{2-} detector (a) without and (b) with 30 nm Al_2O_3 passivation, steps of 200 seconds.

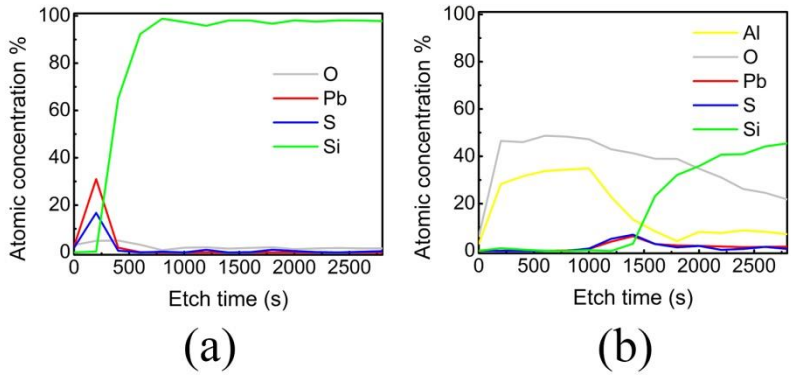

Figure 4.7: Sputtering experiment, XPS depth profile of PbS/OH^- detector (a) without and (b) with 30 nm Al_2O_3 passivation, steps of 200 seconds.

4.4.3 Device characterization

The spectral response of the PbS photoconductors is shown in Figure 4.8(a) as measured with a fiber coupled tunable laser, under 5 V bias (1.1 W/cm^2 optical illumination intensity). A photoresponse extending to 2.4 μm was found for both PbS/S^{2-} and PbS/OH^- based detectors. Figure 4.10(b) shows the responsivity of the PbS/S^{2-} and PbS/OH^- QD photodetectors as a function of power level, clearly illustrating a nonlinear response of the device. The responsivity of the PbS/S^{2-} photodetector can reach more than 50 A/W for 100 nW optical power at 5 V bias. This photoconductive gain reflects a long carrier lifetime—resulting from trap states inside the QD film—compared to the carrier transit time between the electrodes. The power dependent responsivity is attributed to the filling of these long-lived trap states with increasing illumination power, which reduces the internal photoconductive gain [3, 6]. For PbS/OH^- QD photodetectors, a responsivity of 8 A/W is obtained under the same conditions.

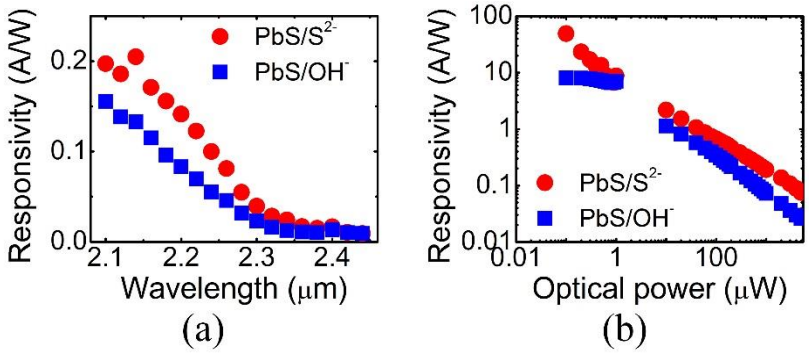

Figure 4.8: (a) Spectral response as a function of wavelength; (b) responsivity as a function of optical illumination at 1550 nm (bias voltage 5 V) for the PbS/S^{2-} and PbS/OH^{-} QD photodetectors.

The noise current density at 300 K of the ALD passivated PbS/S^{2-} and PbS/OH^{-} photoconductors measured at different bias were obtained by a commercial Berkeley Technology Associates (BTA) setup with ProPlussolutions software and the corresponding results are shown in Figure 4.9(a). A specific detectivity of 3.4×10^8 Jones and 2.3×10^8 Jones at 1550 nm at a frequency of 3 Hz is obtained under 5 V bias for PbS/S^{2-} and PbS/OH^{-} based detectors, respectively. In this study, a photoconductor was used where the photocurrent increase linearly with the applied bias voltage. As a consequence, the detector responsivity also increases according to the applied bias, which may lead to an increase in detectivity. Therefore, the responsivity and detectivity of PbS/S^{2-} QD detectors as a function of bias voltage at 100 nW illumination power are compared and listed in Table 4.1. As the results illustrate, from 1 to 5 V bias the detectivity does not have a strong dependence on bias voltage for the PbS/S^{2-} QD detector, which is related to an increase of the noise current density with increased bias. Therefore, the specific detectivity is found to be quasi-independent of the bias voltage between 1 and 5 V. A similar analysis is also made for the PbS/OH^{-} QD detector and listed in Table 4.2. Also in this case the specific detectivity is quasi-independent of bias.

Bias Voltage (V)	Responsivity (A/W)	Detectivity (Jones)
1	9.46	3.2×10^8
3	28.91	3.5×10^8
5	49.18	3.4×10^8

Table 4.1: Responsivity and specific detectivity values obtained under different bias voltage of PbS/S^{2-} QD detectors.

Bias Voltage (V)	Responsivity (A/W)	Detectivity (Jones)
1	1.33	4×10^8
3	4.25	1.61×10^8
5	8.03	2.3×10^8

Table 4.2: Responsivity and specific detectivity values obtained under different bias voltage of PbS/OH^- QD detectors.

The frequency response of PbS/S^{2-} and PbS/OH^- photodetectors under 5 V bias is shown in Figure 4.9(b). The 3-dB bandwidth of the PbS/S^{2-} and PbS/OH^- detectors are 40 Hz and 11 Hz, respectively, which is compatible with basic imaging applications. The larger bandwidth of the PbS/S^{2-} devices is attributed to shorter carrier trap times in the quantum dot film.

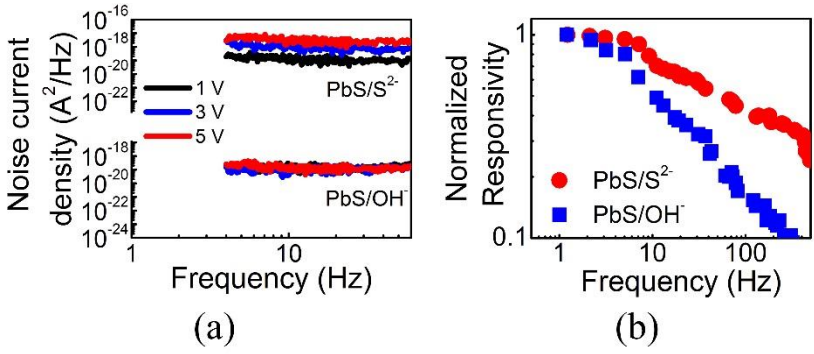

Figure 4.9: (a) Noise current density at different bias voltages for the PbS/S^{2-} and PbS/OH^- QD photodetectors at 230 K; (b) Frequency response (5V bias).

In order to estimate the corresponding quantum efficiency of the photoconductors, RODIS (Rigorous Optical Diffraction Software) software, which is based on the rigorous coupled wave analysis algorithm [19, 20], was used for the optical simulation. In all the cases the simulations are performed under surface normal incident illumination with transverse-electric (TE) and transverse-magnetic (TM) polarized light. The schematics of the device configurations are shown in Figure 4.10. The optical index n and extinction coefficient κ as a function of wavelength used in the simulation are shown in Figure 4.11, extracted from ellipsometry measurements and absorbance spectrum measurements, respectively. The quantum efficiency as a function of wavelength in non-passivated colloidal QD PbS photodetectors are shown in Figure 4.12a. The QD layer thickness is 90 nm (corresponding to 15 times LBL deposition), and the Au contact electrodes are 90 nm thick. As shown in Figure 4.12a, for TE polarized light illumination, at 1550 nm, the quantum efficiency for PbS/S^{2-} and PbS/OH^{-} photodetectors is 20.5% and 20%, respectively. For TM polarized light illumination, the quantum efficiency for PbS/S^{2-} and PbS/OH^{-} photodetectors is 14.2% and 15%, respectively. The simulated quantum efficiency results for ALD passivated photodetectors are shown in Figure 4.12b. Under TE polarized light illumination at 1550 nm, the quantum efficiency for PbS/S^{2-} and PbS/OH^{-} photodetectors is 19.6% and 21.6%, respectively. For TM polarized light illumination, the quantum efficiency for PbS/S^{2-} and PbS/OH^{-} photodetectors is 11.7% and 13.4% at 1550 nm, respectively. However, we did not observe strong polarization dependence during the measurement.

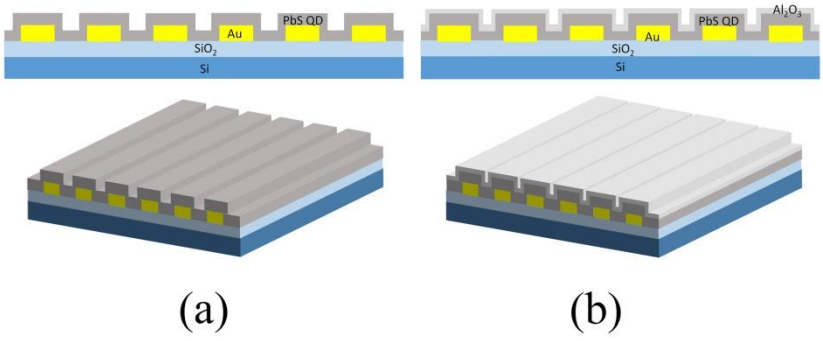

Figure 4.10: Schematics of PbS QD photodetector (a) without and (b) with 30 nm Al_2O_3 passivation.

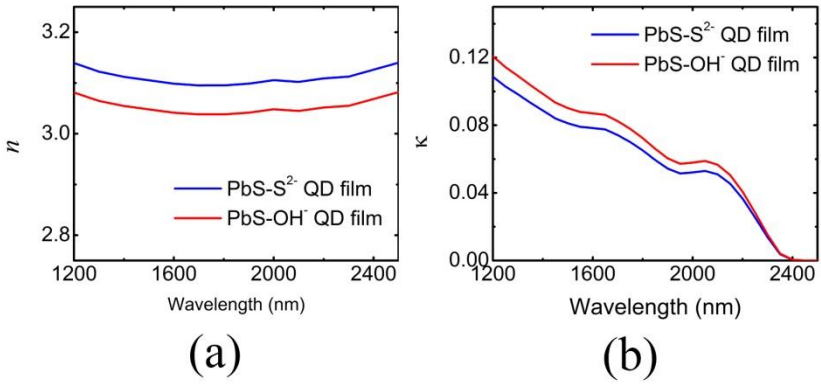

Figure 4.11: Optical index n and extinction coefficient κ of PbS QD film as a function of wavelength in the short-wave infrared range.

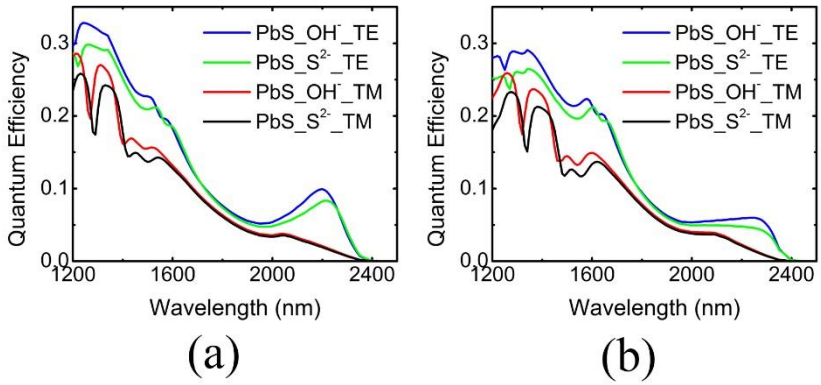

Figure 4.12: Simulated quantum efficiency of PbS QD photodetectors (a) without and (b) with 30 nm Al_2O_3 passivation in short-wave infrared range.

4.5 Conclusion

PbS colloidal quantum dots were used to realize SWIR photoconductors. Air stable devices with Al_2O_3 atomic layer deposition passivation were demonstrated. The QD films were prepared by a layer-by-layer approach to form a uniform colloidal QD film and two kinds of inorganic ligands, S^{2-} and OH^-, were investigated to facilitate carrier transport. PbS photodetectors with cutoff wavelength of 2.4 μm are obtained. We also performed a numerical simulation

on corresponding quantum efficiency of the photodetectors. For PbS/S^{2-} photodetectors, a responsivity up to 50 A/W and a specific detectivity of 3.4×10^{8} Jones are obtained at 1550 nm and 300 K. For PbS/OH^{-} photodetectors, the responsivity is ~8 A/W and the corresponding specific detectivity is ~2.3×10^{8} Jones under the same measurement conditions. The 3-dB bandwidth of the PbS/S^{2-} and PbS/OH^{-} photodetector is 40 Hz and 11 Hz respectively, obtained under 1.1 W/cm^2 illumination at 2250 nm. This approach can become a viable approach to realize low-cost image sensors and single pixel photodetectors.

References

[1] B. Chen, W. Y. Jiang, J. Yuan, A. L. Holmes, and B. M. Onat, "Demonstration of a Room-Temperature InP-Based Photodetector Operating Beyond 3 μm," IEEE Photonics Technology Letters 23, 218-220 (2011).

[2] G. Konstantatos, I. Howard, A. Fischer, S. Hoogland, J. Clifford, E. Klem, L. Levina, and E. H. Sargent, "Ultrasensitive solution-cast quantum dot photodetectors," Nature 442, 180-183 (2006).

[3] G. Konstantatos, and E. H. Sargent, "Nanostructured materials for photon detection," Nat Nano 5, 391-400 (2010).

[4] K. Szendrei, F. Cordella, M. V. Kovalenko, M. Böberl, G. Hesser, M. Yarema, D. Jarzab, O. V. Mikhnenko, A. Gocalinska, and M. Saba, "Solution‐Processable Near-IR Photodetectors Based on Electron Transfer from PbS Nanocrystals to Fullerene Derivatives," Advanced Materials 21, 683-687 (2009).

[5] S. Coe-Sullivan, J. S. Steckel, W. K. Woo, M. G. Bawendi, and V. Bulović, "Large-Area Ordered Quantum-Dot Monolayers via Phase Separation During Spin-Casting," Advanced Functional Materials 15, 1117-1124 (2005).

[6] M. Böberl, M. V. Kovalenko, S. Gamerith, E. J. W. List, and W. Heiss, "Inkjet-Printed Nanocrystal Photodetectors Operating up to 3 μm Wavelengths," Advanced Materials 19, 3574-3578 (2007).

[7] J. Yolanda, M. Iwan, L. Karel, and H. Zeger, "Langmuir–Blodgett monolayers of colloidal lead chalcogenide quantum dots: morphology and photoluminescence," Nanotechnology 21, 295606 (2010).

[8] I. Moreels, K. Lambert, D. Smeets, D. De Muynck, T. Nollet, J. C. Martins, F. Vanhaecke, A. Vantomme, C. Delerue, G. Allan, and Z. Hens, "Size-Dependent Optical Properties of Colloidal PbS Quantum Dots," ACS Nano 3, 3023-3030 (2009).

[9] T. Rauch, M. Boberl, S. F. Tedde, J. Furst, M. V. Kovalenko, G. Hesser, U. Lemmer, W. Heiss, and O. Hayden, "Near-infrared imaging with quantum-dot-sensitized organic photodiodes," Nat Photon 3, 332-336 (2009).

[10] P. O. Anikeeva, J. E. Halpert, M. G. Bawendi, and V. Bulović, "Quantum Dot Light-Emitting Devices with Electroluminescence Tunable over the Entire Visible Spectrum," Nano Letters 9, 2532-2536 (2009).

[11] J. M. Luther, M. Law, M. C. Beard, Q. Song, M. O. Reese, R. J. Ellingson, and A. J. Nozik, "Schottky solar cells based on colloidal nanocrystal films," Nano letters 8, 3488-3492 (2008).

[12] E. Talgorn, M. A. de Vries, L. D. A. Siebbeles, and A. J. Houtepen, "Photoconductivity Enhancement in Multilayers of CdSe and CdTe Quantum Dots," ACS Nano 5, 3552-3558 (2011).

[13] H. Chen, A. Tangi, J. Yolanda, F. Stijn, C. Marco, G. Alban, D. Oksana, B. Filip, R. Günther, and H. Zeger, "The micropatterning of layers of colloidal quantum dots with inorganic ligands using selective wet etching," Nanotechnology 25, 175302 (2014).

[14] K. Lambert, J. Dendooven, C. Detavernier, and Z. Hens, "Embedding Quantum Dot Monolayers in Al2O3 Using Atomic Layer Deposition," Chemistry of Materials 23, 126-128 (2011).

[15] S. H. Kim, P. H. Sher, Y. B. Hahn, and J. M. Smith, "Luminescence from single CdSe nanocrystals embedded in ZnO thin films using atomic layer deposition," Nanotechnology 19, 365202 (2008).

[16] A. Pourret, P. Guyot-Sionnest, and J. W. Elam, "Atomic Layer Deposition of ZnO in Quantum Dot Thin Films," Advanced Materials 21, 232-235 (2009).

[17] R. Ihly, J. Tolentino, Y. Liu, M. Gibbs, and M. Law, "The Photothermal Stability of PbS Quantum Dot Solids," ACS Nano 5, 8175-8186 (2011).

[18] Sybren ten Cate, Yao Liu, C. S. Suchand Sandeep, Sachin Kinge, Arjan J. Houtepen, Tom J. Savenije, Juleon M. Schins, Matt Law, and Laurens D. A. Siebbeles, The Journal of Physical Chemistry Letters 4 (11), 1766 (2013).

[19] M. G. Moharam, T. K. Gaylord, E. B. Grann, and D. A. Pommet, "Formulation for stable and efficient implementation of the rigorous coupled-wave analysis of binary gratings," J. Opt. Soc. Am. A 12, 1068-1076 (1995).

[20] M. G. Moharam, T. K. Gaylord, D. A. Pommet, and E. B. Grann, "Stable implementation of the rigorous coupled-wave analysis for surface-relief gratings: enhanced transmittance matrix approach," J. Opt. Soc. Am. A 12, 1077-1086 (1995).

5

Air-stable PbS colloidal quantum dot phototransistors

5.1 Introduction

As a new optoelectronics material, colloidal quantum dots attracts lots of attention due to the cheap and easy heterogeneous integration on Si electronics or SOI photonic integrated circuits. However, due to the rapid oxidation of QD films while exposed to air, the devices degenerate as time goes on [1, 2]. Therefore, one of the main challenges to make these devices suitable for large scale applications in photonics and microelectronics is the achievement of air-stable devices. In order to solve this problem, many attempts have been made through various passivation approaches, such as halide passivation [3, 4], inorganic core/shell structures [5], colloidal atomic layer deposition [6], etc. Recently, atomic layer deposition (ALD) was proposed to use as a gas diffusion barrier to prevent oxidation and obtain a stable quantum dot solid [7, 8]. After ALD passivation, the electronic properties of the film can however also be changed [8], something we also observed in our work.

In Chapter 4, air-stable devices were obtained through atomic layer deposition (ALD) passivation. However, the photocurrent is quenched after ALD passivation, which results in a decrease in device performance. This is

attributed to alumina penetration in the colloidal quantum dot film during the ALD process [8]. Therefore, in order to avoid the photocurrent quenching we proposed the use of an additional layer of nanocrystal material with large bandgap as sacrificial layer to prevent alumina infilling in the PbS device layer.

In this chapter, two large bandgap nanocrystal materials, ZnSe and HfO_2, are explored as sacrificial layer to improve device performance. Although both materials showcase an improved photocurrent, the difficulty of ALD growth on ZnSe with organic shell make the implementation of air-stable devices still a challenge. Moreover, a ligand exchange procedure on ZnSe nanocrystals to enhance ALD growth usually results in inhomogeneous and discontinues films, which are not suitable as sacrificial layer to prevent alumina penetration. On the other hand, HfO_2 allows obtaining a homogenous film after ligand exchange, and can easily be covered with Al_2O_3 to create an air-stable device. In this chapter we demonstrate a PbS/S^{2-} phototransistor with ultrahigh responsivity up to 920 A/W under a back-gate voltage of –100 V. The electronic and optoelectronic properties of the obtained air-stable PbS phototransistor are investigated. The calculated field effect hole mobility is 0.025 $cm^2/(V{\cdot}s)$ and 0.01 $cm^2/(V{\cdot}s)$ for S^{2-} terminated and OH^- terminated PbS phototransistors, respectively. For a PbS/S^{2-} quantum dot transistor under 2.2 W/cm^2 illumination at 1550 nm and 5 V drain-source bias, the 3-dB bandwidth is 3 Hz under a back-gate voltage of −100 V, in the case of back-gate voltage of 100 V, the corresponding 3-dB bandwidth is 19 Hz. For PbS/OH^- quantum dot transistor, the 3-dB bandwidth is 12 Hz and 17 Hz under a back-gate voltage of −100 V and 100 V, respectively, which makes this approach suitable for low-cost image sensor and detector applications.

5.2 QD Synthesis

5.2.1 Synthesis of ZnSe colloidal quantum dots

For a standard ZnSe synthesis [9], zinc carbonate ($Zn_5(CO_3)2(OH)_6$, 0.06 mmol) was added to 10 mL of octadecene (ODE) together with 1.2 mmol of oleic acid in a three neck flask with cooler under air. The mixture was heated up to 270 ℃ to dissolve the zinc carbonate in ODE by the formation of a zinc carboxylate complex. The heterogeneous ODE-Se precursor was prepared by adding 1.5 mmol of Se powder to 10 mL of ODE without any heating. To initiate the reaction, 1 mL of the heterogeneous ODE-Se precursor was swiftly injected in the colorless reaction mixture containing the Zn precursor. Injection and growth temperature were set at 270 ℃ and 260 ℃, respectively. The transparent reaction mixture turns pale yellow, followed by a more intense yellow, depending on the size of the ZnSe nanocrystals formed. The reaction mixture

was purified by the addition of toluene, isopropanol and methanol, in a 1:1:1 ratio relative to the volume of the reaction mixture. The resulting turbid solution was centrifuged to obtain a pellet of NCs that was redispersed in toluene. Next, the purification was repeated twice using respectively toluene and methanol as solvent and nonsolvent to remove all residual reaction products.

5.2.2 Synthesis of HfO_2 colloidal quantum dots

The HfO_2 nanocrystal particles are synthesized in an autoclave [10] and the method is based on the solvothermal method developed by Buha et al in 2010 [11]. At first, 0.2 g of $HfCl_4$ was added to 45 mL of benzyl alcohol in a stainless steel autoclave with Teflon liner. Then the autoclave was sealed by screws and heated up to 220 ℃ for 3 days in an oven, after that the resulting precipitate was washed with ethanol and diethylether. In the synthesis, 4.5 mL of benzyl alcohol was added to $HfCl_4$ and the resulting final concentration was about 0.03 M. The mixture was stirred at room temperature to make the $HfCl_4$ dispersed in benzyl alcohol, afterwards the mixture was heated up to 60 ℃ for 5 min in the microwave for further dissolution. Finally the mixture was quickly heated up to 220 ℃. The microwave synthesizer was made by CEM discover equipped with an auto sampler and IR temperature detection. When the reaction finished, the suspension was precipitated by diethyl and then centrifuged, afterwards the supernatant was decanted and the QDs were resuspended in ethanol.

Furthermore, post-modification with dodecanoic acid was found to lead to the best results with an initial $HfCl_4$ concentration of 0.09 M. The nanoparticles were first precipitated with diethyl ether and resuspended in chloroform. After that 40 mg of dodecanoic acid was added into the suspension and stirred for 5 min. The addition of 50 μL of oleylamine yields a clear and colorless suspension. The particles were precipitated with a non-solvent and dispersed in apolar solvents.

5.3 Atomic layer deposition on colloidal nanocrystal films

In order to overcome the quenching of the PbS photodetector photocurrent after atomic layer deposition of alumina, both a sacrificial ZnSe and HfO_2 layer were evaluated. Effective air-stable passivation requires at least a 30 nm thick pin-hole free Al_2O_3 film.

5.3.1 Route 1: Al_2O_3 on colloidal ZnSe nanocrystal films

In this route, ZnSe colloidal quantum dots are used as sacrificial layer. Their absorbance spectrum is shown in Figure 5.1. The corresponding bandgap is ~ 3.1 eV and the initial concentration is ~ 100 μmol/L. The initial solution was diluted into different concentrations to check resulting film thickness after spin coating. Each time 25 μL of ZnSe QD solution was used in spin coating and the rotation speed was 1500 rpm. The thickness according to different concentrations was check by AFM and the height profiles are shown in Figure 5.2. In order to obtain a sacrificial layer with sufficient thickness, a 100 μmol/L QD solution was used to obtain a 220 nm thick ZnSe film. Such a film was deposited atop PbS QD photoconductors and the entire structure was exposed to 1000 ALD cycles to grow a 100 nm thick Al_2O_3 film. Figure 5.3 shows the dark current and photocurrent of the PbS/S^{2-} QD photodetector with different coating layer under 2.2 W/cm^2 illumination at 5 V bias as a function of time. The device with direct ALD passivation exhibited air stability with significant current quenching similar to the results in Chapter 4. However, the device with ZnSe sacrificial layer still showed degeneration over time, which suggests that the Al_2O_3 film is of insufficient quality.

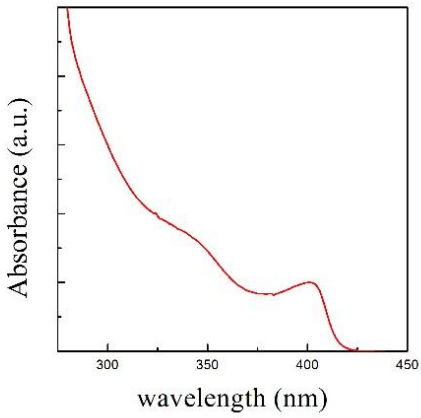

Figure 5.1: Absorbance spectrum of the ZnSe QDs used (solvent: chloroform).

In order to verify this, the surface morphology and corresponding layer thickness were examined by scanning electron microscope (SEM) and the results are shown in Figure 5.4. As one can see from the cross-section SEM image, the 1000 ALD cycles only result in a 20 nm thick Al_2O_3 layer, which is much thinner than the one grown on a silicon reference substrate (~ 70 nm, measured by ellipsometry). In addition, the ZnSe film is only 130 nm thick instead of the expected 220 nm. The cross-section SEM result also indicates many pinholes exist inside the Al_2O_3 film, which therefore is not capable to

form an air-tight passivation layer. This can be attributed to the long organic shell surrounding the ZnSe nanocrystal, slowing down or even preventing the ALD nucleation and growth.

As an alternative, we therefore included a ligand exchange of the ZnSe QDs to S^{2-} moieties, similar as the one used on the PbS nanocrystal films prior to ALD deposition of Al_2O_3. In this study, a saturated solution with $Na_2S{\cdot}9H_2O$ dissolved in MeOH (~ 2 mg/mL) was used to realize partial ligand exchange. Different ligand exchange duration times and cleaning procedures have been explored. However, as shown in Figure 5.5, the obtained ZnSe films peeled off from substrates under these various ligand exchange conditions, resulting in very rough and discontinuous ZnSe films, which cannot be used as ALD sacrificial layer anymore.

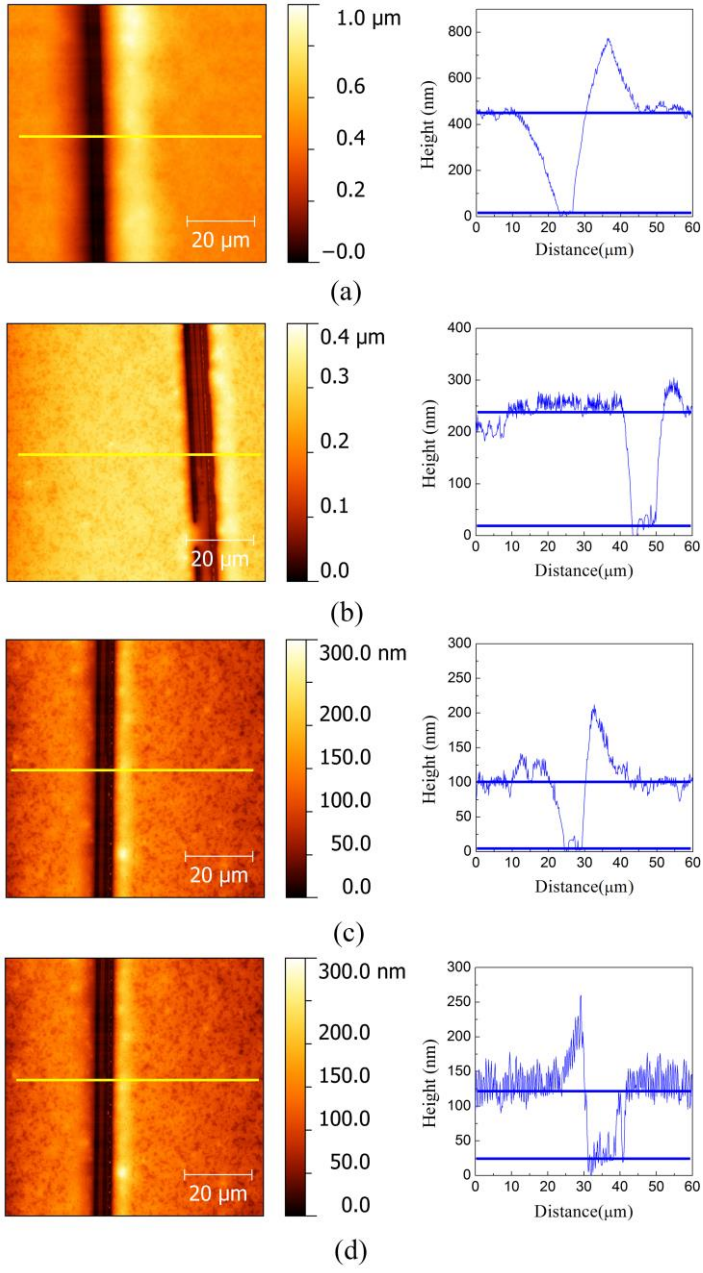

Figure 5.2: Film thickness is determined by the topographic analysis of a deliberately scratched ZnSe nanocrystal film fabricated through spin coating with different concentration: (a) 100 µmol/L; (b) 50 µmol/L; (c) 25 µmol/L and (d) 12.5 µmol/L. The yellow lines mark the respective cross section shown.

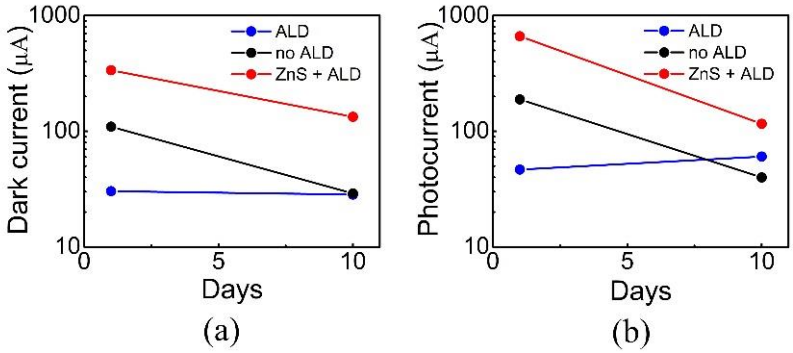

Figure 5.3: PbS/S^{2-} QD photodetector dark current (a) and photocurrent under 2.2 W/cm^2 optical illumination (b) and 5V bias as a function of time.

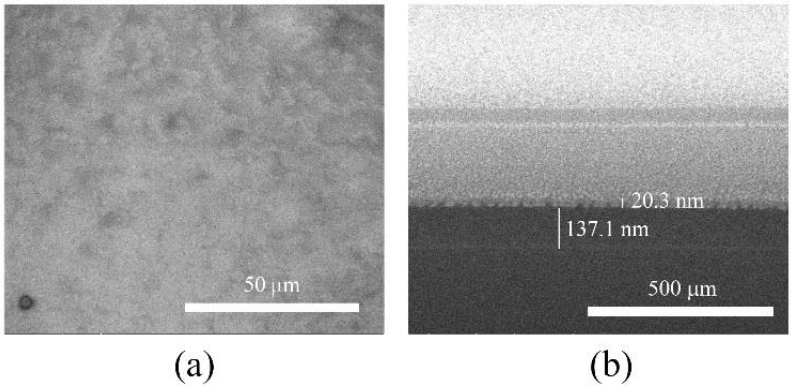

Figure 5.4: Top view SEM image and (b) Cross-section SEM of an Al_2O_3 layer deposited through 1000 ALD cycles on a ZnSe nanocrystal film.

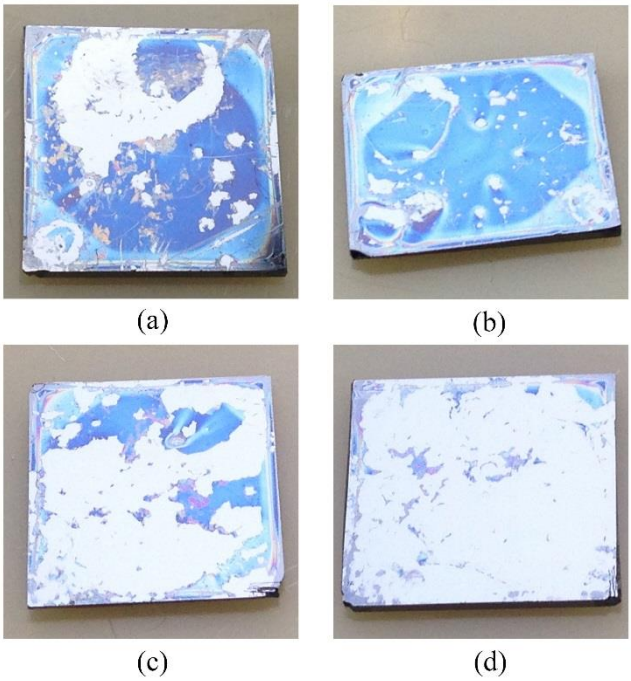

Figure 5.5: Photograph of the ZnSe film (a) with 1 min ligand exchange and 1 min MeOH cleaning; (b) with 1 min ligand exchange and 30 seconds MeOH cleaning; (c) with 2 min ligand exchange and 30 seconds MeOH cleaning; (d) with 5 min ligand exchange and 30 seconds MeOH cleaning.

5.3.2 Route 2: Al_2O_3 on colloidal HfO_2 nanocrystal films

The second route consists of using HfO_2 as sacrificial layer to enhance ALD growth compared to ZnSe. In this work, the HfO_2 nanocrystals were capped with dodecanoic acid, the average diameter is ~ 5-6 nm and the concentration is ~ 10 µmol/L. The corresponding bandgap is ~ 5.7 eV. The HfO_2 nanocrystal films were fabricate by spin coating, and AFM was used to measure corresponding layer thickness. The spin coating speed was set to 1500 rpm and the duration was 40 seconds. As shown in Figure 5.6, with the initial concentration (~ 10 µmol/L) of HfO_2 QD solution, the obtained QD layer is homogenous without cracks and the film thickness is ~ 20 nm. The corresponding RMS roughness is ~ 3.5 nm. However, in order to get a sacrificial layer with sufficient thickness, a thicker HfO_2 film should be obtained. Moreover, for the purpose of enhancing ALD nucleation and film growth, the organic shell surrounding the HfO_2 nanocrystal on the film surface should be removed. Therefore, a partial ligand

exchange on a HfO_2 nanocrystal film was used. A saturated ligand exchange solution with $Na_2S{\cdot}9H_2O$ dissolved in MeOH (~ 2 mg/mL) was used in the following study and the ligand exchange time was ~ 1 min, followed with a thorough cleaning by immersing the sample twice in MeOH and a final dip in isopropanol to remove residual impurities. The surface morphology and thickness after ligand exchange were measured by AFM and shown in Figure 5.7. As one can see, for one time spin coating, after ligand exchange, the remaining thickness of the HfO_2 film is ~ 20 nm and corresponding RMS roughness is ~ 3.1 nm, which indicates the ligand exchange and cleaning procedure does not affect the original morphology of the films. For HfO_2 films with 2 times layer-by-layer spin coating with ligand exchange procedure, the film thickness is ~ 40 nm, and the RMS roughness is ~ 4 nm without cracks. This implies the layer-by-layer spin coating with ligand exchange method can be used to form a homogenous, crack-free sacrificial layer with sufficient thickness to prevent alumina penetration.

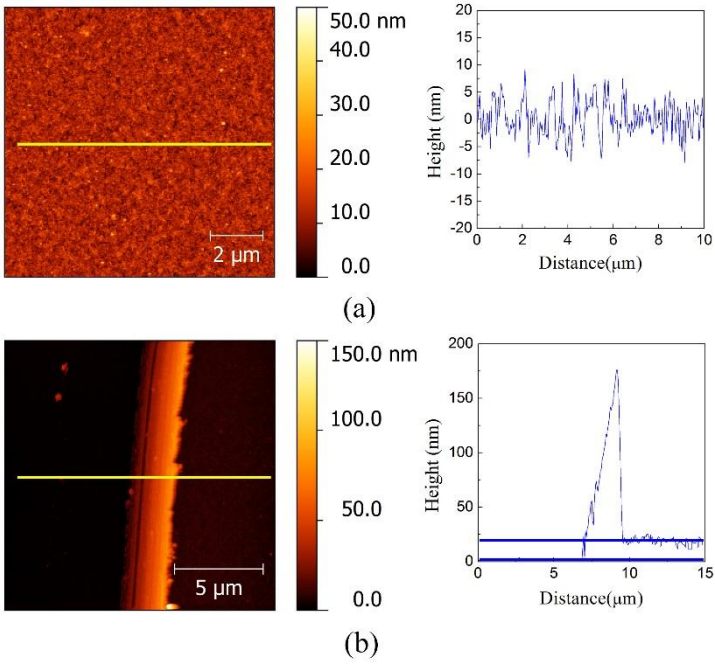

Figure 5.6: (a) AFM images obtained on HfO_2-dodecanoic acid film prepared by spin coating. (b) Film thickness is determined by the topographic analysis of a deliberately scratched HfO_2-dodecanoic acid film. The yellow lines mark the respective cross section shown.

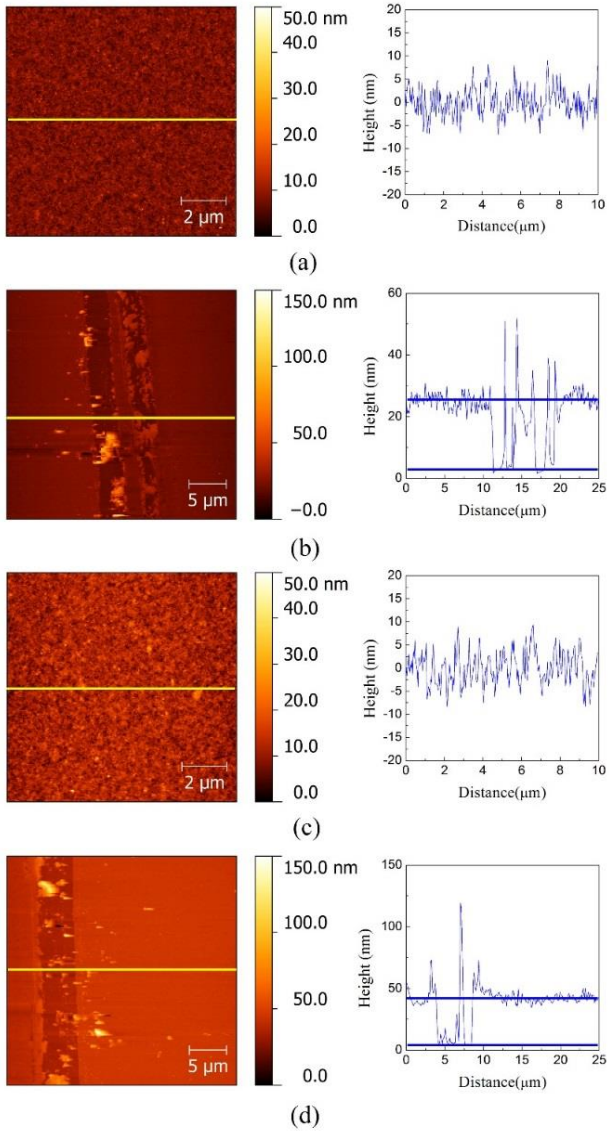

Figure 5.7: (a) AFM images obtained on a HfO_2-dodecanoic acid film prepared by 1 time spin coating with S^{2-} ligand exchange. (b) Film thickness is determined by the topographic analysis of a deliberately scratched HfO_2-S^{2-} acid film. The yellow lines mark the respective cross section shown. (c) AFM images obtained on HfO_2-dodecanoic acid film prepared by 2 times layer-by-layer spin coating with S^{2-} ligand exchange. (d) Film thickness is determined by the topographic analysis of a deliberately scratched HfO_2-S^{2-} acid film with 2 times LBL deposition.

In addition to implementing a homogenous, crack free HfO_2 sacrificial layer, a homogenous, pinhole free Al_2O_3 layer with sufficient thickness should also be obtained to implement air-stable devices. In general, at least 300 ALD cycles should be performed to obtain a ~ 30 nm thick pinhole free Al_2O_3 layer. In this study, 1000 ALD cycles were performed to ensure effective air-stable passivation. An Al_2O_3 thickness of ~ 70 nm was measured on a silicon reference by ellipsometry. In order to analysis the feasibility of ALD growth on a HfO_2 nanocrystal film, 1000 ALD cycles were directly performed on HfO_2 films, which were prepared through layer-by-layer spin coating and ligand exchange. Two HfO_2 samples were prepared, by 1 time and 2 times LBL deposition, respectively. A scanning electron microscope was used to analysis the obtained Al_2O_3 film thickness and the corresponding images are shown in Figure 5.8. In both cases, an Al_2O_3 layer with ~ 70 nm thickness was formed on the HfO_2 film, which corresponds well to the thickness value on the silicon reference. Compared to the ZnSe nanocrystal film with organic shell, HfO_2 films with removal of the organic shell exhibit more effective ALD nucleation and a similar Al_2O_3 film thickness as the one on a silicon reference was obtained.

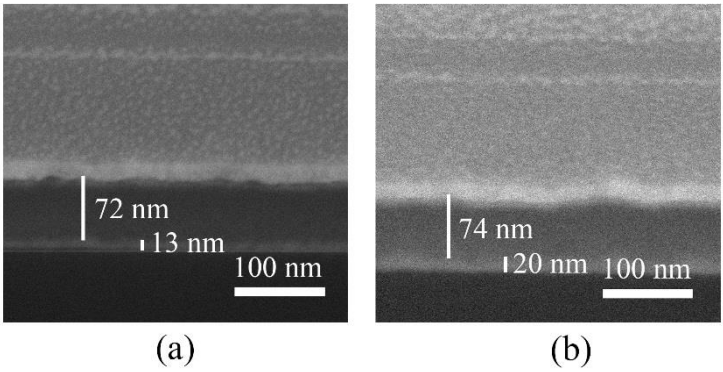

Figure 5.8: Cross-section SEM images of 1000 cycles ALD of Al_2O_3 on (a) HfO_2 with 1 time spin coating and S^{2-} ligand exchange (b) HfO_2 with 2 times LBL spin coating and S^{2-} ligand exchange.

5.4 PbS colloidal QD phototransistor

In this section, the electronic and optoelectronic properties of a PbS quantum dot phototransistor with HfO_2 nanocrystal sacrificial layer are investigated. The devices exhibit air-stable performance and high responsivity, which can potentially be applied in low cost SWIR image sensors.

5.4.1 Device fabrication

The fabrication of the PbS colloidal QD phototransistor started from depositing a 500 nm SiO_2 layer through plasma enhanced chemical vapor deposition (PECVD) on a highly doped Si substrate. The use of thinner SiO_2 layers of 100 nm in our experiments led to an early breakdown of the transistor. Interdigitated TiAu finger electrodes (5 nm Ti and 20 nm Au) were formed by evaporation. The electrode patterns were defined by optical lithography and lift-off procedure. The space between the electrodes was designed to be 2 μm and the finger width was also designed to be 2 μm, which is limited by the resolution of the lithography system. The total channel width of the phototransistor was ~ 1786 μm. The PbS QD layer deposition was performed through LBL deposition as mentioned in Chapter 4. The Si/SiO_2 substrate with patterned TiAu electrodes was dipped in a 1 μM PbS solution, and pulled out with a speed of 80 mm min^{-1}. After complete drying, the QD film was re-immersed into a ligand exchange solution of either $Na_2S{\cdot}9H_2O$ (10 mg ml^{-1}) or KOH (0.01 mg ml^{-1}) in formamide to replace the OlAc organic chain by S^{2-} or OH^- moieties, respectively. After ligand exchange, the samples were washed by immersing twice in formamide and acetone, respectively, followed by a final dip wash in isopropanol to remove all impurities. The resulting films were dried under nitrogen flow. The PbS films used in this study were obtained through 15 times LBL deposition. After that a selective wet-etching approach mentioned in Chapter 3 was used to pattern the PbS QD film to achieve patterns with a size of 104 μm × 94 μm. In a second step, the HfO_2 sacrificial layer was deposited on top of the PbS QD film by spin coating a HfO_2 nanocrystal film, followed by ligand exchange with saturated $Na_2S{\cdot}9H_2O$ in formamide (~ 2 mg ml^{-1}) to partially remove organics from the film surface. The obtained HfO_2-S^{2-} films were cleaned by re-immersing into methanol twice and a final dip in isopropanol. In this study, HfO_2 QD films were formed through 6 deposition cycles to implement a sacrificial layer with sufficient thickness. After that, 1000 thermal ALD cycles were performed to obtain an air-tight Al_2O_3 passivation layer. In order to test the effectiveness of the sacrificial layer and air-stability of the device, a PbS QD detector without HfO_2 coating and ALD coating as contrast samples were also fabricated and tested.

The corresponding device schematic diagram is shown in Figure 5.9. As one can see from the figure, the phototransistor configuration is similar to a photoconductor, where the source and drain electrodes are formed by a metal-semiconductor-metal architecture. The gate electrode is electrically isolated from the semiconductor channel by a thin dielectric film and serves as a third contact. By applying different gate voltages, the carrier density in the semiconductor channel can be electrically modulated through the field-effect.

The corresponding dark current can be substantially reduced by depleting the phototransistor channel. However, due to the existence of photoconductivity, the incident light can still activate the channel conductance through carrier photogeneration, which then ideally profits from a photoconductive gain mechanism as in the photoconductors [12]. Compared to a photoconductor, the architecture of a phototransistor allows to implement low dark current and high photoconductive gain at the same time. Generally, a high-performance phototransistor device requires high carrier mobility in the channel to obtain high photoconductive gain and efficient field-effect modulation to operate at low dark current.

In a typical phototransistor case, at low drain-source voltage range, the gradual channel approximation is usually considered for long channel transistors, i.e. the electric field perpendicular to the current flow which is generated by the gate voltage is much larger than the electric field parallel to the current flow which is created by the drain-source voltage. With this approximation, the current I_D can be obtained from the following equation,

$$I_D = \frac{WC_{ox}\mu}{L}\left(V_G - V_T - \frac{V_{DS}}{2}\right)V_{DS} \tag{5.1}$$

where W is the channel width, C_{ox} is the capacitance of the gate oxide per unit area, L is the channel length, μ is the field-effect mobility and V_T is the threshold voltage. The threshold voltage is defined as the gate bias needed for pinch off of the device and it is given by

$$V_T = V_{FB} + 2\psi_B + \frac{\sqrt{2\varepsilon_s q N_A (2\psi_B)}}{C_{ox}} \tag{5.2}$$

where V_{FB} is the flat-band voltage, ψ_B is the Fermi potential of the semiconductor, ε_s is the semiconductor permittivity, q is the elementary charge, N_A is the doping concentration.

When $V_{DS} \ll V_G$, equation (5.1) can be further simplified to

$$I_D = \frac{WC_{ox}\mu_{lin}}{L}(V_G - V_T)V_{DS} \tag{5.3}$$

where μ_{lin} is the linear regime field-effect mobility. The current I_D increases linearly with drain-source voltage V_{DS}, where the phototransistor operates like a variable resistor and regards as working in linear regime.

The linear mobilities μ_{lin} for holes and electrons can be extracted from the gradient of I_D versus V_G at a constant V_{DS} from the transfer curves (I_D - V_G) of the devices,

$$\left.\frac{dI_D}{dV_G}\right|_{V_{DS}=constant} = \frac{WC_{ox}V_{DS}}{L}\mu_{lin} \tag{5.4}$$

At high drain-source voltages, the channel pinches off near the drain electrodes and the corresponding current I_D saturates. The pinch off point starts to shift from the drain towards to the source when the drain-source voltage increase further, and the phototransistor is regarded as operating in the saturation regime, I_D can be expressed as

$$I_D = \frac{WC_{ox}\mu_{sat}}{2L}(V_G - V_T)^2 \tag{5.5}$$

where μ_{sat} is the saturation regime field-effect mobility.

In this work, we did not observe a clear saturation regime, therefore, the linear field-effect mobility was used to estimate the carrier mobility of the device.

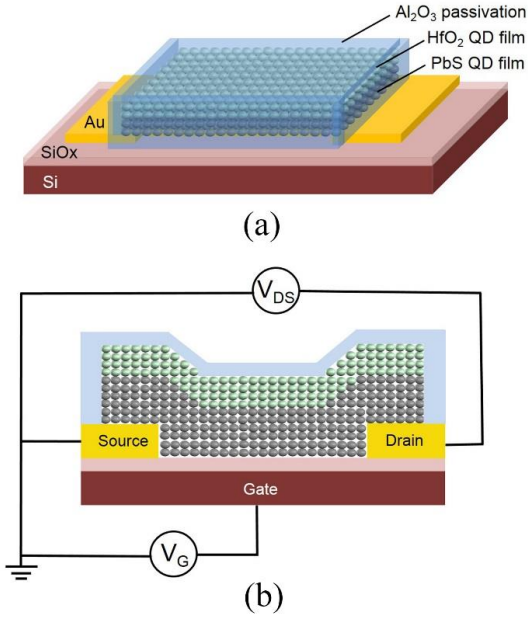

Figure 5.9: Schematic diagram in (a) side view and (b) cross-section of a PbS colloidal quantum dot phototransistor (not to scale).

5.4.2 Air-stability measurement

In order to verify air-stability of the device through ALD passivation, the current-voltage characteristics under different illumination were measured by surface illumination through a fiber coupled laser at 1550 nm. The source-drain current are measured without gate bias both in the dark and under 2.2 W/cm^2 illumination at 5 V bias as a function of time. As shown in Figure 5.10, quantum dot devices with ALD passivation exhibit improved air-stability compared with the one without passivation. Moreover, compared with a PbS quantum dot film directly passivated by ALD, the device coated with a HfO_2 sacrificial layer before ALD passivation has a much higher photocurrent, which is comparable to the un-passivated device. This indicates the photocurrent quenching because of ALD deposition can be improved by introducing a HfO_2 nanocrystal film with sufficient thickness as sacrificial layer.

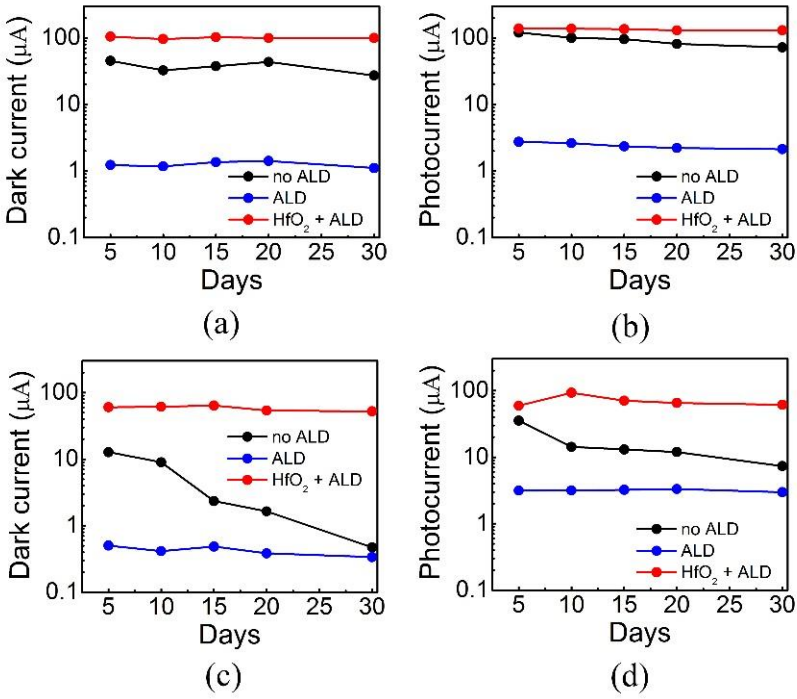

Figure 5.10: PbS/S^{2-} QD photodetector dark current (a) and photocurrent (b) under 2.2 W/cm^2 optical illumination and 5V bias as a function of time. PbS/OH^- QD photodetector dark current (c) and photocurrent (d) under 2.2 W/cm^2 optical illumination and 5V bias as a function of time.

5.4.3 Field-effect phototransistor measurements: results and discussion

In Figure 5.11(a) the output curves of a S^{2-} terminated PbS quantum dot phototransistor without ALD passivation (after 20 days) is shown. The device exhibits highly p-type conductance with quasi-linear drain current versus V_{SD}. However, complete turn-off of I_D is not observed. This is attributed to large hole densities in the device channel. The corresponding transfer-curve (I_D-V_G) is shown in Figure 5.12a. The calculated hole mobility μ_{lin} is obtained through equation (5.4) and the corresponding value is ~ 0.015 $cm^2/(V{\cdot}s)$. After ALD deposition, the PbS-S^{2-} film behaved as an ambipolar transistor with a dominant p-branch and a weak n-branch (Figure 5.11b). According to the transfer-curve of the device (Figure 5.12b), the calculated hole mobility and electron mobility is ~ 1.3×10^{-3} $cm^2/(V{\cdot}s)$ and ~ 1.3×10^{-4} $cm^2/(V{\cdot}s)$ at 5 V source-drain voltage, respectively. In Chapter 4, we presented the XPS results of a PbS colloidal quantum dot film with direct ALD deposition, which indicates there is a penetration of alumina into the PbS quantum dot solid. Highly conducting p-type PbS/S^{2-} quantum dot films before ALD deposition indicate there are many acceptors. Before ligand exchange, the OlAc-capped quantum dot film exhibits extremely low conductivity, and turns to highly p-type conductivity after S^{2-} exchange. For nonstoichiometric cadmium and lead based quantum dots, unpassivated surface chalcogenide anions were considered as acceptors in previous research [13]. Therefore, we can assume S^{2-} moieties which passivate the QD surface act as acceptors. After direct ALD deposition, a much lower mobility is observed, which can be attributed to the effect of alumina infilling. Also the phototransistor changed from p-type to ambipolar. This indicates the alumina infilling not only affects the carrier mobility, moreover, there is a reduction in the concentration of holes. This means the acceptors, i.e. the trap states for electrons, inside the quantum dot film were partially passivated because of alumina infilling. Furthermore, the change of conductance type of PbS QD film after direct ALD coating indicates that ALD does more than passivating, the properties of QD films can be also affected by ALD.

For the purpose of decreasing the photocurrent quenching, a layer of S^{2-} terminated HfO_2 nanocrystals with sufficient thickness was used to prevent alumina penetration during ALD. The corresponding results are shown in Figure 5.11c. The output curves for the device with sacrificial layer indicates the PbS quantum dot film remains p-type similar to the non-ALD coated device. Additionally, both photocurrent and dark current value is comparable to the non-ALD coated device, which confirms the HfO_2 sacrificial layer can effectively prevent alumina penetration and decrease photocurrent quenching. The calculated hole mobility μ_{lin} is ~ 0.025 $cm^2/(V{\cdot}s)$ according to the transfer curve

shown in Figure 5.12c. Compared to the device exposed in air after 20 days, the higher mobility value indicates oxidation of the device is prevented through ALD passivation. For the OH^- terminated PbS quantum dot device, similar results were obtained, the corresponding output curves and transfer curves are shown in Figure 5.13 and Figure 5.14. The calculated hole mobility μ_{lin} for air-stable PbS quantum dot device with sacrificial layer is ~ 0.01 $cm^2/(V \cdot s)$. Furthermore, for un-passivated PbS quantum dot devices exposed in air after 20 days, a high on/off ratio of ~ 100 was obtained for an OH^- terminated quantum dot device without light illumination (Figure 5.14a). However, for ALD passivated PbS quantum dot devices with HfO_2 sacrificial layer, a much lower on/off ratio was obtained, and the corresponding channels did not exhibit complete "turn off". This can be attributed to either the high p-type doping of the PbS channel or the use of a too thick channel. When the channel thickness is very thin, the phototransistor can be operated in a full depletion condition with an extremely low off-state dark current, and a large on/off ratio can be obtained. However, the corresponding absorption efficiency of the device is very low due to the thin absorption layer, resulting a limited detector response. On the other hand, a thick phototransistor channel can provide a much more efficient light absorption and high device responsivity. Meanwhile the thick channel devices may suffer from much higher off-state dark current and a large reduced on/off ratio. This is due to the fact that the field-effect capacitive coupling mainly affects the channel region close to the oxide surface. As a consequence, a significant leakage current can still exist through the upper part of the channel, and the corresponding channel cannot be completely switched off. A solution to overcome this dilemma is to use a hybrid structure such as colloidal QDs/graphene to decouple the electronic transport channel from the optical absorption layer, which will be further discussed as prospective research in Chapter 6.

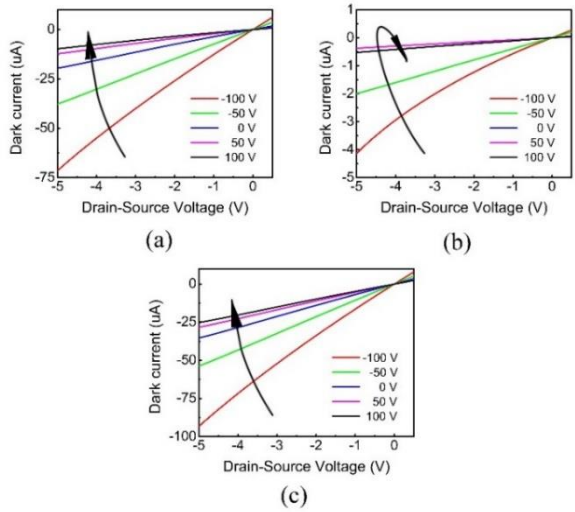

Figure 5.11: Electrical characteristics of PbS/S^{2-} QD phototransistors. Output curves of (a) bare PbS/S^{2-} QD phototransistors without passivation (b) PbS/S^{2-} QD phototransistors with direct ALD passivation and (c) PbS/S^{2-} QD phototransistors with HfO_2 sacrificial layer and ALD passivation.

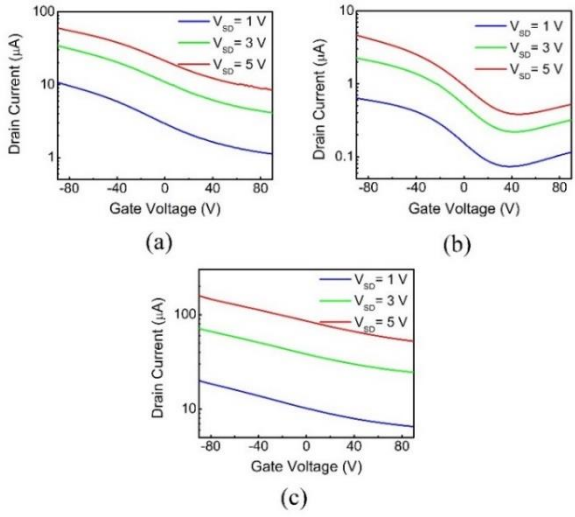

Figure 5.12: Transfer curves of (a) bare PbS/S^{2-} QD phototransistors without passivation (b) PbS/S^{2-} QD phototransistors with direct ALD passivation and (c) PbS/S^{2-} QD phototransistors with HfO_2 sacrificial layer and ALD passivation.

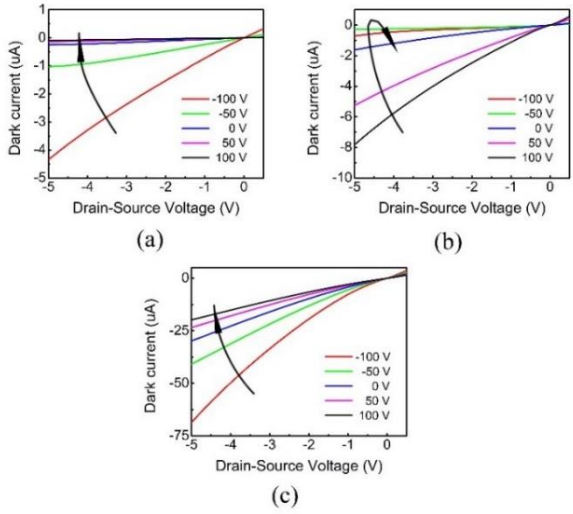

Figure 5.13: Electrical characteristics of PbS/OH^- QD phototransistors. Output curves of (a) bare PbS/OH^- QD phototransistors without passivation (b) PbS/OH^- QD phototransistors with direct ALD passivation and (c) PbS/OH^- QD phototransistors with HfO_2 sacrificial layer and ALD passivation.

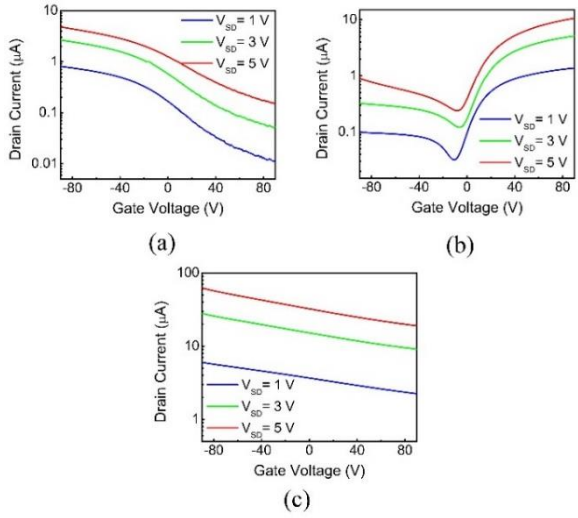

Figure 5.14: Transfer curves of (a) bare PbS/OH^- QD phototransistors without passivation (b) PbS/OH^- QD phototransistors with direct ALD passivation and (c) PbS/OH^- QD phototransistors with HfO_2 sacrificial layer and ALD passivation.

In order to explore the optoelectronics properties of the device, the transfer curves of a PbS quantum dot phototransistor with HfO_2 sacrificial layer were measured at various top surface illumination intensities through a fiber coupled laser at 1550 nm. The drain current under different light illumination intensities are shown in Figure 5.15. The photocurrent ($I_{photocurrent} = I_{illumination} - I_{dark\ current}$) at different gate voltages were extracted from the transfer curves and shown in Figure 5.16. For a S^{2-} terminated PbS QD phototransistor, under a back-gate voltage V_G of –100 V, the responsivity of the device is ~ 930 A/W; a responsivity of ~ 330 A/W was obtained where V_G = 100 V. For an OH^- terminated device, the responsivity is ~ 230 A/W and 510 A/W under a back-gate voltage of –100 V and 100 V, respectively. The high responsivity is attributed to the long lived trap states inside PbS quantum dot films. With high illumination intensity, trap states are refilled resulting in lower internal photoconductive gain, which corresponds to lower responsivity [14, 15].

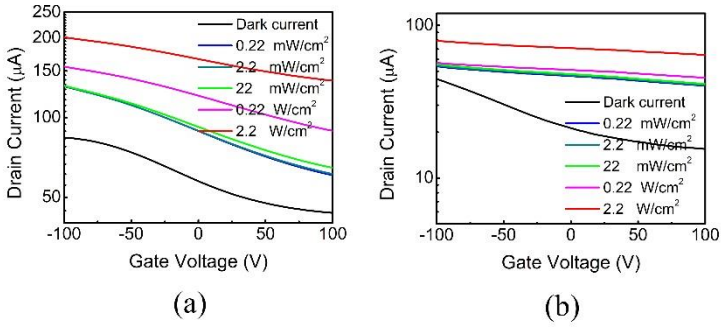

Figure 5.15: Characteristics of the PbS phototransistor. Transfer curves I_D-V_G of PbS/S^{2-} and PbS/OH^- phototransistors with HfO_2 sacrificial layer at various illumination intensities of the laser.

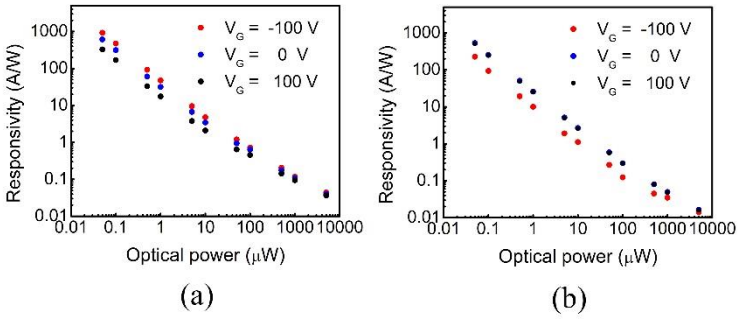

Figure 5.16: Responsivity as a function of optical illumination intensity at 1550 nm of (a) PbS/S^{2-} and (b) PbS/OH^- phototransistors with HfO_2 sacrificial layer.

To assess the device bandwidth, a laser was modulated at different frequencies and the corresponding photocurrent was obtained using a lock-in amplifier. The frequency response of a PbS/S^{2-} and PbS/OH^{-} quantum dot phototransistor with HfO_2 sacrificial layer under 2.2 W/cm^2 illumination at 1550 nm and 5 V drain-source bias are shown in Figure 5.17. For a PbS/S^{2-} quantum dot transistor, the 3-dB bandwidth is 3 Hz under a back-gate voltage of −100 V, in the case of a back-gate voltage of 100 V, the corresponding 3-dB bandwidth is 19 Hz. For the PbS/OH^{-} quantum dot transistor, the 3-dB bandwidth is 12 Hz and 17 Hz under a back-gate voltage of −100 V and 100 V, respectively, which makes this approach suitable for low-cost image sensor and detector applications.

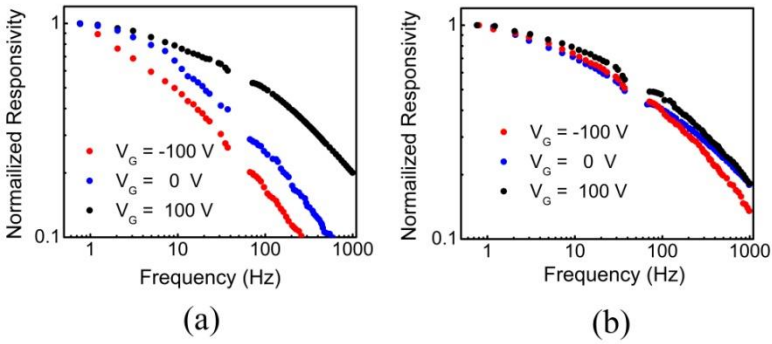

Figure 5.17: Electrical response of the (a) PbS/S^{2-} and (b) PbS/OH^{-} phototransistor (V_D = 5 V).

In order to estimate the quantum efficiency, we used RODIS for the corresponding optical simulation as mentioned in Chapter 4. In the simulation, the parameters were set corresponding to the real devices, i.e. 20 nm thickness for Au electrodes, 90 nm thickness of the PbS QD film (corresponding to 15 times LBL deposition), 120 nm thickness of HfO_2 and 100 nm thickness for Al_2O_3. In all cases the simulations were performed under surface normal incident illumination with transverse-electric (TE) and transverse-magnetic (TM) polarized light. The quantum efficiency as a function of wavelength in non-passivated colloidal QD PbS phototransistors are shown in Figure 5.18a. For TE polarized light illumination, at 1550 nm, the quantum efficiency for PbS/S^{2-} and PbS/OH^{-} phototransistors is 13.1% and 14.1%, respectively. For TM polarized light illumination, the quantum efficiency for PbS/S^{2-} and PbS/OH^{-} phototransistors is 10% and 10%, respectively. For ALD passivated PbS/S^{2-} and PbS/OH^{-} phototransistors, the corresponding quantum efficiency for TE polarized light is 13.7% and 15.3%, for TM polarized light is 10.2% and 12%, respectively. In the case of phototransistors with HfO_2 sacrificial layer, for TE

polarized light, the quantum efficiency is 10.5% and 11.6 % for PbS/S^{2-} and PbS/OH^{-} phototransistors. In TM illumination mode, the corresponding quantum efficiency for PbS/S^{2-} and PbS/OH^{-} phototransistors is 8.1% and 11.6%, respectively. We did not observe strong polarization dependence around 1550 nm in our measurement. In the short-wave infrared wavelength range, the polarization dependence of the phototransistors becomes very small. Nevertheless, according to the simulation results, although the ALD passivated phototransistors exhibit slightly higher quantum efficiency in both TE and TM polarized light illumination case, due to the decrease of the photocurrent quenching by introducing of a HfO_2 sacrificial layer, the phototransistors exhibit higher field effect hole mobility, corresponding to higher responsivity.

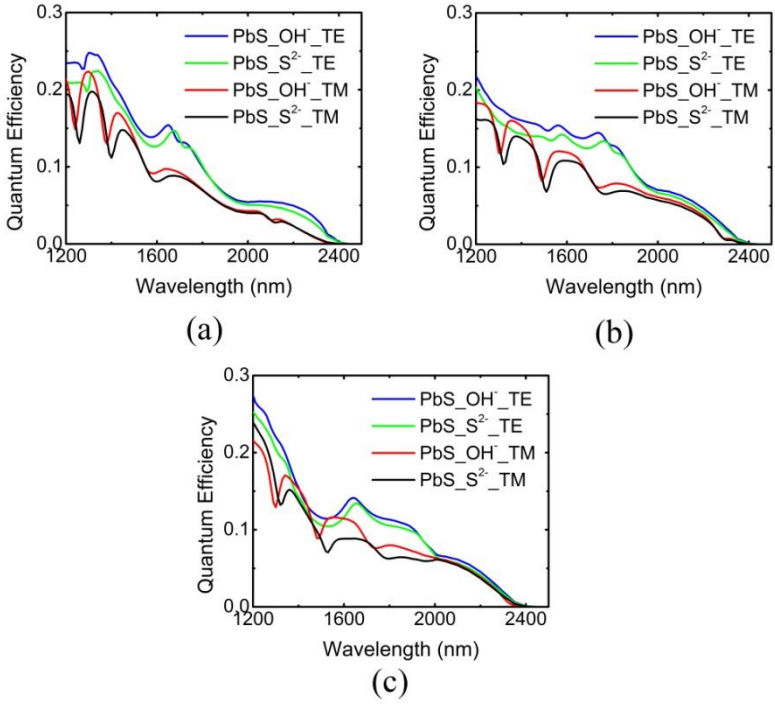

Figure 5.18: Simulated quantum efficiency of PbS QD photodetectors (a) without and (b) with 30 nm Al_2O_3 passivation (c) with HfO_2 sacrificial layer and ALD passivation in short-wave infrared range.

5.5 Conclusion

In this chapter, in order to decrease photocurrent quenching from the ALD passivation process, ZnSe and HfO_2 nanocrystal films were explored as sacrificial material to prevent alumina penetration and infilling. Compared to

ZnSe, HfO_2 exhibits better compatibility with the solid state ligand exchange approach and ALD growth technique. A homogenous, crack free HfO_2 nanocrystal film can be obtained through LBL spin coating with ligand exchange approach. Electronic and optoelectronic characteristic results of the devices indicate the HfO_2 sacrificial layer is capable to prevent alumina infilling and decrease photocurrent quenching. With effective ALD passivation, we demonstrate air-stable PbS colloidal quantum dot phototransistors with high responsivity. Furthermore, the change of conductance type of PbS QD film after direct ALD coating indicates that ALD does more than passivating; the electronic properties of QD films can also be directly affected by ALD. An ultrahigh responsivity up to 920 A/W under a back-gate voltage of –100 V is obtained through a S^{2-} terminated PbS phototransistor. The electronic and optoelectronic properties of the obtained air stable PbS phototransistors were also investigated. The calculated field effect hole mobility is 0.025 $cm^2/(V{\cdot}s)$ and 0.01 $cm^2/(V{\cdot}s)$ for S^{2-} terminated and OH^- terminated PbS phototransistors, respectively. Under 1.1 W/cm^2 illumination at 1550 nm, for a PbS/S^{2-} quantum dot transistor, the 3-dB bandwidth is 3 Hz under a back-gate voltage of −100 V, the corresponding 3-dB bandwidth is 19 Hz in the case of back-gate voltage of 100 V. For PbS/OH^- quantum dot transistor, the 3-dB bandwidth is 12 Hz and 17 Hz under a back-gate voltage of −100 V and 100 V, respectively, which make these devices suitable for low-cost image sensor and detector applications. The corresponding quantum efficiency of the phototransistors was also estimated by performing a numerical simulation study through RODIS software. In the case of phototransistors with HfO_2 sacrificial layer under surface normal incident illumination at 1550 nm, for TE polarized light, the quantum efficiency is 10.5% and 11.6 % for PbS/S^{2-} and PbS/OH^- phototransistors. In TM illumination mode, the corresponding quantum efficiency for PbS/S^{2-} and PbS/OH^- phototransistors is 8.1% and 11.6%, respectively.

References

[1] C. Hu, A. Gassenq, Y. Justo, K. Devloo-Casier, H. Chen, C. Detavernier, Z. Hens, and G. Roelkens, "Air-stable short-wave infrared PbS colloidal quantum dot photoconductors passivated with Al_2O_3 atomic layer deposition," Applied Physics Letters 105, (2014).

[2] Y. Liu, M. Gibbs, C. L. Perkins, J. Tolentino, M. H. Zarghami, J. Bustamante, and M. Law, "Robust, Functional Nanocrystal Solids by Infilling with Atomic Layer Deposition," Nano Letters 11, 5349-5355 (2011).

[3] J. Zhang, J. Gao, E. M. Miller, J. M. Luther, and M. C. Beard, "Diffusion-Controlled Synthesis of PbS and PbSe Quantum Dots with in Situ Halide Passivation for Quantum Dot Solar Cells," ACS Nano 8, 614-622 (2014).

[4] W. K. Bae, J. Joo, L. A. Padilha, J. Won, D. C. Lee, Q. Lin, W.-k. Koh, H. Luo, V. I. Klimov, and J. M. Pietryga, "Highly Effective Surface Passivation of PbSe Quantum Dots through Reaction with Molecular Chlorine," Journal of the American Chemical Society 134, 20160-20168 (2012).

[5] J. W. Stouwdam, J. Shan, F. C. J. M. van Veggel, A. G. Pattantyus-Abraham, J. F. Young, and M. Raudsepp, "Photostability of Colloidal PbSe and PbSe/PbS Core/Shell Nanocrystals in Solution and in the Solid State," The Journal of Physical Chemistry C 111, 1086-1092 (2007).

[6] S. J. Oh, N. E. Berry, J.-H. Choi, E. A. Gaulding, H. Lin, T. Paik, B. T. Diroll, S. Muramoto, C. B. Murray, and C. R. Kagan, "Designing High-Performance PbS and PbSe Nanocrystal Electronic Devices through Stepwise, Post-Synthesis, Colloidal Atomic Layer Deposition," Nano Letters 14, 1559-1566 (2014).

[7] R. Ihly, J. Tolentino, Y. Liu, M. Gibbs, and M. Law, "The Photothermal Stability of PbS Quantum Dot Solids," ACS Nano 5, 8175-8186 (2011).

[8] Y. Liu, J. Tolentino, M. Gibbs, R. Ihly, C. L. Perkins, Y. Liu, N. Crawford, J. C. Hemminger, and M. Law, "PbSe Quantum Dot Field-Effect Transistors with Air-Stable Electron Mobilities above 7 $cm^2\ V^{-1}\ s^{-1}$," Nano Letters 13, 1578-1587 (2013).

[9] S. Flamee, R. Dierick, M. Cirillo, D. Van Genechten, T. Aubert, and Z. Hens, "Synthesis of metal selenide colloidal nanocrystals by the hot injection of selenium powder," Dalton Transactions 42, 12654-12661 (2013).

[10] J. Roo, K. Keukeleere, J. Feys, P. Lommens, Z. Hens, and I. Driessche, "Fast, microwave-assisted synthesis of monodisperse HfO2 nanoparticles," Journal of Nanoparticle Research 15, 1-11 (2013).

[11] J. Buha, D. Arcon, M. Niederberger, and I. Djerdj, "Solvothermal and surfactant-free synthesis of crystalline Nb_2O_5, Ta_2O_5, HfO_2, and Co-doped HfO_2 nanoparticles," Physical Chemistry Chemical Physics 12, 15537-15543 (2010).

[12] D. Kufer, and G. Konstantatos, "Photo-FETs: Phototransistors Enabled by 2D and 0D Nanomaterials," ACS Photonics 3, 2197-2210 (2016).

[13] G. W. Bryant, and W. Jaskolski, "Surface Effects on Capped and Uncapped Nanocrystals," The Journal of Physical Chemistry B 109, 19650-19656 (2005).

[14] G. Konstantatos, and E. H. Sargent, "Nanostructured materials for photon detection," Nat Nano 5, 391-400 (2010).

[15] M. Böberl, M. V. Kovalenko, S. Gamerith, E. J. W. List, and W. Heiss, "Inkjet-Printed Nanocrystal Photodetectors Operating up to 3 μm Wavelengths," Advanced Materials 19, 3574-3578 (2007).

6

Conclusions and perspectives

6.1 Conclusions

In this thesis, we aim for demonstrating a novel approach to implement photodetectors based on solution-based semiconductor QDs, which enable implementing a low-cost and versatile photodetector technology, amenable to integration.

First, we explored various solution-based film preparation methods to obtain a homogenous, crack-free quantum dot film. Drop casting and dip coating as quantum dot film preparation methods were explored. Metal-free inorganic ligands, such as S^{2-} and OH^{-}, are investigated to facilitate the charge carrier transport. A solid state ligand exchange approach with these short inorganic moieties to enhance photoconductivity was optimized. In order to remove film cracks during the ligand exchange procedure, a layer-by-layer approach was developed. Uniform, ultra-smooth colloidal QD films without cracks were obtained through this approach. The first generation photoconductors was obtained with cut-off wavelength up to 2.2 μm.

In addition, we have developed a method for the micro-patterning of films of colloidal QD stabilized by inorganic ligands. Using both PbS and CdSe/CdS QDs, films were made by a layer-by-layer approach, where each cycle involves the deposition of a QD layer by dip-coating, the replacement of the native

organic ligands by inorganic moieties, such as OH^- and S^{2-}, followed by a thorough cleaning of the resulting film. We demonstrated that with this method, a smooth and crack-free QD film is formed, on which a photoresist can be spun. The micropatterned films are defined by optical lithography with a positive photoresist, followed by the removal of uncovered QDs by wet etching using a HCl/H_3PO_4 mixture ($1HCl:10H_3PO_4$). High resolution films with feature dimensions down to 500 nm can be realized by this selective wet etching method, limited by the resolution of the lithographic process and a slight over-etching, both on planar and on 3D substrates. For CdSe/CdS core/shell QDs, the micro-patterned films still retained their photoluminescence after lithography and wet etching. Nearly 78% of the QY remains and no additional trap states are introduced in this procedure. These results indicate that the low-cost micro-patterning method based on a layer-by-layer approach and selective wet etching is a very promising way to achieve the large-scale device integration of colloidal QDs.

In order to implement photodetector and photovoltaic applications, making the colloidal QD devices air-stable is of key importance for a practical application. For the purpose of obtaining air-stable QD devices, the main issue is to avoid oxidation of the QD film. This requires a well passivating, pinhole-free layer that is transparent at the wavelengths to be detected. Atomic layer deposition (ALD) usually results in films without pinhole and is therefore very suitable for passivation. Al_2O_3, which is probably the most extensively characterized material in ALD, is a natural choice in this respect since it is a wide bandgap insulator that is transparent in the short-wave infrared. In this thesis, air stable PbS colloidal QD photodetectors with Al_2O_3 atomic layer deposition passivation to realize SWIR photodetection were demonstrated. The QD films were prepared by a layer-by-layer approach to form a uniform colloidal QD film and two kinds of inorganic ligands, S^{2-} and OH^-, were investigated to facilitate carrier transport. PbS photodetectors with cut-off wavelength of 2.4 μm are obtained. We also performed a numerical simulation on corresponding quantum efficiency of the photodetectors. For PbS/S^{2-} photodetectors, a responsivity up to 50 A/W and a specific detectivity of 3.4×10^8 Jones are obtained at 1550 nm and 300 K. For PbS/OH^- photodetectors, the responsivity is ~8 A/W and the corresponding specific detectivity is ~2.3×10^8 Jones under the same measurement conditions. The 3-dB bandwidth of the PbS/S^{2-} and PbS/OH^- photodetector is 40 Hz and 11 Hz respectively, obtained under 1.1 W/cm^2 illumination at 2250 nm. This approach can become a viable approach to realize low-cost imaging sensors and single pixel photodetectors.

However, the photocurrent is quenched after ALD passivation, which results in a decrease in device performance. This is attributed to alumina penetration in the colloidal quantum dot film during the ALD process. Therefore, in order to avoid the photocurrent quenching we proposed the use of an additional layer of

nanocrystal material with large bandgap as sacrificial layer to prevent alumina infilling in the PbS device layer. Two large bandgap nanocrystal materials, ZnSe and HfO_2, are explored as sacrificial layer to improve device performance. Although both materials showcase an improved photocurrent, the difficulty of ALD growth on ZnSe with organic shell makes the implementation of air-stable devices still as challenge. Moreover, a ligand exchange procedure on ZnSe nanocrystals to enhance ALD growth usually results an un-homogeneous and discontinuous film, which is not suitable as sacrificial layer to prevent alumina penetration. Compared to ZnSe, HfO_2 exhibits better compatibility with the solid state ligand exchange approach and ALD growth technique. A homogenous, crack free HfO_2 nanocrystal film can be obtained through LBL spin coating with a ligand exchange approach. Electronic and optoelectronic characteristic results of the devices indicate the HfO_2 sacrificial layer is capable to prevent alumina infilling and decrease photocurrent quenching. With effective ALD passivation, we demonstrate air-stable PbS colloidal quantum dot phototransistors with high responsivity. An ultrahigh responsivity up to 920 A/W under a back-gate voltage of –100 V is obtained through a S^{2-} terminated PbS phototransistor. The electronic and opto-electronic properties of the obtained air-stable PbS phototransistors were also investigated. The calculated field effect hole mobility is 0.025 $cm^2/(V{\cdot}s)$ and 0.01 $cm^2/(V{\cdot}s)$ for S^{2-} terminated and OH^- terminated PbS phototransistors, respectively. Under 1.1 W/cm^2 illumination at 1550 nm, for a PbS/S^{2-} quantum dot transistor, the 3-dB bandwidth is 3 Hz under a back-gate voltage of −100 V, in the case of a back-gate voltage of 100 V, the corresponding 3-dB bandwidth is 19 Hz. For the PbS/OH^- quantum dot transistor, the 3-dB bandwidth is 12 Hz and 17 Hz under a back-gate voltage of −100 V and 100 V, respectively, which makes this approach suitable for low-cost image sensor and detector applications. The corresponding quantum efficiency of the phototransistors was also estimated by performing a numerical simulation study through RODIS software. In the case of phototransistors with HfO_2 sacrificial layer under surface normal incident illumination at 1550 nm, for TE polarized light, the quantum efficiency is 10.5% and 11.6 % for PbS/S^{2-} and PbS/OH^- phototransistors. In TM illumination mode, the corresponding quantum efficiency for PbS/S^{2-} and PbS/OH^- phototransistors is 8.1% and 11.6%, respectively.

6.2 Perspectives

For colloidal quantum dot photoconductors, there still remains room to improve in terms of device performance. One path to improve the sensitivity of the devices is to enhance the absorption of light in the quantum dot film. In this respect, silicon resonant grating structures such as high contrast grating (HCG),

can be used to implement this goal. Highly doped Si gratings can be used not only for light absorption enhancement, but also for carrier extraction as electric contact to further reduce the shadowing of the metal electrodes. By carefully choosing the colloidal quantum dots and the corresponding passivation ligands material, efficient carrier injection can be realized at the quantum dot/highly doped Si grating interface [1].

To obtain high performance colloidal quantum dot phototransistors, one of the key performance metrics is the carrier mobility in the channel. In this work we demonstrate high responsivity phototransistors with reasonable hole mobility. However, the carrier mobility in the phototransistor channel can be further improved by using novel nanostructured materials such as colloidal quantum dot superlattices. On the other hand, hybrid materials, such as the combination of colloidal quantum dots with 2D materials like graphene or MoS_2, can also be explored for SWIR detection to obtain phototransistors with ultrahigh sensitivity. In this case, the colloidal quantum dots can implement strong light absorption and the 2D material can provide a high carrier mobility channel for the photogenerated carriers.

Extending the photodetection wavelength from the short-wave infrared to the mid-infrared is another goal for colloidal QD photodetectors. This study can be carried out with the current device design by using QDs such as HgTe which can provide absorption in the mid infrared region. Furthermore, our hybrid integration technology can be applied not only to single pixel photodetectors, but also pixel array fabrication, which will offer more prospects for practical applications.

References

[1] S. Masala, V. Adinolfi, J.-P. Sun, S. D. Gobbo, O. Voznyy, I. J. Kramer, I. G. Hill, and E. H. Sargent, "The Silicon:Colloidal Quantum Dot Heterojunction," Advanced Materials 27(45), 7445-7450 (2015).

A

QD film characterization

A.1 Introduction

In Chapter 3, we discussed the effect of micropatterning on the quantum yield (QY) of the film. However, in order to make the text clear, the details about QY measurement were not provide. As a consequence, a brief introduction about the QY measurement is given in the appendix section.

A.2 QY measurement

In this work, the QY of the QD films was measured using an integrating sphere that equips the Edinburgh Instruments FLSP920 spectrometer. The design of this sphere is illustrated in Figure 3.20.

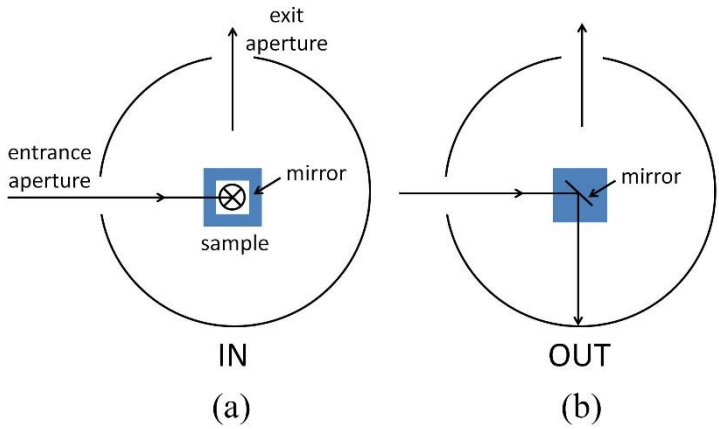

Figure A.1: Top view of the integrating sphere illustrating the two types of measurement when (a) the sample is inside the beam ('IN' position) and (b) the sample is outside the beam ('OUT' position), which are selected by rotating the mirror.

The calculation method was slightly modified from the one reported by Mello et al. [1]. The general definition of the QY is:

$$QY = \frac{E}{A_{QD} \times X} \tag{A.1}$$

where E is the number of photons emitted, A_{QD} is the absorption of the QDs and X is the number of photons arriving on the sample and available for absorption by the QDs. As illustrated in Figure 3.3, in the integrating sphere the beam can be either directed to the sample or to the wall of the sphere by rotating an internal mirror. The sample is said to be either inside or outside the beam, and the corresponding measurements are therefore denoted as 'IN' and 'OUT', respectively. Hence, E_{IN} and E_{OUT} correspond to the values obtained by integrating the signal corresponding to emitted photons. Similarly, X corresponds to the values obtained by integrating the signal corresponding to excitation photons.

The absorption can be defined as:

$$A = 1 - T \tag{A.2}$$

where T is the fraction of photons transmitted after the first pass of the beam through the sample. T can be determined by the ratio between X_{IN} and X_{OUT}. However, a fraction of photons might also get lost because of the substrate of the film itself. This fraction is most likely purely reflection as glass slides should

not significantly absorb in this wavelength range. As a matter of fact, due to the geometry of the integrating sphere, during 'IN' measurements a fraction of photons, denoted R, can get reflected on the substrate and exit the sphere through the entrance aperture, whereas this should not happen if the beam is first directed to a wall of sphere as it is the case in a 'OUT' measurement. Thus $A_{QD}$is determined by:

$$A_{QD} = A_{sample} - R_{substrate} \tag{A.3}$$

With:

$$A_{sample} = 1 - \frac{X_{sample,IN}}{X_{sample,OUT}} \tag{A.4}$$

$$R_{substrate} = 1 - \frac{X_{substrate,IN}}{X_{substrate,OUT}} \tag{A.5}$$

where 'sample' refers to the entire system: QDs and substrate. The correction with R was found to be critical as it typically accounts for more than 10% of the A-value. This correction actually constitutes our modification from previously reported methods [1, 2].

Then, the amount of photons emitted by the QDs is determined by measuring the $E_{sample,IN}$ value. However, A_{QD} is determined for the fraction of photons that got absorbed during a single pass through the sample ($E_{sample,OUT}$). Experiments showed that correcting $E_{sample,IN}$ considering more than four reflections on walls of the sphere did not significantly affect the result and further reflections were not considered. Thus, the number of photons emitted is determined by:

$$E = E_{sample,IN} - \left(1 - A_{QD}\right)E_{sample,OUT} - \sum_{n=1}^{\infty} A_{QD}^{n}\left(1 - A_{QD}\right)E_{sample,OUT} \tag{A.6}$$

where we can limit ourselves to n = 3.

Finally, the amount of photons actually available for the QDs is determined by measuring X_{empty}. Here again, due to the design of the sphere and the sample holder, X_{empty} is best estimated when measured in the OUT position.

The complete formula for QY is therefore given by [1]:

$$QY = \frac{E_{sample,IN} - \left(1 - A_{QD}\right)E_{sample,OUT} - \sum_{n=1}^{\infty} A_{QD}^{n}\left(1 - A_{QD}\right)E_{sample,OUT}}{X_{empty} \times A_{QD}} \tag{A.7}$$

Considering with equation (A.4) and (A.5), the QY can be further expressed as:

$$QY = \frac{E_{sample,IN} - (1 - A_{QD}) E_{sample,OUT} - \sum_{n=1}^{\infty} A_{QD}^{n} (1 - A_{QD}) E_{sample,OUT}}{X_{empty} \times \left(\frac{X_{substrate,IN}}{X_{substrate,OUT}} - \frac{X_{sample,IN}}{X_{sample,OUT}} \right)} \quad \text{(A.8)}$$

For an accurate QY measurement, the acquisition parameters are crucial. The excitation wavelength span after transmission through the slit should be wide enough to allow an accurate integration on the X-signals. The emission wavelength span has to be equal or smaller than the acquisition step. The acquisition steps should be much smaller than the excitation wavelength span also for an accurate integration of X-signals. Of course, the excitation and emission wavelength spans have to be identical for all measurements. Here, the measurements were realized with an excitation wavelength span of 3 nm, an emission wavelength span of 0.1 nm, the X-signals were recorded with steps of 0.1 nm and the E-signals were recorded with steps of 1 nm. Due to the large excitation wavelength span (3 nm), the X-signals have to be integrated on reasonably large range. Here, X-values were obtained by integrating the signal from 345 nm to 385 nm for an actual excitation wavelength of 365 nm.

References

[1] J. C. de Mello, H. F. Wittmann, and R. H. Friend, "An improved experimental determination of external photoluminescence quantum efficiency," Advanced Materials 9, 230-232 (1997).

[2] L. Porrès, A. Holland, L.-O. Pålsson, A. P. Monkman, C. Kemp, and A. Beeby, "Absolute Measurements of Photoluminescence Quantum Yields of Solutions Using an Integrating Sphere," Journal of Fluorescence 16, 267-273 (2006).